

---

Electronic Thesis and Dissertation Repository

---

4-9-2024 2:00 PM

# Luminescence and Structural Properties of Silicon-Germanium Quantum Structures Fabricated by Ion Implantation

Matheus Coelho Adam, *Western University*

Supervisor: Goncharova, Lyudmila V., *The University of Western Ontario*

Co-Supervisor: Simpson, Peter J., *The University of British Columbia, Kelowna, BC, Canada*

A thesis submitted in partial fulfillment of the requirements for the Doctor of Philosophy degree in Physics

© Matheus Coelho Adam 2024

Follow this and additional works at: <https://ir.lib.uwo.ca/etd>

 Part of the [Condensed Matter Physics Commons](#)

---

## Recommended Citation

Coelho Adam, Matheus, "Luminescence and Structural Properties of Silicon-Germanium Quantum Structures Fabricated by Ion Implantation" (2024). *Electronic Thesis and Dissertation Repository*. 9970. <https://ir.lib.uwo.ca/etd/9970>

This Dissertation/Thesis is brought to you for free and open access by Scholarship@Western. It has been accepted for inclusion in Electronic Thesis and Dissertation Repository by an authorized administrator of Scholarship@Western. For more information, please contact [wlsadmin@uwo.ca](mailto:wlsadmin@uwo.ca).

## Abstract

The advancement of semiconductor materials has played a crucial role in driving positive technological breakthroughs that impact humanity in numerous ways. The presence of defects significantly alters the physical properties of semiconductors, making their analysis essential in the fabrication of semiconductor devices. I present a new method to quantify surface and near-surface defects in single crystal semiconductors. Epitaxially grown silicon (Si) was measured by low energy electron diffraction (LEED) to obtain the surface Debye temperature ( $\theta_D$ ). The results showed the surface  $\theta_D$  of bulk Si (001), 1.0  $\mu\text{m}$ , and 0.6  $\mu\text{m}$  Si on sapphire of 333 K, 299 K, and 260 K, respectively. Complementary measurements using Rutherford backscattering spectrometry (RBS) and positron annihilation spectroscopy (PAS) showed a correlation between the concentration of defects,  $N_d$ , and the change in the surface  $\theta_D$ , expressed by the empirical relation  $\theta_D = (365 \pm 14) - (8.1 \pm 1.5) \times 10^{-13} N_d$  for silicon. Arrays of SiGe quantum dots (QDs) ranging from 1.7 to 5.7 nm in diameter were fabricated using two methods: co-implantation of Si and Ge into an  $\text{SiO}_2$  matrix, and a hybrid method involving plasma-enhanced chemical vapour deposition (PECVD) of Si-rich  $\text{SiO}_x$  deposition plus Ge implantation. Ion implantation conditions allowed incorporation of up to 8.0 peak Ge atomic percent and identical thermal procedures were used in both methods. SiGe QD arrays in both methods exhibited photoluminescence in the visible and near-infrared spectra, with emissions from 780 nm to about 1020 nm. Incorporation of Ge, confirmed by Raman spectroscopy, induced a shift towards higher wavelengths in the light emission. Time-resolved photoluminescence measurements indicated average-weighted lifetimes ranging from 34  $\mu\text{s}$  to 220  $\mu\text{s}$ , with a decreasing trend noted with increasing Ge concentrations. Experimentally observed differences in photoluminescence peak intensity and width for the two fabrication approaches can be connected to SiGe QD size distributions and matrix effects.

**Keywords:** surface Debye temperature, low energy electron diffraction (LEED), semiconductor defects, epitaxial films, quantum dots, SiGe quantum dots, photoluminescence, Raman spectroscopy.



## Summary for Lay Audience

Novel semiconductor materials and devices have been continuously changing our everyday life and society. Defects can affect semiconductor performance in many positive ways and some negative ways. This thesis investigates the relationship between defects in semiconductor crystals and the Debye temperature. Defects are defined as atomic level imperfections such as impurities or disorder in the crystalline structure. To illustrate, imagine a solid composed of billions of orderly cubes arranged side by side. We expect atoms to occupy the eight vertices of each cube. However, if one atom is located at the center of the cube while the other seven are at the vertices, we have what is referred to as a defect. The Debye temperature of a solid serves as a metric for gauging the extent of atomic jiggling and vibration within a material. It provides insights into the average energy of these minuscule particles and helps in comprehending their behavior when the material undergoes heating or cooling. Therefore, employing surface analysis to measure Debye temperature and ion beam techniques to quantify the concentration of defects, I found that a higher defect concentration leads to a lower Debye temperature, suggesting that measurements of the Debye temperature can be used to estimate the concentration of defects.

I fabricated silicon-germanium quantum dots, which are nanometer-scale particles, embedded in a silicon oxide matrix. Light emission of these quantum dots is enhanced significantly compared to the bulk analogs. This is particularly relevant today, given that the primary hardware in cutting-edge technologies like artificial intelligence and big data involves integrated optical circuits known as system-on-chip. Within these chips, various components, such as a CPU, memory, and sensors, coexist and communicate through metallic wires. Shifting their communication to light could lead to reduced power consumption and enhanced processing power. I explored how the light emission of these SiGe quantum dots correlates with the concentration of germanium. In the fabrication process, I discovered a more effective procedure to thermally process these samples to incorporate germanium into the quantum dots. Furthermore, I demonstrated that adjusting the amount of germanium allows us to modify the wavelength of the light emitted from the quantum dots.

## Co-Authorship Statement

Chapter 1 contains the motivation of this thesis, a brief theoretical background, and a literature review about part of the topic covered in this thesis. The chapter was written entirely by the candidate with revision made by his supervisors.

In Chapter 2, the experimental methods are summarized. It contains the main experimental techniques that were employed to prepare and study the samples. The chapter was written entirely by the candidate with revision made by his supervisors.

Chapter 3 is a reproduction of a published manuscript by the candidate. He contributed to this through the design and execution of RBS experiments, as well as the analysis of RBS data. Additionally, he played a key role in performing LEED analysis and contributed significantly to the manuscript writing process. Nazban Darukhanawalla made valuable contributions by conducting RBS experiments. James M. Gaudet, Peter J. Simpson, and Marc H. Weber conducted PAS experiments and carried out the associated data analysis. Guenevere O'Hara and Paige Harford conducted LEED experiments. Greg Hall contributed to the project by developing the necessary software for LEED data acquisition. Jozef Ociepa, Peter J. Simpson, and Lyudmila V. Goncharova provided essential input during the revision process and offered valuable supervision throughout the project.

The research in Chapter 4 was primarily led by the candidate, who worked in every aspect, from sample preparation to data collection and analysis. Two specific contributions were made by external collaborators. The PL measurement of the sample Si\_1100C\_FG at the Horiba facility, utilizing a different detector, was conducted by Alex Siemiarczuk. Additionally, Raman measurements were carried out by Mauritz Van Zyl, under the supervision of Sean Shieh. His supervisors contributed significantly in discussing the results and reviewing the chapter.

In Chapter 5, the candidate calibrated the deposition rate in the PECVD system at Western Nanofab, made the sample preparation, and carried out all PL measurements and analysis. XRD and Raman results were also analyzed by the candidate, but XRD was measured at Surface Science Western by Vahid Dehnavi and Raman was measured by Mauritz Van Zyl, supervised by Sean Shieh. Chapter 6 was written entirely by the candidate with revision made by his supervisors.

## Acknowledgements

It's impossible for me to forget the first day I met Prof. Goncharova and Prof. Simpson during a video call interview in 2018, part of the Ph.D. admission process at Western. I shared my dream of becoming a scientist and studying abroad. I'm grateful for them accepting me as their student and making my dream a reality. I've been fortunate to have them supervise me, not just technically but also providing support and advice whenever I needed it. Thank you, Prof. Goncharova and Prof. Simpson.

This journey wouldn't be possible without the constant support of my lovely wife Fernanda. I often joke about being crazy for leaving a stable job, family, surfing, and friends to move to Canada, but she's even crazier for joining me! Thank you for being an integral part of this journey with your patience and unconditional love. I also would like to thank my parents for their role model, integrity, and love. A special thanks to my mother-in-law who came to Canada when Luca was born and for taking care of Fernanda and Luca for two months in Brazil when I was here in Canada wrapping the thesis up.

I would like to thank Jack Hendriks, for his technical support in running the Tandatron accelerator that was crucial to my research, and for all the nice chats we had about politics, traveling, cars, and advice about life in Canada in general. I have also had the pleasure of working in the Western Nanofabrication Facility and would like to thank Todd Simpson and Tim Goldhawk for all their help. Many thanks to Sean Shieh and Mauritz Van Zyl for measuring my samples with Raman spectroscopy and to Marc Weber at Washington State University and James Gaudet for their valuable help with PAS measurements and analysis. I want to thank Vahid Dehnavi at Surface Science Western for XRD measurements, and Alex Siemiarczuk at Horiba for measuring PL on one of my samples. Last but not least, I want to express my gratitude to Jozef and Bart from OCI Vacuum Microengineering Inc. for their collaboration at the beginning of my Ph.D. and for their continued professional support since I joined the company approximately a year ago.

# Table of Contents

<b>Abstract</b>	<b>ii</b>
<b>Summary for Lay Audience</b>	<b>iii</b>
<b>Co-Authorship Statement</b>	<b>iv</b>
<b>Acknowledgements</b>	<b>v</b>
<b>Table of Contents</b>	<b>vi</b>
<b>List of Tables</b>	<b>viii</b>
<b>List of Figures</b>	<b>ix</b>
<b>List of Abbreviations</b>	<b>xii</b>
<b>1 Introduction</b>	<b>1</b>
1.1 Motivation . . . . .	1
1.2 Silicon and germanium QD fundamentals . . . . .	5
1.3 Silicon-germanium QDs formed by ion implantation . . . . .	10
1.4 Scope of the Thesis . . . . .	17
1.5 References . . . . .	19
<b>2 Experimental methods</b>	<b>23</b>
2.1 Fabrication methods . . . . .	23
2.1.1 Ion implantation . . . . .	23
2.1.2 Plasma-enhanced chemical vapour deposition (PECVD) . . . . .	26
2.2 Characterization methods . . . . .	28
2.2.1 Rutherford backscattering spectrometry (RBS) . . . . .	28
2.2.2 Channelling . . . . .	32
2.2.3 Photoluminescence (PL) . . . . .	34
2.2.4 Low energy electron diffraction (LEED) . . . . .	37
2.2.5 Other techniques . . . . .	38
2.3 References . . . . .	40
<b>3 Surface Debye temperature determination from LEED: correlation to defects in epitaxial films</b>	<b>43</b>

3.1	Introduction . . . . .	43
3.2	Experimental details . . . . .	46
3.3	Results and discussion . . . . .	48
3.4	Conclusions . . . . .	58
3.5	References . . . . .	59
<b>4</b>	<b>Light emission from SiGe quantum structures in SiO<sub>2</sub> produced by Si and Ge co-implantation</b>	<b>62</b>
4.1	Introduction . . . . .	62
4.2	Experimental details . . . . .	65
4.3	Results and discussion . . . . .	67
4.4	Conclusions . . . . .	78
4.5	References . . . . .	80
<b>5</b>	<b>Light emission from SiGe quantum structures in SiO<sub>2</sub> produced by PECVD and Ge implantation</b>	<b>82</b>
5.1	Introduction . . . . .	82
5.2	Experimental details . . . . .	83
5.3	Results and discussion . . . . .	85
5.4	Conclusions . . . . .	94
5.5	References . . . . .	96
<b>6</b>	<b>Conclusions and future work</b>	<b>99</b>
6.1	Conclusions . . . . .	99
6.2	Future work . . . . .	102
	<b>Appendix A Copyrights</b>	<b>103</b>
	<b>Curriculum Vitae</b>	<b>104</b>

# List of Tables

1.1	Summary of papers reviewed in this section. . . . .	16
3.1	Fitting results for all spots and energies used in LEED measurements. The absolute value of the slope is presented in $\times 10^{-3} \text{ K}^{-1}$ and its standard deviation is in $\times 10^{-5} \text{ K}^{-1}$ . . . . .	49
3.2	Surface $\theta_D$ and its total uncertainty $\delta\theta_D$ calculated from LEED measurements at spots (-1/2 0) and (1 1) for incident electron energies of 80 eV, 95 eV and 150 eV. All values in Kelvin. . . . .	50
3.3	Comparison between surface and bulk $\theta_D$ for several semiconductors and metals. Adapted from [3], except where indicated. . . . .	50
3.4	Summary of defect areal density calculations from RBS and ion channeling measurements using equation (3.4). NA stands for “not applicable”. . . . .	53
3.5	Summary of defect areal densities obtained from PAS measurements using POSTRAP. . . . .	55
3.6	Surface Debye temperatures ( $\theta_D$ ) calculated at spot (0 1) from LEED patterns, compared to published results for bulk Si (001), concentration of defects at the surface from RBS measurements, and concentration of defects obtained from PAS measurements for near-surface layers. * See discussion of the interpretation of this number in the text. . . . .	56
4.1	Ge implanted dose for each sample in this work. The sample nomenclature is also presented, being labeled chronologically. . . . .	66
4.2	Peak emission wavelength ( $\lambda_{\text{max}}$ ) obtained from PL spectra in the UV-Vis and NIR ranges. . . . .	71
4.3	Parameters obtained from double exponential fit ( $y = y_0 + A_1 e^{-t/t_1} + A_2 e^{-t/t_2}$ ) of time-resolved photoluminescence decays. . . . .	75
5.1	PECVD $\text{SiO}_x$ deposition parameters. . . . .	84
5.2	Concentration of Ge $x$ determined from the chemical formula $\text{Si}_{1-x}\text{Ge}_x$ . . . . .	86
5.3	Samples without germanium with their wavelength of maximum emission ( $\lambda_{\text{max}}$ ) and QD diameter $D$ . . . . .	89
5.4	Parameters obtained from double exponential fit ( $y = y_0 + A_1 e^{-t/t_1} + A_2 e^{-t/t_2}$ ) of time-resolved photoluminescence decays along with the average-weighted lifetime. . . . .	91

# List of Figures

1.1	(a) Cross-section of a MOSFET. (b) CMOS inverter schematic. (c) Cross-section of a CMOS inverter. Adapted from [5] and [6]. . . . .	2
1.2	The density of transistors in the IC versus time. Adapted from [10]. . . . .	3
1.3	Intel i7 internal block diagram (left) and die photo (right). Adapted from [12]. . . . .	4
1.4	Band structures of (a) silicon and (b) germanium showing valence band maxima (VBM) and conduction band minima (CBM). Adapted from [26]. . . . .	6
1.5	(a) Quantum structures that exhibit quantum confinement (QC) in 2D, 1D, and 0D. (b) Quantum structures and a bulk (3D) density of states $\rho(E)$ . Adapted from [32]. . . . .	6
1.6	(a) Normalized photoluminescence spectra for samples annealed at 500°C, and (b) change in Si-QS size with annealing temperature. Adapted from [32]. . . . .	8
1.7	Bandgap as a function of germanium atomic fraction for different $\text{Si}_{1-x}\text{Ge}_x$ systems. The system is unstrained for gold and silver diamonds, circles are strained undoped and squares are for heavily doped strained systems. Adapted from [37]. . . . .	9
1.8	X-ray diffraction from SiGe precipitates in $\text{SiO}_2$ . Equal doses ( $3 \times 10^{17} \text{ cm}^{-2}$ ) of Si (215 keV) and Ge (500 keV) were implanted and the sample was annealed at 1100 °C for 1h. Reproduced from [40]. . . . .	10
1.9	Transmission electron microscopy (TEM) of SiGe precipitates in $\text{SiO}_2$ after annealing at (a) 1100 °C and (b) 1000 °C for 1h. These samples have been implanted with Si (215 keV, $3 \times 10^{17} \text{ cm}^{-2}$ ) and Ge (500 keV, $3 \times 10^{17} \text{ cm}^{-2}$ ). Reproduced from [40]. . . . .	11
1.10	(a) Dependence of the Raman spectra of $\text{Si}_{1-x}\text{Ge}_x$ nanocrystals on the Ge content. (b) PL spectra of $\text{Si}_{1-x}\text{Ge}_x$ nanocrystals with various Ge contents. Adapted from [41]. . . . .	12
1.11	Size distribution, in nanometers, of the nanocrystals in the sample annealed for 1 h (a) and 3 h (b). Insets show the selected area diffraction patterns. Adapted from [45]. . . . .	13
1.12	Raman spectroscopy measurements of the samples made by Zhong et al. [46]. Adapted from [46]. . . . .	14
1.13	(a) Room temperature PL spectra. (b) Normalized time-resolved PL decays at 675 nm. Adapted from [46]. . . . .	15
1.14	TEM images and histograms of quantum dot diameters for (a) 9 at.% annealed at 700 °C and (b) 12 at.% annealed at 900 °C. Adapted from [49]. . . . .	16

2.1	(a) Approximation of the depth distribution of implanted atoms in an amorphous target. Adapted from [3]. (b) Simulated Ge ions depth distribution when implanted into a SiO <sub>2</sub> target. Simulation performed with SRIM [4]. . . . .	24
2.2	Tandetron accelerator schematic at Western Univeristy. . . . .	25
2.3	PECVD reactor schematic illustrating its basic components. Copied from [9]. . . . .	27
2.4	Schematic representation of an elastic collision between a projectile of mass $M_1$ , velocity $v_0$ , and energy $E_0$ and a target of mass $M_2$ which is initially at rest. After the collision, the projectile and the target mass have velocities and energies $v_1$ , $E_1$ and $v_2$ , $E_2$ , respectively. The angles $\theta$ and $\phi$ are positive as shown. Reproduced from [11]. . . . .	28
2.5	Example of a typical RBS spectrum pointing out the edge slopes and the higher number of count as the film depth increases (lower peak energies) [11]. . . . .	31
2.6	A silicon crystal is seen from different angles. On the left, it is viewed from a random angle so that the structure appears to be amorphous. In the middle, the sample is rotated and channels formed by horizontal planes can be seen. On the right, with proper angles, channels are formed by lines of silicon atoms. Adapted from [11]. . . . .	32
2.7	Comparison between a channeled (aligned) spectrum and a random spectrum from crystalline Si covered with 130 nm SiO <sub>2</sub> . The peak at channel 200 comes from Si in the oxide. The peak at channel 90 is from oxygen. Adapted from [11]. . . . .	33
2.8	Basic representation of a radiative recombination process (photoluminescence), where the incident light beam is represented in blue, while the emitted light due to the recombination process is represented in green. Adapted from [14]. . . . .	35
2.9	Efficiency properties of the photodetectors used in this work: (a) PMT R928 quantum efficiency, (b) DSS-IGA020 photodiode responsivity. Reproduced from [17] and [18]. . . . .	36
2.10	Horiba Fluorolog-QM-75-22 system schematic used in this work. . . . .	36
2.11	(a) Working principle schematic of LEED. (b) Example of a LEED pattern. Adapted from [22]. . . . .	37
2.12	LEED spectrometer used in this work. Copied from [24]. . . . .	38
3.1	LEED diffraction intensities measured at spot (0 1) as a function of temperature for samples (a) Si (001), (b) SoS 1.0 $\mu\text{m}$ , and (c) SoS 0.6 $\mu\text{m}$ . . . . .	48
3.2	Calculated surface Debye temperature from LEED measurements at 80 eV, 95 eV and 150 eV incident electron energy, at spots (a) (0 1), (b) (-1/2 0), and (c) (1 1). Table 3.2 presents a summary of surface $\theta_D$ measured for these energies. . . . .	49
3.3	Random and channeling spectra along with the normalized yield $\chi$ on the right scale, of samples (a) Si (001), (b) SoS 1.0 $\mu\text{m}$ , and (c) SoS 0.6 $\mu\text{m}$ . . . . .	52
3.4	S-parameter as a function of incident positron energy and depth from 0 to 30 keV. Solid lines show results of modeling using POSTRAP. . . . .	54
4.1	Process flow illustrating the sample preparation in this work. Si was implanted with $8.05 \times 10^{16}$ ions/cm <sup>2</sup> at 40 keV. Ge implanted doses varied from $1.30 \times 10^{15}$ to $2.10 \times 10^{16}$ ions/cm <sup>2</sup> , at 55 keV. The diagram also includes the nomenclature for each sample set, where “X” stands for Ge concentration. “A” stands for anneal. . . . .	65



4.2	PL spectra in the UV-Vis range of (a) sample set SiAGeXA (thermal annealing between Si and Ge implants) and (b) reference sample plus sample set SiGeXAA (thermal annealing after Si and Ge implants). . . . .	67
4.3	PL spectra in the NIR range of (a) sample set SiAGeXA and (b) reference sample plus sample set SiGeXAA. Note different intensity scales. . . . .	68
4.4	Emission spectrum of the reference sample excited with 270 nm and measured with the PMT R5509-73. . . . .	69
4.5	Simulated depth profiles from RBS measurements of sample Si_1100C_FG before and after annealing. . . . .	70
4.6	Wavelength of maximum emission, $\lambda_{\max}$ , plotted for all samples. (a) data obtained from UV-Vis emission and (b) from NIR emission. The red dashed line separates the different sample sets. . . . .	72
4.7	(a) RBS results of samples SiAGe2.0A and SiGe2.0AA. (b) Simulated depth profile of these measurements using MEISwin software [16]. . . . .	73
4.8	(a) Time-resolved photoluminescence decays measured at room temperature using a pulsed LED with wavelength of $370 \pm 10$ nm. (b) TRPL experimental data from the reference sample fitted with different exponential decays. . . . .	74
4.9	Weighted average lifetime $\bar{t}_w = (A_1 t_1 + A_2 t_2)/(A_1 + A_2)$ for each sample, where $A_1$ and $A_2$ are the coefficients calculated from the exponential fitting. . . . .	76
4.10	Raman spectra of (a) sample set SiAGeXA (b) sample set SiGeXAA, with the reference sample for comparison. . . . .	77
5.1	GIXRD scans of selected samples from Gamma PECVD deposition regime. . . . .	86
5.2	Raman spectra of samples (a) without Ge and (b) with Ge implanted at 8 at.%. . . . .	88
5.3	Steady-state PL on selected samples in the (a) UV-Vis and (b) NIR. . . . .	89
5.4	Wavelength of maximum emission, $\lambda_{\max}$ , obtained during steady-state PL characterization. Samples Alpha, Beta, and Gamma with Ge 8 at.% did not have their $\lambda_{\max}$ determined because of their weak emission. . . . .	90
5.5	Average-weighted lifetime $\bar{t}_w = (A_1 t_1 + A_2 t_2)/(A_1 + A_2)$ for each sample. . . . .	92
5.6	Steady-state PL comparison between (a) SiGeXAA and (b) Alpha_X% sample sets. Samples in (a) were fabricated by co-implant of Si and Ge while samples in (b) were fabricated by a combination of PECVD plus Ge implant. . . . .	93

# List of Abbreviations

$\theta_D$	- Debye temperature
at.%	- atomic percent (percentage of one kind of atom relative to the total number of atoms)
CMOS	- complementary metal-oxide-semiconductor
CVD	- chemical vapour deposition
$E_g$	- bandgap energy
GIXRD	- grazing incidence X-ray diffraction
HRTEM	- high-resolution transmission electron microscopy
ICs	- integrated circuits
LEED	- low energy electron diffraction
$N_d$	- concentration of defects
NIR	- near-infrared
PAS	- positron annihilation spectroscopy
PECVD	- plasma-enhanced chemical vapour deposition
PL	- photoluminescence
PMT	- photomultiplier tube
QC	- quantum confinement
QD	- quantum dot
QS	- quantum structure
RBS	- Rutherford backscattering spectrometry
SRIM	- Stopping and Range of Ions in Matter
SSD	- solid-state detector
TEM	- transmission electron microscopy
TRPL	- time-resolved photoluminescence
UHV	- ultra-high vacuum
UV-Vis	- ultra-violet to visible
XRD	- X-ray diffraction

# Chapter 1

## Introduction

The introductory chapter of this thesis has three main sections. The first two sections cover the research motivation, aiming to contextualize the topic of this project, and describe essential theoretical principles that are relevant to the thesis. The third section summarizes the literature on the state-of-the-art in fabrication and characterization of SiGe quantum structures that will be useful to the scope of this work.

### 1.1 Motivation

In recent years, many advancements have been accomplished in the fields of information technology, health sciences, and defense systems due to the study of fundamental physical properties of nanomaterials. As the optical, electronic and other properties can be dramatically different when particle size drops below a few nanometers, these novel properties can be explored for a variety of applications. For instance, we can mention the application of titanium dioxide and zinc oxide nanoparticles in sunscreens [1], copper nanoparticles as a safer, cheaper, and more reliable alternative to lead-based solder materials commonly used to assemble electronic components [2], and the use of nanomaterials in catalysis [3]. Nanoparticles find their applications in diverse economic sectors [4]: nanomaterials in the environment, food industry and packaging, in health care and cosmetics, in medicine, nanomaterials for building and protection, for clothing and textile products and nanomaterials for smart electronics and sensors.

Among all kinds of applications in the different industries, one of the main drivers for the development of nanomaterials was the microelectronics industry, which uses semiconductor

materials to manufacture integrated circuits (ICs). The main electronic component of this industry is the MOSFET (metal-oxide-semiconductor field-effect-transistor) and the association of two MOSFETs forms the basic block of CMOS (complementary metal-oxide-semiconductor) technology, that is the CMOS inverter. Figure 1.1(a) shows the cross-section of this component, and Figures 1.1(b) and 1.1(c) present the schematic of the CMOS inverter, and its cross-section, respectively.

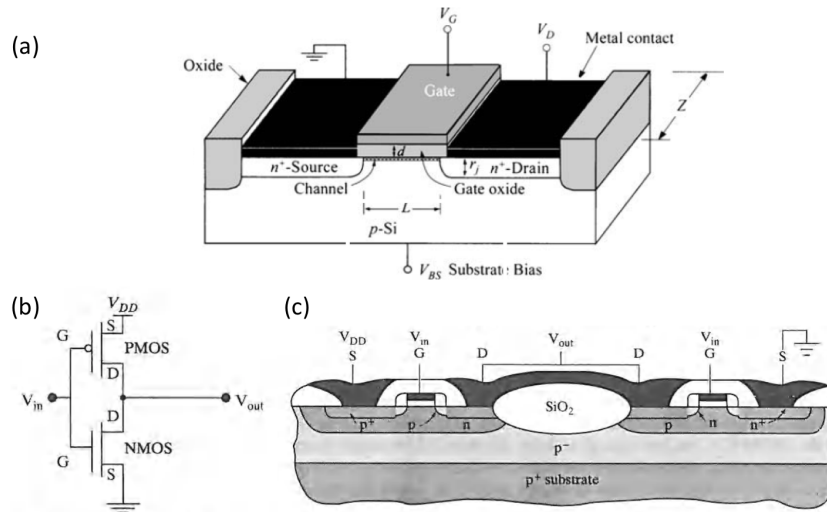


Figure 1.1: (a) Cross-section of a MOSFET. (b) CMOS inverter schematic. (c) Cross-section of a CMOS inverter. Adapted from [5] and [6].

The CMOS technology led the semiconductor industry to impressive achievements in the field of materials science along with its development. In fact, since two decades ago, the microelectronics industry has worked in the nanoscale, as reported by the International Technology Roadmap for Semiconductors (ITRS) [7]. For instance, from 2007 until 2009, the most used technologies were ones with half pitch smaller than 80 nm. The pitch of a certain technology is proportional to the channel length  $L$  of the transistor (see Figure 1.1 (a)). Consider the technological node of 65 nm, which was used to make Intel Core 2 Duo microprocessors: transistors have a channel length of approximately 30 nm in this node. In this industry, there is also a trend of feature size miniaturization over time, which enables more components to be made in the same chip area. Indeed, the microelectronics industry has been keeping to this trend over time as evidenced by Figure 1.2, where we can observe the number of transistors in various microprocessors along the years. This relationship was first observed by Gordon Moore in 1965 [8].

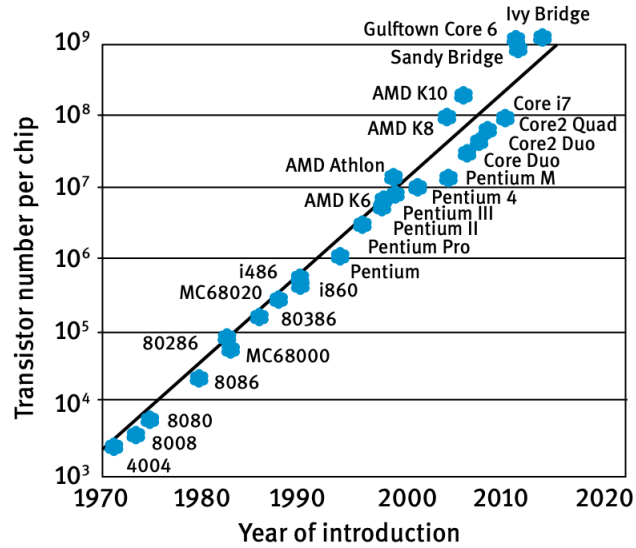


Figure 1.2: The density of transistors in the IC versus time. Adapted from [10].

He wrote that the number of components in an IC was expected to double every year. However, in 1975, he published another paper [9] in which he wrote that the number of components per chip might double every two years. This is the so-called Moore's law, even though it is not a physics law such as Ohm's law, for example. Moore's law is much more a guideline that sets the pace for industry development.

Based on this tendency of growth dictated by Moore's law, the nanoelectronics industry needs alternatives to maintain the advancements in performance, power consumption, and higher operating speeds. Currently, the majority of microprocessors have chip multiprocessor (CMP) architectures, where a chip is formed by different components where the communication among them is made by electrical signals. For instance, Figure 1.3 shows the Core i7 microprocessor with four processing units, a graphic processor, memory, and other components. According to Miller [11], light could be used to carry information over relatively long distances (in the order of millimeters) with lower power consumption compared to metal conductor wires of Cu or Al. Therefore, a device like the one cited above is an example where we can integrate photonics and electronics to increase the chip speed and decrease the power consumption by making the communication among chip components using photons.

The main semiconductor used in the electronic industry today is silicon (Si), since its interface with silicon oxide has a low concentration of defects and the combination of different

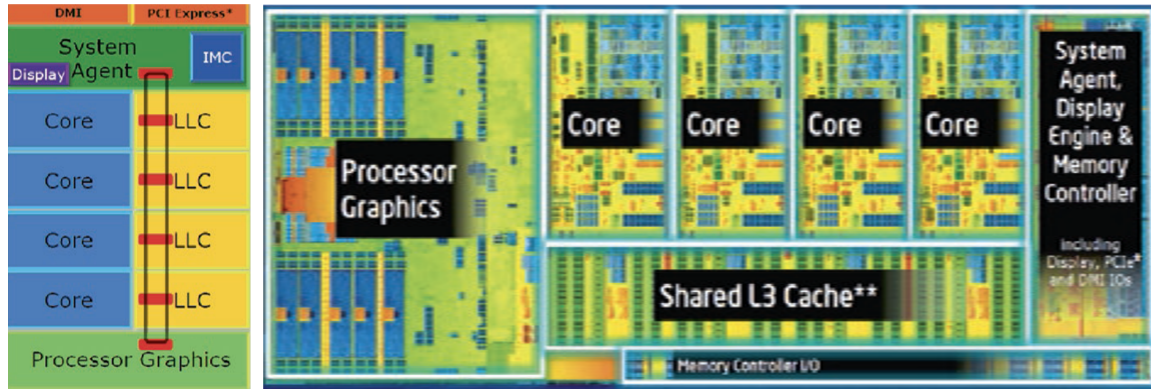


Figure 1.3: Intel i7 internal block diagram (left) and die photo (right). Adapted from [12].

dopants and doping levels makes silicon an excellent material for electronics. However, it lacks light emission due to being an indirect bandgap semiconductor. Many approaches have been explored in order to improve light emission from Si, such as the fabrication of porous silicon [13] and silicon nanowires [14], and the major advancements in the field of silicon photonics have come from work on silicon nanocrystals due to the quantum confinement (QC) effect [15]. A nanostructure that exhibits the quantum confinement effect is called a quantum structure (QS), and it is called as a quantum dot (QD) if the carriers have zero degrees of freedom, as defined by Reed et al. [16] in 1986. More details about quantum confinement and quantum structures will be discussed in the next section.

Using semiconductor QDs to enhance computational power in the quantum information processing is another growing field. [17], [18]. Indeed, this option is not just academic research, since there is an effort from many companies such as Intel, Google, and IBM to make quantum computation a reality. According to the International Roadmap for Devices and Systems [19], quantum dots can be used to process information as qubits.

The semiconductor industry plays a significant role in the world economy. The global semiconductor sector's total revenue was set to increase from US\$ 534B in 2023 to US\$ 624B in 2024 according to a report from the consulting firm Gartner [20]. In this huge market, the participation of compound semiconductors like GaAs, GaN, and SiC, for example, was 43B US\$ in 2022 [21], and the market share of organic electronics (mainly concentrated in display applications) grew to 40B US\$ in the end of 2020 [22]. Silicon-based electronics form the major participant of the electronic industry, with more than 80% of market share. This fact

is very important because it means that the state of the art for nanoelectronics production is based on silicon. Consequently, future nanoelectronics and optoelectronics processing should be compatible with current IC production technology.

One of the key techniques in current IC manufacturing is ion implantation [23]. It is used to modify the electrical properties of specific regions on the silicon substrate by introducing donor or acceptor atoms in a precise way. This process, called doping, is necessary to make transistors that are used to form the logic blocks of CMOS technology. Ion implantation is a versatile techniques that allows sample fabrication beyond the chemical solubility limit, enabling the combination of different chemical elements to fabricate quantum structures (QDs) that would not be possible to achieve through chemical reactions [24]. The widespread application of ion implantation in current IC manufacturing, along with its ability to precisely modify material properties, motivates me to choose this technique for producing my samples.

## 1.2 Silicon and germanium QD fundamentals

Before diving into more specialized topics, it is essential to provide a brief summary of main concepts that serve as foundational elements for this thesis. Silicon and germanium, both belonging to the group IV of the periodic table, are semiconductors having the diamond crystal structure characterized by a face-centered cubic lattice. Si and Ge electronic band structure<sup>1</sup> is presented in Figure 1.4. We can observe that for both elements we have valence band maxima (VBM) and conduction band minima (CBM) at different values of the wave vector  $\vec{k}$ . Then, electronic transitions between the valence and conduction band must involve phonons in order to conserve momentum. Materials that present an offset between VBM and CBM are called indirect bandgap materials. The bandgap is defined as the energy difference between VBM and CBM, being equal at room temperature to 1.12 eV for Si and 0.66 eV for Ge.

The description presented so far applies for bulk semiconductors where electrons can move in the three dimensions (3D) and the density of states  $\rho(E)$  is continuous. When we spatially confine the electrons in one of their dimensions,  $\rho(E)$  is quantized, and we have so-called quan-

---

<sup>1</sup>Just as chemists have been working with atomic orbitals to study and describe electron behaviours in chemical reactions, condensed-matter physicists have developed a theory to describe the properties of solids in terms of energy bands. More details can be found in [25].

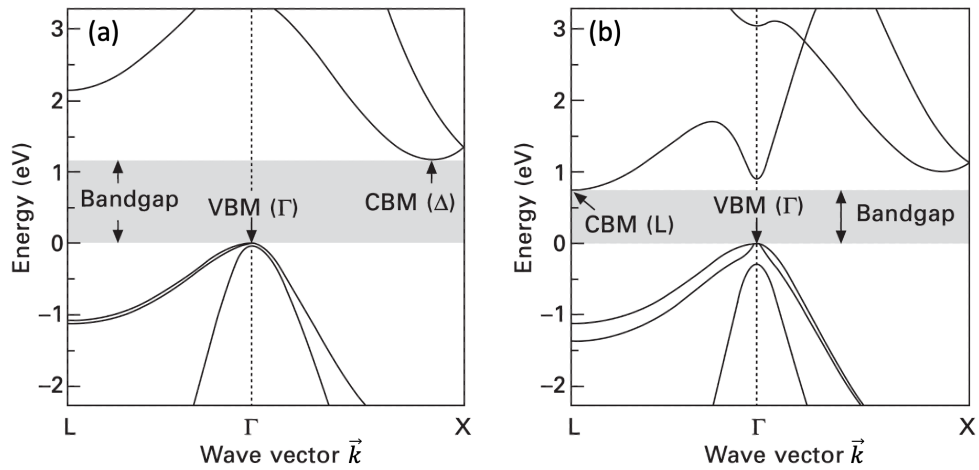


Figure 1.4: Band structures of (a) silicon and (b) germanium showing valence band maxima (VBM) and conduction band minima (CBM). Adapted from [26].

tum wells (2D). If we continue to increase the number of dimensions that confine the electrons, we obtain quantum wires (1D) and, finally, quantum dots (0D), as illustrated in Figure 1.5. In the subsequent discussion, our focus shall be exclusively directed towards quantum dots.

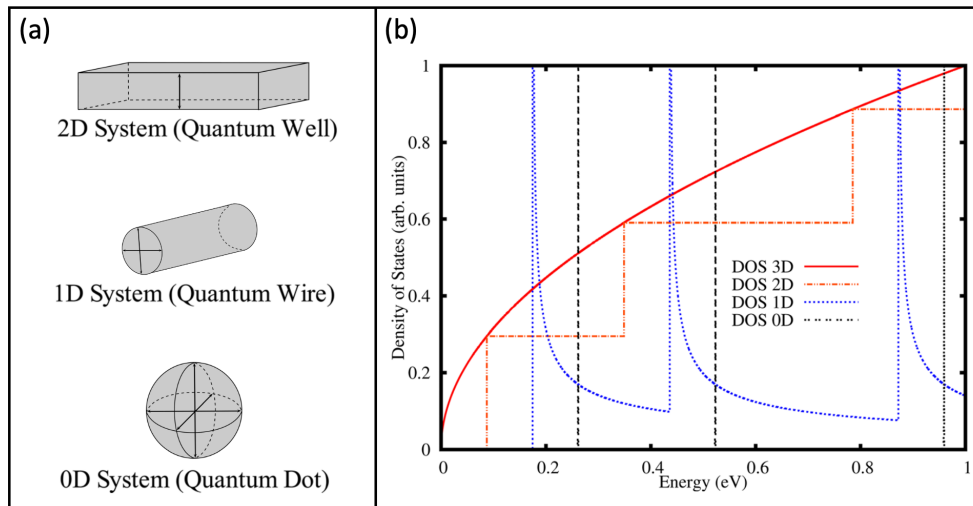


Figure 1.5: (a) Quantum structures that exhibit quantum confinement (QC) in 2D, 1D, and 0D. (b) Quantum structures and a bulk (3D) density of states  $\rho(E)$ . Adapted from [32].

This emphasis is warranted by the fact that the nanoparticles under consideration in this study



exhibit dimensions where quantum confinement manifests in all three-dimensions.

Given these alterations in the density of states and in the band structure by the reduction of the system dimensions, we can approximate small crystals inside a layer of insulating material as quantum dots. When electrons are confined in the QD, the uncertainty in position is reduced and, consequently, the uncertainty in momentum (which is proportional to the uncertainty in  $\vec{k}$ ) increases due to the Heisenberg's uncertainty principle. In this case, the probability to have energy transitions involving photon emission increases. Then, even in materials that are poor light emitters (indirect band gap), we can use quantum confinement effects to have light emission.

A straightforward way to investigate quantum confinement (QC) effect is using photoluminescence (PL) characterization. Photoluminescence is a technique where electrons are elevated to higher energy levels after absorbing photons of energy higher than a bandgap. In this process, when these electrons return to their lower energy or ground states, they release the excess energy in the form of photons, which is detected as emitted light. Therefore, the change in the emitted light wavelength may be caused by dimensional or structural changes in the QS related to QC effects. More details about this PL are provided in the next chapter.

Our research group has been studying silicon QDs for a considerable time [28, 29, 30, 31, 32]. For instance, Figure 1.6a shows photoluminescence measurements for different Si-QDs in a silicon nitride matrix. All samples were annealed at 500 °C for 30 min in a nitrogen atmosphere. According to the composition of each sample, Si-QDs of different sizes are formed, as evidenced by Figure 1.6b. Then, we can observe a blue shift as the quantum dot size decreases, which is characteristic of the quantum confinement effect. This is an important property of this kind of system: it is possible to adjust the wavelength of the emitted light according to the required application.

Various theoretical models [33, 34, 35], have been applied to semiconductor quantum structures. No single model can encompass all semiconductor QDs due to their variety of fabrication methods. One approach that has been used to associate the diameter  $D$  of the QD to the maximum of the photoluminescence peak,  $E_g(D)$ , is

$$E_g(D) = E_g(\infty) + A/D^2, \quad (1.1)$$

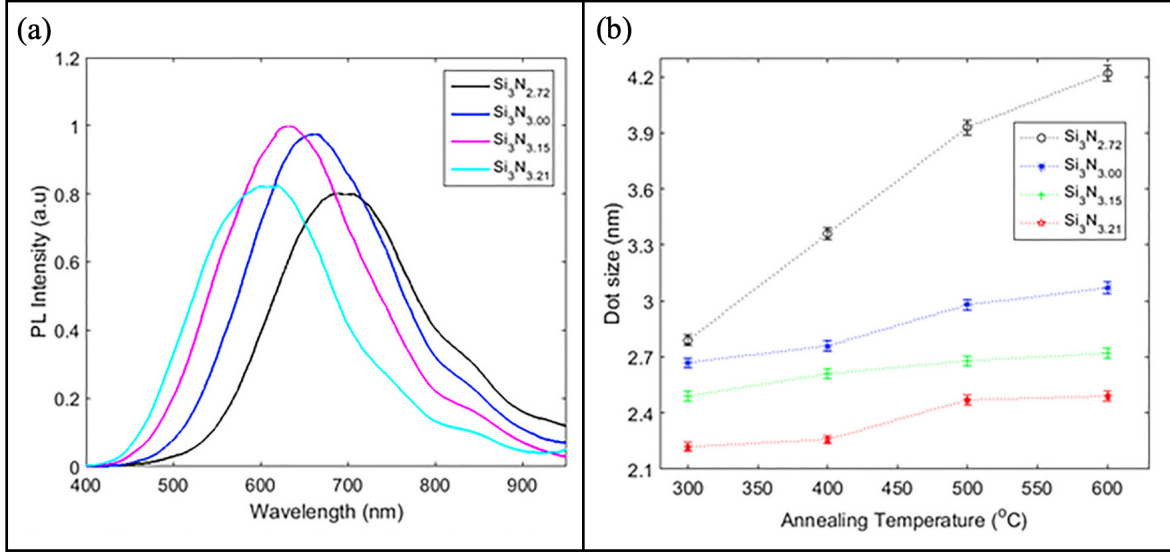


Figure 1.6: (a) Normalized photoluminescence spectra for samples annealed at 500°C, and (b) change in Si-QS size with annealing temperature. Adapted from [32].

where  $E_g(\infty)$  is the bandgap of the bulk material, and  $A$  is a constant that depends on the material and its confinement regime. Barbagiovanni et al. [30] suggested three different regimes of quantum confinement: weak, medium, and strong. Different QC regimes have different values for  $A$  according to the semiconductor material and its crystallinity. Quantum confinement regime is assigned based on the dimension of the QS in relation to the Bohr radius of the exciton in the material. The Bohr radius of the exciton,  $a_B^X$ , is [36]:

$$a_B^X = a_B^H \epsilon \frac{m_0}{\mu}, \quad (1.2)$$

where  $a_B^H$  is the Bohr radius in the hydrogen atom ( $0.5292 \text{ \AA}$ ),  $\epsilon$  is the dielectric constant of the material,  $m_0$  is the mass of the electron and  $\mu$  is the reduced mass in terms of the electron and hole effective mass. For example, QDs with radius much smaller than the exciton Bohr radius have strong quantum confinement.

The advantage of having a compound QS is the possibility of tuning the emission wavelength not only by its size but also by the relative concentration of each element. Figure 1.7 shows the bandgap as a function of germanium fraction for three different types of Si<sub>1-x</sub>Ge<sub>x</sub>: unstrained (diamond symbol), strained undoped (circles), and strained heavily doped (squares).

The plotted values for  $E_g$  as a function of Ge content came from several studies for bulk

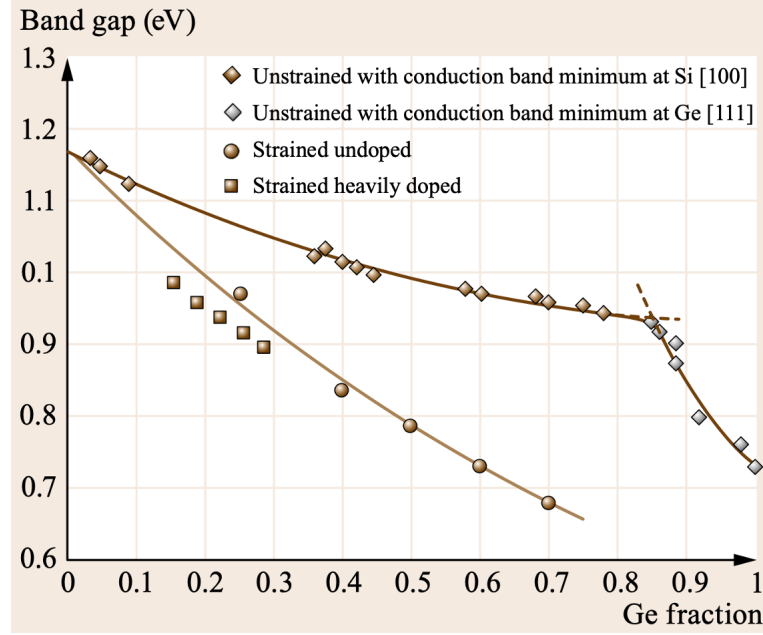


Figure 1.7: Bandgap as a function of germanium atomic fraction for different  $\text{Si}_{1-x}\text{Ge}_x$  systems. The system is unstrained for gold and silver diamonds, circles are strained undoped and squares are for heavily doped strained systems. Adapted from [37].

$\text{Si}_{1-x}\text{Ge}_x$  alloys grown on silicon. These studies were compiled by Haddara et al. in [37]. In this paper, the author fits the variation of bandgap  $E_g$  with germanium content for unstrained  $\text{Si}_{1-x}\text{Ge}_x$  using the following empirical equation:

$$E_g(x) = \begin{cases} 1.17 - 0.47x + 0.24x^2, & x < 0.85 \\ 5.88 - 9.58x + 4.43x^2, & x > 0.85 \end{cases} . \quad (1.3)$$

According to the author, the transition at  $x = 0.85$  is due to the minimum of the conduction band switching from the [100] direction associated with Si to the [111] direction associated with Ge. For strained  $\text{Si}_{1-x}\text{Ge}_x$  the empirical fit for the bandgap is

$$E_g(x) = 1.17 - 0.94x + 0.34x^2 . \quad (1.4)$$

In the next section, I provide a brief review of the literature on silicon-germanium quantum structures, fabrication, and characterization.

### 1.3 Silicon-germanium Qs formed by ion implantation

A range of methods has been employed for the fabrication of SiGe quantum structures, spanning from solution-based chemical techniques like colloidal synthesis [38] to ultra-high vacuum techniques such as molecular beam epitaxy (MBE) [39]. Given that the primary emphasis of this research is on fabricating SiGe Qs using ion implantation in an amorphous SiO<sub>2</sub> matrix, this subsection will provide a summary of previous work related to both fabrication and characterization methods pertinent to this research.

The literature regarding SiGe Qs formed by ion implantation into insulating matrices like silicon oxide, silicon nitride and aluminum oxide is not extensive. To the best of our knowledge, the first work about this particular system was published in 1995 [40]. In that work, Si<sup>+</sup> and Ge<sup>+</sup> were implanted into amorphous silicon dioxide and were postannealed at 1100 °C or at 1000 °C for 1 h in the Ar atmosphere with 5% H<sub>2</sub>. Figure 1.8 presents an x-ray diffraction (XRD) measurement that was performed in order to show the presence of SiGe crystals. The focus of Zhu et al.'s research was to show the effect of the annealing temperature on the

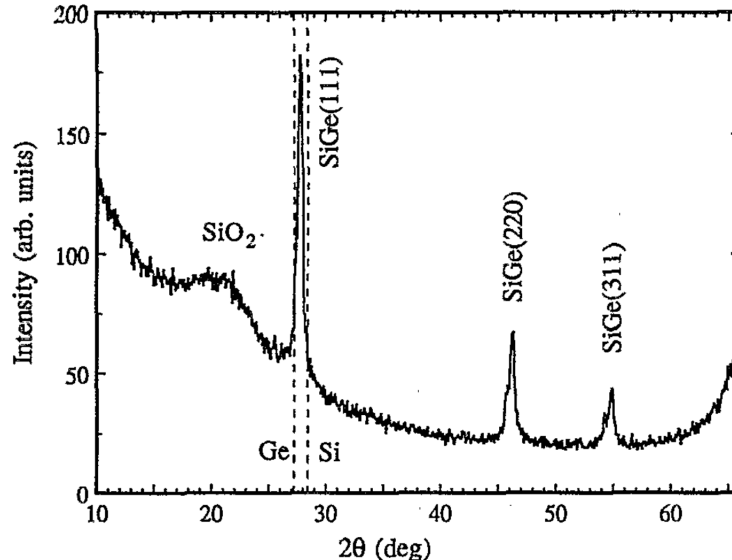


Figure 1.8: X-ray diffraction from SiGe precipitates in SiO<sub>2</sub>. Equal doses ( $3 \times 10^{17} \text{ cm}^{-2}$ ) of Si (215 keV) and Ge (500 keV) were implanted and the sample was annealed at 1100 °C for 1h. Reproduced from [40].

size of the precipitates. When the sample was annealed at 1100 °C, which is near the melting temperature of SiGe alloy, some particles were observed with dimensions greater than 100 nm

and some particles have coalesced (Figure 1.9a). On the other hand, when another sample was

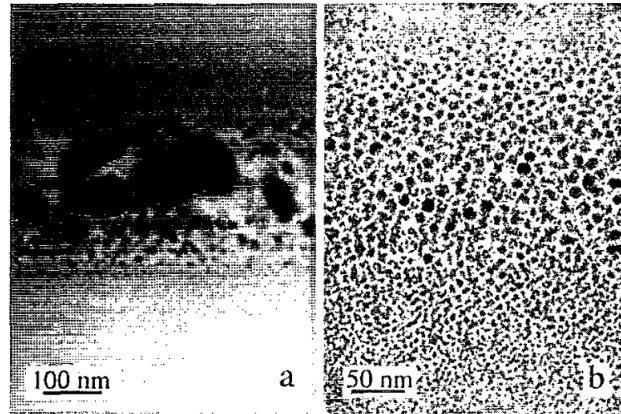


Figure 1.9: Transmission electron microscopy (TEM) of SiGe precipitates in SiO<sub>2</sub> after annealing at (a) 1100 °C and (b) 1000 °C for 1h. These samples have been implanted with Si (215 keV,  $3 \times 10^{17} \text{ cm}^{-2}$ ) and Ge (500 keV,  $3 \times 10^{17} \text{ cm}^{-2}$ ). Reproduced from [40].

annealed at 1000 °C (Figure 1.9b), the precipitates were spherical in shape and with a maximum size of 15 nm. Zhu et al.'s study [40] provides valuable insights into the energies and fluences required for fabricating SiGe QDs, as well as the size variations of these QDs under different annealing temperatures. However, the study does not cover the optical properties of the fabricated QDs.

Radio frequency (RF) sputtering was used to produce Si<sub>1-x</sub>Ge<sub>x</sub> QDs by Takeoka et al. in 2000 [41], with extensive optical characterization completed. In this case, silicon oxide films with a thickness of about 300 nm containing Si<sub>1-x</sub>Ge<sub>x</sub> nanocrystals were deposited using three targets simultaneously (SiO<sub>2</sub>, Si and Ge) followed by thermal annealing in N<sub>2</sub> gas at ambient pressure and 1100 °C. According to the authors, different compositions were produced with Ge content  $x$  ranging from 0 to 0.31. High-resolution transmission electron microscopy (HRTEM) showed the growth of spherical nanocrystals with 4.6 nm diameter in an amorphous SiO<sub>2</sub> matrix. Raman spectroscopy was also employed and its results are presented in Figure 1.10(a). According to the authors, the presence of three peaks for the samples containing Ge is in accordance with the spectrum of bulk Si<sub>1-x</sub>Ge<sub>x</sub> alloy crystals previously published in the literature [42]. Takeoka et al. also studied PL at room temperature using a 457.9 nm Ar-ion laser. Figure 1.10(b) shows a PL spectrum for each of the six different samples according to Ge content  $x$ . The average diameter (determined by HRTEM) of each sample is given on the left-hand side

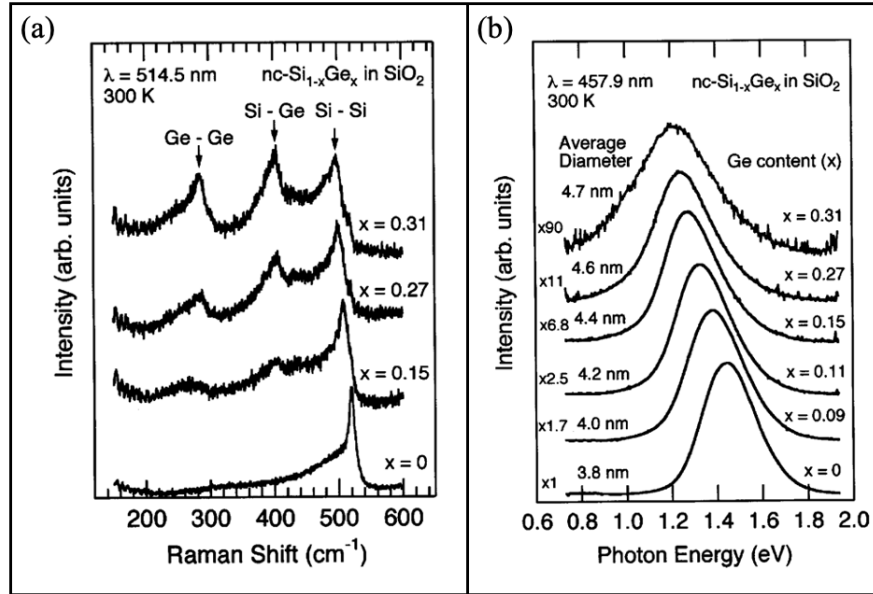


Figure 1.10: (a) Dependence of the Raman spectra of Si<sub>1-x</sub>Ge<sub>x</sub> nanocrystals on the Ge content. (b) PL spectra of Si<sub>1-x</sub>Ge<sub>x</sub> nanocrystals with various Ge contents. Adapted from [41].

of right-panel spectrum. It is clear there is a shift to lower energies as the Ge content increases. The author argues that is mainly caused by Si<sub>1-x</sub>Ge<sub>x</sub> alloy formation since the energy shift is about 240 meV. It could be due to the increasing size of Si nanocrystals from 3.8 to 4.7 nm, but this hypothesis entails an energy shift of only 50 meV [43], disagreeing with the observation. According to the authors, one of the reasons why the PL intensity decreases as the Ge content increases is the diameter increment for higher Ge concentrations since the size of nanocrystals is close to the Bohr radius. For instance, considering Si nanocrystals, it is known that PL intensity decreases one order of magnitude when nanocrystals increase diameter from 3 to 4 nm [44]. Another reason is the density of defects associated with Si<sub>1-x</sub>Ge<sub>x</sub> nanocrystals and the SiO<sub>2</sub> interface, which may increase with higher Ge content. The author has also studied the PL transients and found that the lifetime for all samples is on the order of a microsecond. Furthermore, it becomes shorter with increasing Ge concentration. For instance, the lifetime for  $x = 0$  is 10.1  $\mu\text{s}$  while for  $x = 0.31$  it is 1.5  $\mu\text{s}$ .

Takeoka et al.'s research [41] is complemented by the work conducted by Mogaddam et al. [45], with a particular focus on investigating the structural properties as a function of various annealing conditions. The typical thickness of deposited films was about 350 nm. The

deposition parameters were fixed to study the effect of annealing time on the local structure of the samples, which were thermally annealed at 1100 °C in N<sub>2</sub> gas and at ambient pressure, for 1, 3, or 5 h. The author also compared TEM imaging for samples annealed for 1 and 3 h, as shown in Figure 1.11. In this case, there were mixtures of nanocrystals of many sizes

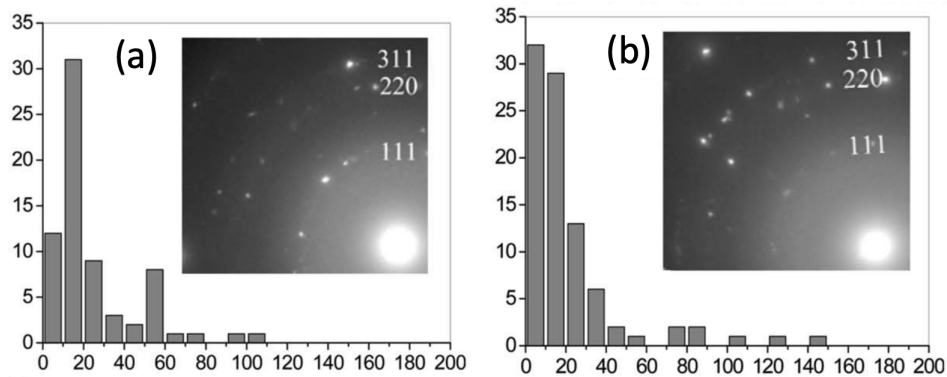


Figure 1.11: Size distribution, in nanometers, of the nanocrystals in the sample annealed for 1 h (a) and 3 h (b). Insets show the selected area diffraction patterns. Adapted from [45].

within the co-sputtered layer for both samples. This large variation can be understood by the Ostwald ripening process where large nanocrystals grow at the expenses of the smaller ones. However, the size distribution comparison of these two samples indicates that for the sample annealed for a long time of 3 h, the number of nanocrystals with sizes smaller than 10 nm is about three times that of the sample annealed for 1h. In addition, large nanocrystals with sizes of approximately 150 nm were formed accompanied by a significant decrease in the number of nanocrystals having a moderate size of 50 nm. Figure 1.11 also shows the histograms obtained from TEM for both samples.

A study deserving attention due to its integration of both structural and optical characterization of SiGe QDs formed by ion implantation in SiO<sub>2</sub> is the research published by Zhong et al. [46]. Zhong et al. formed SiGe QDs in SiO<sub>2</sub> films using consecutive implantation of Si<sup>+</sup> and Ge<sup>+</sup> ions with energies of 36 keV and 70keV, respectively. According to SRIM (Stopping and Range of Ions in Matter) simulations, the mean projected range (RP) of both ions was about 50 nm, without consideration of the sputtering effect. The fluences were chosen in order to maintain the total implanted dose constant at  $3 \times 10^{16}$  ions/cm<sup>2</sup>, followed by anneal at 900 °C for 1 h in N<sub>2</sub> ambient. Five samples (A1-A5) were made varying Si:Ge ra-

tios controlled by the implantation doses, from  $3 \times 10^{16}$  Si/cm<sup>2</sup> and 0 Ge for sample A1 to  $2.6 \times 10^{16}$  Si/cm<sup>2</sup> and  $0.4 \times 10^{16}$  Ge/cm<sup>2</sup> for sample A5. The authors used XRD, Raman spectroscopy, and HRTEM to characterize the microstructural properties of the samples. The XRD measurements showed the characteristic peak of SiGe(111) and, for higher germanium implanted doses (A3, A4, and A5) the SiGe(220) peak was also presented. According to the author, the QDs average size was about 3 to 4 nm, which was obtained using the Scherrer equation [47, 48],  $B(2\theta) = K\lambda/(L \cos \theta)$ , where  $B(2\theta)$  is the peak width,  $\lambda$  is the x-ray wavelength,  $L$  is the nanocrystal size, and  $K$  is a constant that is a function of the particle shape (generally taken as being about 1.0 for spherical particles). In addition, Figure 1.12 presents Raman spectra for the sample set, and three different peaks are shown in samples where germanium was implanted: Ge-Ge, Si-Ge, and Si-Si peak. The intensities of Si-Ge and Ge-Ge peaks were en-

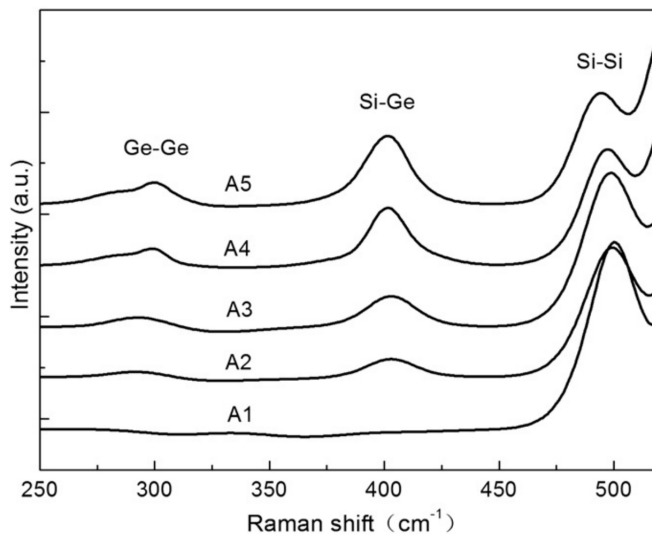


Figure 1.12: Raman spectroscopy measurements of the samples made by Zhong et al. [46]. Adapted from [46].

hanced with the increase of Ge dose. Furthermore, the author also identified QDs in the silicon oxide matrix using HRTEM and their diameters were measured to be 3 to 4 nm. The paper also presents the results of PL measurements and time-resolved photoluminescence (TRPL). Both were done at room temperature and using a wavelength of 325 nm for excitation. Figure 1.13 shows them. In Figure 1.13(a), the spectra show a strong emission in the red region. With the increase of Ge dose, the PL peak shifts from 653 nm (sample A1) to around 700 nm (sample A5), and PL reaching maximum intensity for sample A3. According to the authors, if the PL



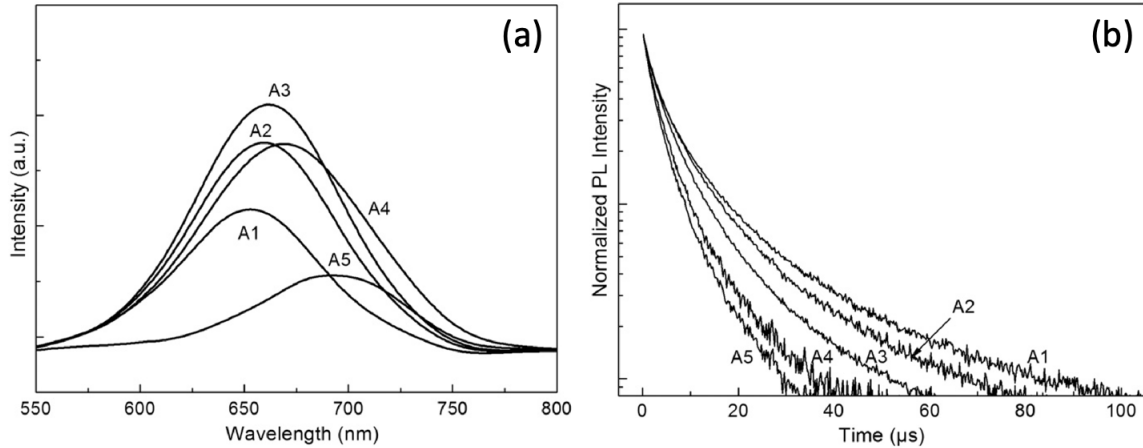


Figure 1.13: (a) Room temperature PL spectra. (b) Normalized time-resolved PL decays at 675 nm. Adapted from [46].

peaks originate from a localized state such as a defect center at the QS/matrix interface, the wavelength of PL peaks should be independent of the Ge doping dose. From the experimental result, the quantum confinement of an electron–hole pair in the SiGe QDs is considered as a possible mechanism for the visible PL emission. Consequently, the redshift of PL indicates an energy gap narrowing of SiGe QDs as a function of Ge concentration. Figure 1.13(b) shows the normalized TRPL transients for all samples. The lifetime decreased from  $50.2\ \mu\text{s}$  to  $23.1\ \mu\text{s}$  as the Ge implanted dose increased from 0 to  $4 \times 10^{15}\ \text{ions}/\text{cm}^2$ .

Besides the growth of SiGe QDs into silicon oxide, Mirzaei et al. [49] have used a  $2\ \mu\text{m}$  silicon nitride ( $\text{Si}_3\text{N}_4$ ) layer as a matrix. In this case, only  $\text{Ge}^+$  ions were implanted at  $400\ ^\circ\text{C}$ , followed by anneal at  $700\ ^\circ\text{C}$  or  $900\ ^\circ\text{C}$ , for 1 h, in dry  $\text{N}_2$ . The implanted doses resulted in an atomic percentage of 9 and 12% in relation to the silicon nitride matrix, respectively. In order to evaluate the formation of QDs, the author used transmission electron microscopy. Figure 1.14 presents the size distribution of both samples (9 at.% Ge, annealed at  $700\ ^\circ\text{C}$  and 12 at.% Ge, annealed at  $900\ ^\circ\text{C}$ ). Complementary techniques such as synchrotron-based methods of X-ray-absorption near-edge structure and extended X-ray-absorption fine-structure spectroscopy have also been utilized to characterize the size and structure of the embedded nanostructures. The formation of SiGe QDs was evidenced using these techniques, and the small QD size with relatively high Ge concentrations at high annealing temperatures is the direct result of a low Ge mobility in silicon nitride matrix. This result highlights the role of the matrix in the embedded

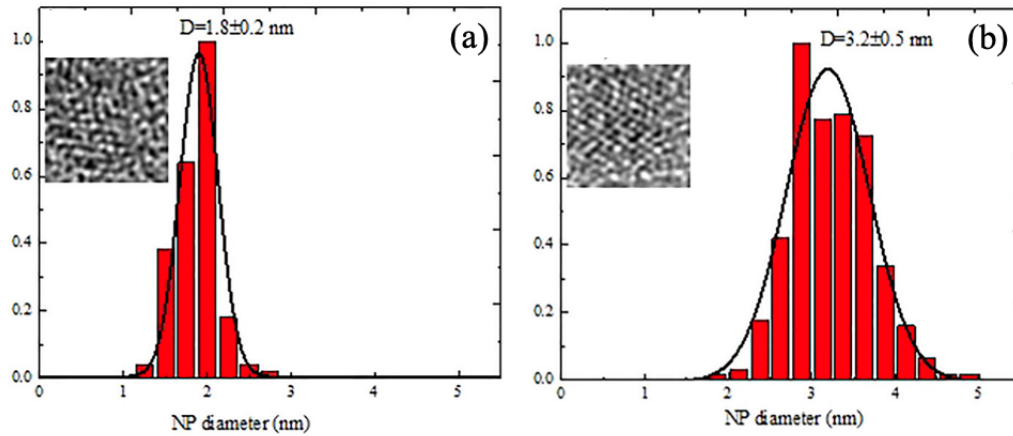


Figure 1.14: TEM images and histograms of quantum dot diameters for (a) 9 at.% annealed at 700 °C and (b) 12 at.% annealed at 900 °C. Adapted from [49].

nanostructure properties.

Table 1.1 summarizes the papers that were discussed in this literature review. As mentioned

	Zhu et al. (1995) [40]	Takeoka et al. (2000) [41]	Mogaddam et al. (2008) [45]	Zhong et al. (2012) [46]	Mirzaei et al. (2017) [49]
Technique used to form the nanostructures	Ion implant	Sputtering	Sputtering	Ion implant	Ion implant
Matrix	SiO <sub>2</sub>	SiO <sub>2</sub>	SiO <sub>2</sub>	SiO <sub>2</sub>	Si <sub>3</sub> N <sub>4</sub>
Anneal temperature(s) (°C)	1000 and 1100	1100	1100	900	700 and 900
Anneal time	1h	Not specified	1, 3, and 5h	1h	1h
Anneal environment	Ar + 5% H <sub>2</sub>	N <sub>2</sub>	N <sub>2</sub>	N <sub>2</sub>	N <sub>2</sub>
Different compositions	No	Yes	No	Yes	Yes
Optical measurements	No	PL and TRPL	No	PL and TRPL	No
Structural measurements	XRD and TEM	Raman and TEM	XRD, Raman, XPS, and TEM	XRD, Raman, and TEM	TEM, XANES, and EXAFS

Table 1.1: Summary of papers reviewed in this section.

before, the general literature lacks studies about SiGe nanostructures produced by ion implantation in silicon dioxide. As a result, we could report just two among five overall presented in this review chronologically. We also added two studies about SiGe QDs produced by sputtering deposition in order to compare and have additional information about the optical and structural properties. Now, it is important to compare these results to each other. For instance, taking

the PL emission curve from Zhong et al. [46] and comparing it to the emission results obtained by Takeoka et al. [41], we expect to have similar wavelength peaks for samples without Ge. This is reasonable since the reported QS average size is about the same (4 nm) for both. From [41], the peak energy related to the sample with no Ge content is about 1.45 eV, which is equivalent to  $\lambda = 855$  nm. However, [46] reported the peak wavelength being  $\lambda = 660$  nm for the sample without germanium. Another result presented in the work of Zhong et al. [46] is the PL intensity increasing with Ge implanted doses for samples A2 and A3. This observation contradicts the previous publication of Takeoka et al. [41], where the emission decreased by almost a factor of two for less than 10% of germanium increment.

Therefore, there are many unresolved questions in this field of SiGe Qs in SiO<sub>2</sub> produced by ion implantation, considering that the literature does not explain some inconsistencies between SiGe Qs produced by ion implantation and other techniques, and no study so far has been performed systematically to understand the mechanisms of light emission in SiGe Qs, in particular distinguishing light emission from the semiconductor QDs, defects in the matrix or Si QD/matrix interface, or just the matrix itself.

## 1.4 Scope of the Thesis

Semiconductors and their associated quantum structures are particularly special materials. The controlled or involuntary introduction of defects, whether they are impurities in their crystal structure, as in the case of dopants, or mere structural flaws, is capable of promoting drastic changes in the electrical and optical properties of these systems. Therefore, the study and characterization of such defects are crucial for the development and improvement of semiconductor devices. One of the main characteristics of this industrial sector is its close relationship with cutting-edge research, especially in areas such as materials engineering, condensed-matter physics, and surface science. Surface science techniques play a key role in advancing epitaxial growth, a critical process in material science and semiconductor technology [50, 51]. Among these techniques, low energy electron diffraction (LEED) stands out as a powerful tool for characterizing crystal surfaces. LEED provides valuable insights into surface structures, allowing researchers to precisely monitor the arrangement of atoms during their formation [52]. This

capability is vital in optimizing fabrication methods of QDs and materials in general, and ensuring the desired crystal quality, ultimately influencing the electronic and optical properties of materials. The fine-tuning of epitaxial growth made possible by surface science techniques like LEED is fundamental to the development of high-performance devices and the continual progression of semiconductor technologies.

In the first part of the thesis, I used ion beam analysis and low energy electron diffraction to explore the intrinsic relationship between defect concentration and fundamental properties of materials, more specifically, the Debye temperature. To achieve this, test samples with different defect concentrations measured by established methods, such as ion channeling and positron annihilation spectroscopy (PAS), were employed, and the Debye temperature measured by LEED was associated to the concentration of defects. In Chapter 3, I presented findings that highlight the correlation between Debye temperature and the crystal quality of the material. This research contributes to the field by offering LEED as an alternative technique for addressing defects in the surface and near-surface layers.

The relevance of defects extends beyond their influence on fundamental properties like the Debye temperature. They alter the optical properties significantly. In the second part of this thesis, I studied the optical and structural properties of SiGe QDs made either by Si and Ge implantation or Ge implantation only in an insulating matrix of silicon oxide. In Chapter 4, I have investigated SiGe QDs produced through co-implantation, focusing on determining the optimal conditions, including Si and Ge implanted doses and annealing temperatures, to attain quantum confinement in these SiGe QDs. In Chapter 5, I combined two different experimental techniques (PECVD and Ge ion implantation) to produce SiGe QDs and studied their optical and structural properties. Furthermore, I have achieved a comprehensive understanding of the impact of composition, crystalline structure, and stress in SiGe quantum structures on their optical properties, particularly luminescence.

# References

- [1] T. Smijs and S. Pavel, *Nanotechnology, Science and Applications* 4, 95 (2011).
- [2] K. Schnabl, L. Wentlent, K. Mootoo, S. Khasawneh, A. A. Zinn, J. Beddow, E. Hauptfleisch, D. Blass, and P. Borgesen, *Journal of Electronic Materials* 43, 4515 (2014).
- [3] S. Chaturvedi, P. N. Dave, and N. K. Shah, *Journal of Saudi Chemical Society* 16, 307 (2012).
- [4] Z. Abdullaeva, *Nanomaterials in Daily Life* (Springer International Publishing, 2017).
- [5] Simon M. Sze, *Physics of Semiconductor Devices* (Wiley-Interscience, 2006).
- [6] Ben Streetman, *Solid State Electronic Devices* (Prentice Hall, 2005).
- [7] *The International Technology Roadmap for Semiconductors (ITRS) 2009*.  
<http://www.itrs2.net/itrs-reports.html>. Accessed: January 3rd, 2024.
- [8] G.E. Moore, *IEEE Solid-State Circuits Society Newsletter* 11, 33 (2006).
- [9] G.E. Moore, *IEEE Solid-State Circuits Society Newsletter* 11, 36 (2006).
- [10] K. König and A. Ostendorf, *Optically Induced Nanostructures: Biomedical and Technical Applications* (De Gruyter, 2015).
- [11] D. Miller, *Proceedings of the IEEE* 97, 1166 (2009).
- [12] V. S. Chakravarthi, *A Practical Approach to VLSI System on Chip (SoC) Design* (Springer International Publishing, 2020).
- [13] A. Halimaoui, C. Oules, G. Bomchil, A. Bsiesy, F. Gaspard, R. Herino, M. Ligeon, and F. Muller, *Applied Physics Letters* 59, 304 (1991).
- [14] A. G. Cullis and L. T. Canham, *Nature* 353, 335 (1991).

- [15] L. Pavesi, L. Dal Negro, C. Mazzoleni, G. Franzò, and F. Priolo, *Nature* 408, 440 (2000).
- [16] M. A. Reed, R. T. Bate, K. Bradshaw, W. M. Duncan, W. R. Frensley, J. W. Lee, and H. D. Shih, *Spatial Quantization in GaAs–AlGaAs Multiple Quantum Dots*, *Journal of Vacuum Science and Technology B: Microelectronics Processing and Phenomena* 4, 358 (1986).
- [17] F. A. Zwanenburg, A. S. Dzurak, A. Morello, M. Y. Simmons, L. C. L. Hollenberg, G. Klimeck, S. Rogge, S. N. Coppersmith, and M. A. Eriksson, *Reviews of Modern Physics* 85, 961 (2013).
- [18] L. M. K. Vandersypen and M. A. Eriksson, *Physics Today* 72, 38 (2019).
- [19] *International Roadmap for Devices and Systems* (IEEE, 2018)
- [20] *Press Release: Gartner Forecasts Worldwide Semiconductor Revenue to Grow 17% in 2024*. <https://www.gartner.com/en/newsroom/press-releases/2023-12-04-gartner-forecasts-worldwide-semiconductor-revenue-to-grow-17-percent-in-2024>. Accessed: December 20th, 2023
- [21] <https://www.precedenceresearch.com/compound-semiconductor-market>. Accessed: December 20th, 2023
- [22] *Printed, Organic and Flexible Electronics 2020-2030: Forecasts, Technologies, Markets* <https://www.idtechex.com/de/research-report/printed-organic-and-flexible-electronics-2020-2030-forecasts-technologies-markets/687>. Accessed: February 11th, 2020.
- [23] A.D. Pogrebnjak (Ed.), *Ion Implantation: Synthesis, Applications and Technology* (Nova Science Publishers, Hauppauge, NY, USA, 2019).
- [24] R. Hellborg, H. Whitlow, Y. Zhang (Editors), *Ion Beams in Nanoscience and Technology* (Springer, New York, NY, USA, 2010).
- [25] C. Kittel, *Introduction to solid state physics*, 8th ed., J. Wiley, New York, 2005.
- [26] Y. Shiraki and N. Usami (Editors), *Silicon–germanium (SiGe) nanostructures: production, properties and applications in electronics* (Woodhead Publishing, Cambridge, UK)
- [27] E. G. Barbagiovanni, D. J. Lockwood, P. J. Simpson, and L. V. Goncharova, *Applied Physics Reviews* 1, 11302 (2014).

- [28] C. R. Mokry, P. J. Simpson, and A. P. Knights, *Journal of Applied Physics* 105, (2009).
- [29] E. G. Barbagiovanni, L. V. Goncharova, and P. J. Simpson, *Physical Review B* 83, (2011).
- [30] E. G. Barbagiovanni, D. J. Lockwood, P. J. Simpson, and L. V. Goncharova, *Journal of Applied Physics* 111, 34307 (2012).
- [31] L. V. Goncharova, P. H. Nguyen, V. L. Karner, R. D'Ortenzio, S. Chaudhary, C. R. Mokry, and P. J. Simpson, *Journal of Applied Physics* 118, 224302 (2015).
- [32] C. C. Cadogan, L. V. Goncharova, P. J. Simpson, P. H. Nguyen, Z. Q. Wang, and T.-K. Sham, *Journal of Vacuum Science & Technology B* 34, 61202 (2016).
- [33] A. Zunger, *Phys. Status. Solidus. B* 224, 727 (2001).
- [34] D. B. T. Thoai, Y. Z. Hu, and S. W. Koch, *Phys. Rev. B.* 42, 11261 (1990).
- [35] N. Tit, Z. H. Yamani, J. Graham, and A. Ayes, *Mater. Chem. Phys.* 24, 927 (2010)
- [36] S. Glutsch, *Excitons in low-dimensional semiconductors* (Springer, 2004).
- [37] Y. M. Haddara, P. Ashburn, and D. M. Bagnall, *Springer Handbook of Electronic and Photonic Materials* (Springer International Publishing, 2017).
- [38] F. Erogbogbo, T. Liu, N. Ramadurai, P. Tuccarione, L. Lai, M. T. Swihart, and P. N. Prasad, *ACS Nano* 5, 7950 (2011).
- [39] Z. Yang, Y. Shi, J. Liu, B. Yan, R. Zhang, Y. Zheng, and K. Wang, *Materials Letters* 58, 3765 (2004).
- [40] J. G. Zhu, C. W. White, J. D. Budai, S. P. Withrow, and Y. Chen, *Journal of Applied Physics* 78, 4386 (1995).
- [41] S. Takeoka, K. Toshikiyo, M. Fujii, S. Hayashi, and K. Yamamoto, *Physical Review B* 61, 15988 (2000).
- [42] M. I. Alonso and K. Winer, *Physical Review B* 39, 10056 (1989).
- [43] H. Takagi, H. Ogawa, Y. Yamazaki, A. Ishizaki, and T. Nakagiri, *Applied Physics Letters* 56, 2379 (1990).
- [44] Y. Kanzawa, T. Kageyama, S. Takeoka, M. Fujii, S. Hayashi, and K. Yamamoto, *Solid State Communications* 102, 533 (1997).

- [45] N. A. P. Mogaddam, A. S. Alagoz, S. Yerci, R. Turan, S. Foss, and T. G. Finstad, *Journal of Applied Physics* 104, 124309 (2008).
- [46] K. Zhong, M. Lai, Y. Chen, and B. Gu, *Physica B: Condensed Matter* 407, 3660 (2012).
- [47] P. Scherrer, *Göttinger Nachrichten Math. Phys.* 2, (1918)
- [48] A. L. Patterson, The Scherrer Formula for X-Ray Particle Size Determination, *Phys. Rev.* 56, 978 (1939).
- [49] S. Mirzaei, F. Kremer, R. Feng, C. J. Glover, and D. J. Sprouster, *Journal of Applied Physics* 121, 105702 (2017).
- [50] Lyudmila V. Goncharova, *Basic Surfaces and their Analysis* (Morgan & Claypool Publishers, 2018).
- [51] Kurt W. Kolasinski, *Surface Science: Foundations of Catalysis and Nanoscience* (Wiley, 2012).
- [52] M. A. Van Hove, W. H. Weinberg, and C.-M. Chan, *Low-Energy Electron Diffraction: Experiment, Theory and Surface Structure Determination* (Springer Berlin Heidelberg, 1986).



# Chapter 2

## Experimental methods

### 2.1 Fabrication methods

In this thesis, samples were either commercially acquired or fabricated using the facilities at Western University. In the last case, samples were made by ion implantation and plasma-enhanced chemical vapour deposition (PECVD) techniques. The following subsections describe these sample preparation methods.

#### 2.1.1 Ion implantation

Ion implantation is a material processing technique in which ions of a specific chemical element can be energetically introduced into a matrix. Ion implantation has been used in semiconductor industries for many years, and in the last two decades, implantation process has been applied to a diverse range of other application (see recent reviews [1, 2]). Atoms are ionized, accelerated, separated by the mass-to-charge ratios, and directed at the sample. It is a non-equilibrium thermodynamic technique, enabling the introduction of elements into substrates at concentrations from a fraction of atomic percent to much higher values, well above their solubility limits.

Ion implantation has independent control of the dose and energy, allowing the formation of various implantation profiles. The mass separation allows for the generation of monoenergetic and highly pure ion beams, preventing sample contamination. This capability also enables the same accelerator to be used for the implantation of different ions.

One must keep in mind that, due to collisions experienced by the ions and the statistical

nature of the process, not all ions will end their trajectory at the same point (called projected range  $R_p$ ). Therefore, there is a variation of this parameter, referred to as straggling ( $\Delta R_p$ ). A typical depth profile in an amorphous substrate from monoenergetic ions at moderate ion doses is approximately Gaussian in shape and can be characterized by  $R_p$  and  $\Delta R_p$  about this mean value, as shown in Figure 2.1(a). Monte Carlo simulation, such as Stopping and Range of Ions

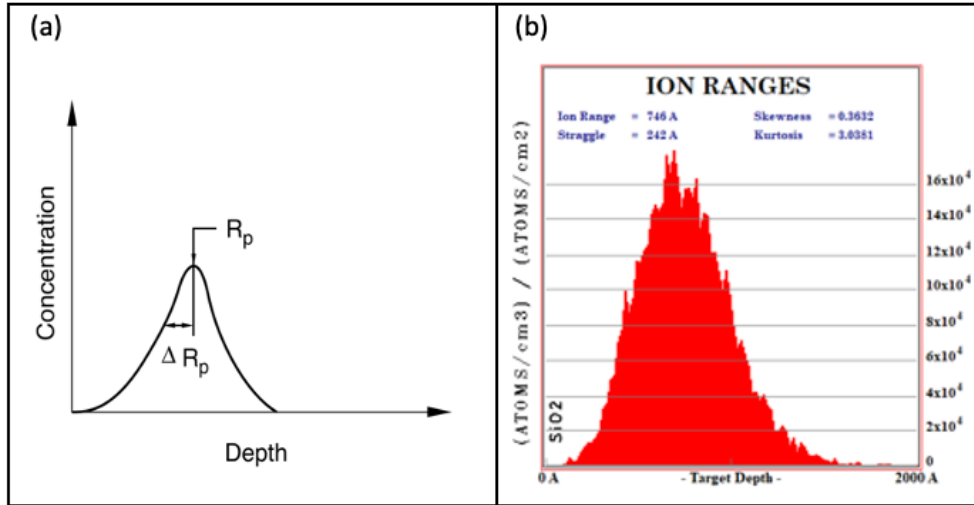


Figure 2.1: (a) Approximation of the depth distribution of implanted atoms in an amorphous target. Adapted from [3]. (b) Simulated Ge ions depth distribution when implanted into a SiO<sub>2</sub> target. Simulation performed with SRIM [4].

in Matter (SRIM) [4] or TRIDYN [5], is widely used to estimate the depth profile. During the operation of the SRIM software, the high energy incident particle undergoes numerous interactions with substrate atoms. Each interaction causes energy loss, particle deflection, and potentially the displacement of the impacted atom, thus generating a collision cascade. This process of particle-atom interaction is stochastic, and the SRIM software iteratively models it using a Monte Carlo process. SRIM provides two methods for predicting implantation profile and induced atomic damage: the full cascade method and the quick method. Figure 2.1(b) shows the results of a simulation of 100 keV Ge ions implanted into SiO<sub>2</sub> calculated by the SRIM [4] (version 2008), using full cascade method.

The equipment used in this work to perform the implants is part of the Tandatron Accelerator Laboratory at Western University [6]. Figure 2.2 illustrates the accelerator and its

capabilities. This accelerator has two independent ion sources: one for gases (duoplasmatron

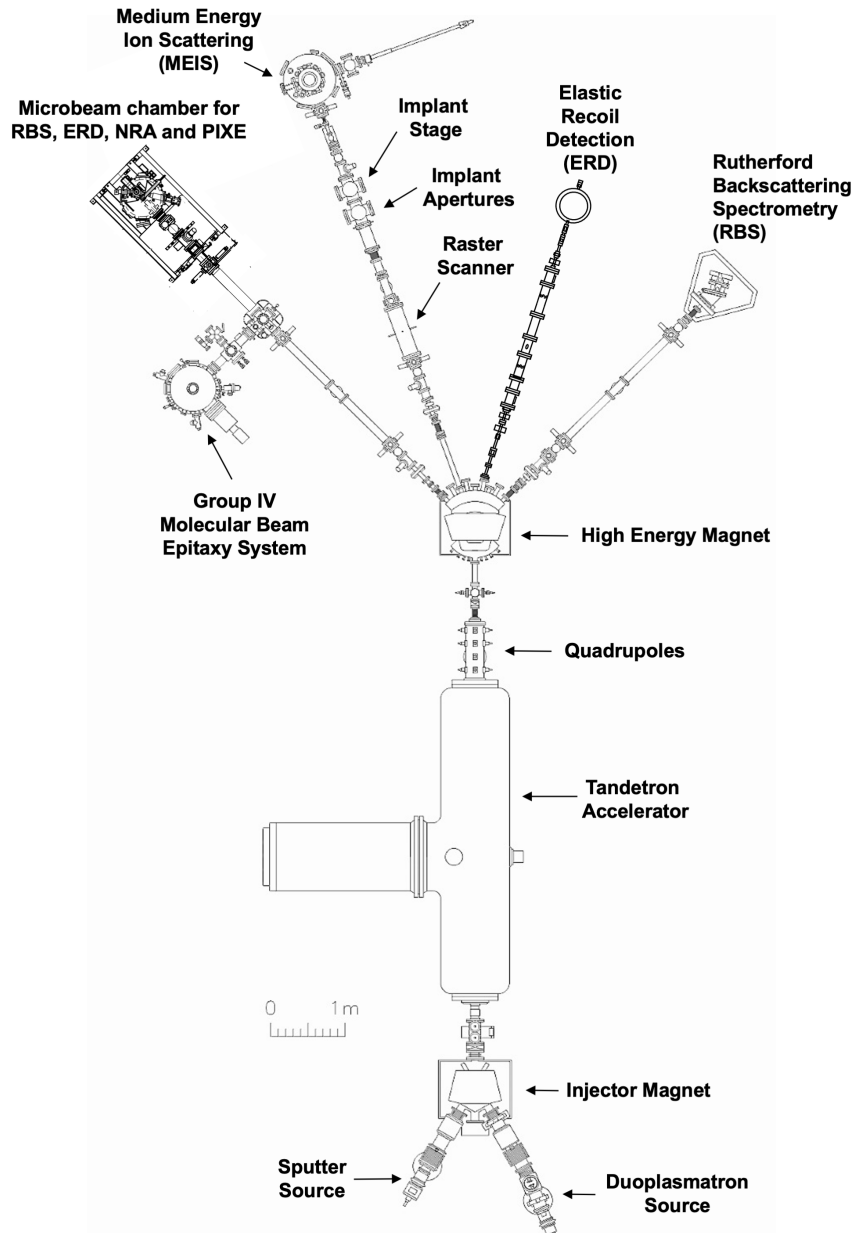


Figure 2.2: Tandatron accelerator schematic at Western Univeristy.

source) and another for solids (sputter source). The gas source operates based on gas ionization, while in the sputtering source the ions are generated by bombarding the sputter targets of the intended material with Cs ions. Si and Ge ion beams were generated using a sputtering source, while He ions used for Rutherford backscattering analysis were generated using a duoplasmatron source. The tandem accelerator accelerates the ions in two stages. This tandem

effect is very effective for generating high energetic ion beams with energies up to a few MeV. The ions generated have a negative charge before reaching the injector magnet and are thus accelerated by a positive potential  $V$ . In the center of the accelerator tube, the ions undergo a charge exchange in the stripper gas, becoming positively charged and then repelled by a potential  $nqV$ , where  $n$  is the degree of ionization of the ion. Then, the beam containing ions with all possible charge states is accelerated up to the high energy magnet, where the mass-to-charge ratio is selected and the beam directed to the implant stage, where the target will be implanted. The separation among different ions is accomplished through magnetic analyzers in the high energy magnet. It is known that for a particle with mass  $m$ , charge  $q$ , travelling at constant speed  $v$ , in a magnetic field with the magnitude perpendicular to the particle trajectory being  $B$ , its curvature radius  $r$  is  $mv/(qB)$ . Considering that the particle was accelerated by a difference of electric potential  $V$ , it is straight forward to show that:

$$B = \frac{1}{r} \sqrt{\frac{2mV}{q}}. \quad (2.1)$$

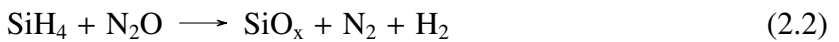
By knowing the mass ( $m$ ) and charge ( $q$ ) of the ions to be implanted, the curvature radius of the analyzer ( $r$ ), and the voltage used to accelerate the ions ( $V$ ), the magnetic field ( $B$ ) is determined. This field must be applied in such a way that only ions with the exact mass-to-charge ratio can overcome the curve and pass through the slit placed at the exit of the analyzer.

My samples were made using the sputter source to implant Si and Ge. The implant energies ranged from 40 keV to 100 keV. Silicon and germanium beams were rastered to achieve uniform implantation over the desired areas with beam currents kept between 400 nA to  $1.7 \mu\text{A}$ . Doses ranged from  $1.30 \times 10^{15}$  (low dose Ge implants) to about  $1.00 \times 10^{17}$  ions/cm<sup>2</sup> (high dose Si implants). More details about that will be provided in chapters 4 and 5.

### 2.1.2 Plasma-enhanced chemical vapour deposition (PECVD)

A chemical vapour deposition process (CVD) can be defined as one in which the formation of solid films on the surface of a substrate occurs through the chemical reaction of reactive gases in the vapour phase containing the necessary compounds for the deposition of the desired material film [7]. Plasma-enhanced chemical vapour deposition (PECVD) reactors have been developed

in response to the need for thin film deposition at low temperatures. PECVD systems, operating at low pressures, have a key feature: a supplementary energy source (heated sample stage) to promote and sustain chemical reactions among gaseous species. In addition to thermal energy, a radio frequency electric field is used, inducing an electrical discharge that transfers energy to the molecules of reactive gases and diluents, generating free radicals that facilitate film deposition. Consequently, the substrate temperature during the PECVD process can be significantly reduced. In this thesis, I used silane ( $\text{SiH}_4$ ) and nitrous oxide ( $\text{N}_2\text{O}$ ) as precursors to deposit Si-rich  $\text{SiO}_x$  according to the chemical reaction (2.2):



It is important to note that the stated chemical reaction is the ideal scenario. In general,  $\text{SiO}_x$  films have Si-O-N bonding fragments corresponding to 10 at.% of nitrogen [8]. Figure 2.3 shows a schematic of a typical PECVD reactor, exemplifying the basic components of this system. Shown are the gas inlet, the electrode where RF voltage is applied to induce the plasma,

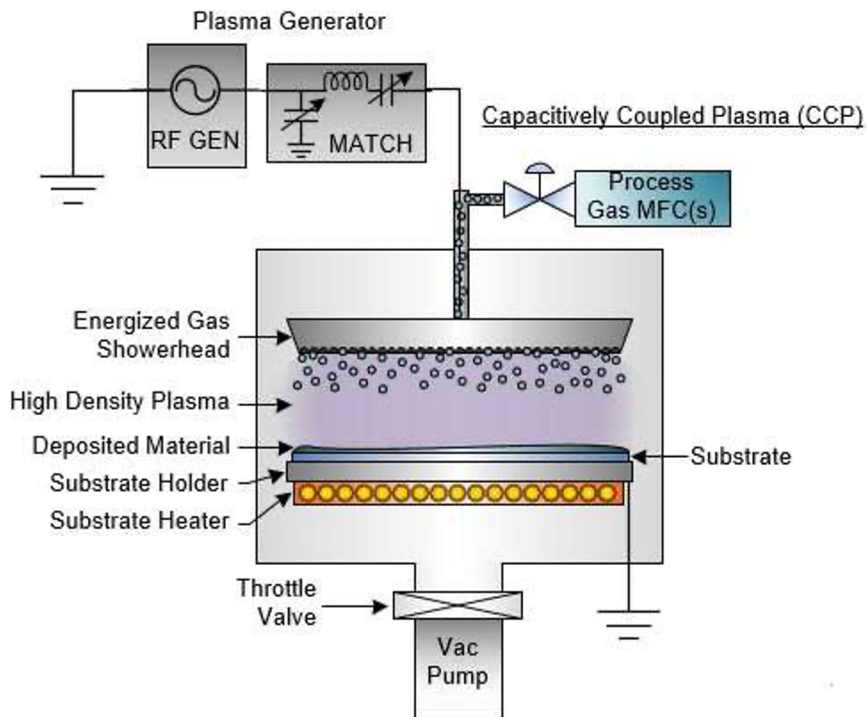


Figure 2.3: PECVD reactor schematic illustrating its basic components. Copied from [9].

and the heater that provides energy promoting the chemical reaction. My samples made by

PECVD were fabricated at Western Nanofabrication Facility using the PECVD system, model STS 310PC [10].

## 2.2 Characterization methods

### 2.2.1 Rutherford backscattering spectrometry (RBS)

The RBS technique [3, 11, 12] is based on the detection of incident particles that collide with a sample and are scattered at angles greater than  $90^\circ$ , usually  $\approx 170^\circ$ . Typically, a monoenergetic beam of alpha particles or protons is used. When the beam reaches the sample, the beam particles will collide with the atoms of the sample and, depending on the parameters of the collision, the particles will be scattered at various angles and with different energy values. Some of these particles will reach the detector, which will then measure the energy of each particle and in this way a spectrum containing the number of particles for each energy value will be assembled. The final energy of the scattered particle depends on its mass, the mass of the target atom, the particle's energy before the collision and the scattering angle. As the detector is in a fixed position, only particles that are scattered in the direction of the detector at a known angle will be detected. Therefore, the difference between the projectile energy before and after the collision will be related only to the mass of the target's atoms. Figure

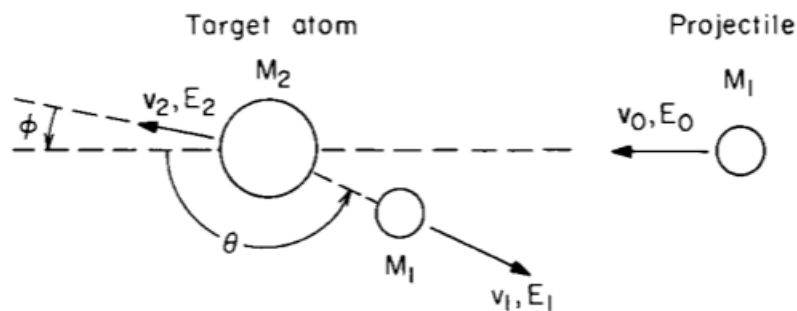


Figure 2.4: Schematic representation of an elastic collision between a projectile of mass  $M_1$ , velocity  $v_0$ , and energy  $E_0$  and a target of mass  $M_2$  which is initially at rest. After the collision, the projectile and the target mass have velocities and energies  $v_1$ ,  $E_1$  and  $v_2$ ,  $E_2$ , respectively. The angles  $\theta$  and  $\phi$  are positive as shown. Reproduced from [11].

2.4 represents a diagram of a collision with scattering and recoil angles shown. Considering

there are no nuclear reactions, the collision is elastic, and the energy and linear momentum are conserved, we obtain the kinematic factor  $K$ , which is the ratio between the energy of the incident particle after the collision ( $E_1$ ) and the energy before the collision ( $E_0$ ).  $K$  is given by [11]:

$$K = \frac{E_1}{E_0} = \left[ \frac{(M_2^2 - M_1^2 \sin^2 \theta)^{1/2} + M_1 \cos \theta}{M_1 + M_2} \right]^2. \quad (2.3)$$

As seen in the equation above, each combination of projectile, target and scattering angle will have its characteristic kinematic factor. Knowing the mass and energy of the incident beam particles and measuring the energy of the scattered particles, it is possible to calculate the kinematic factor. Then, knowing the angle of detection, it is possible to calculate the mass of the target atom which the particle collided with. Therefore, atoms with different masses will appear at different positions in the spectrum.

In order to understand an RBS spectrum, it is also necessary to know the chances that collisions will occur and, additionally, the chances that after the collision the particles scatter at the angle, where the detector is. For this reason, there is the concept called differential scattering cross section for nuclear collisions,  $d\sigma/d\Omega$ , where  $\Omega$  is the solid angle of the detector. The differential scattering cross section has the dimension of an area and can be interpreted as the probability that the scattering event will produce a signal at the detector.  $d\sigma/d\Omega$  can be calculated using the Coulomb repulsion potential in the interaction between the ion beam nuclei and the nuclei of the sample atoms. The final expression is [11]:

$$\frac{d\sigma}{d\Omega} = \left( \frac{Z_1 Z_2 q^2}{16\pi\epsilon_0 E} \right)^2 \frac{4}{\sin^4 \theta} \frac{\{[1 - ((M_1/M_2) \sin \theta)^2]^{1/2} + \cos \theta\}^2}{[1 - ((M_1/M_2) \sin \theta)^2]^{1/2}}, \quad (2.4)$$

where  $E$  is the energy of the projectile immediately before scattering,  $Z_1$ ,  $Z_2$  are atomic numbers of the incident particle and target nuclei. From this expression we can obtain important information:

- $d\sigma/d\Omega$  is proportional to  $Z_1^2$ : the backscattering yield of a measurement using a He beam as the incident particle is 4× higher than one using a H beam.
- $d\sigma/d\Omega$  is proportional to  $Z_2^2$ : heavier target atoms scatter more than light ones. In other

words, the technique is more sensitive to heavy elements.

- $d\sigma/d\Omega$  is inversely proportional to the incident beam energy squared. Then, the number of backscattered particles increases as the incident beam energy decreases.
- $d\sigma/d\Omega$  is symmetric in relation to the incident beam direction, and it is only a function of the scattering angle  $\theta$ .
- When  $M_1 \ll M_2$ ,  $d\sigma/d\Omega$  is inversely proportional to the fourth power of  $\sin \theta$ , making the backscattering yield to increase quickly as  $\theta$  gets closer to  $180^\circ$ .

It can be demonstrated that, for small  $\Omega$ , the total number of detected particles,  $A$ , is [11]:

$$A = \frac{d\sigma}{d\Omega} \times \Omega \times Q \times N \times t, \quad (2.5)$$

where  $Q$  is the total number of ions incident on the sample,  $N$  is the atomic density of the sample layer where the incident ions are scattered, and  $t$  is the thickness of this layer. Thus,  $Nt$  is the areal density of target atoms of the sample (atoms/cm<sup>2</sup>). Therefore, knowing  $d\sigma/d\Omega$  and  $\Omega$  and counting the total number of incident particles ( $Q$ ) and detected ones ( $A$ ), it is possible to determine the density per unit area of the target atoms for each element.

When penetrating into the target, the incident particle loses some of its energy due to electronic interactions before it collides. Another part of the energy is lost in the collision and, finally, another part is lost in its exit path towards the sample surface. Consequently, a particle that collided with an atom on the target surface will be detected with greater energy than an identical particle that collided with an identical deeper target atom. Then, it is possible to determine the depth of the target atom by measuring the energy of the detected particle. The total energy lost by the beam  $\Delta E = (dE/dx)\Delta x$  (for approximations where  $dE/dx$  can be considered constant as a function of energy) also increases linearly with  $\Delta x$ . Then, it is determined that  $\Delta E$  is proportional to  $N\Delta x$  and the proportionality constant is defined by

$$\varepsilon \equiv \frac{1}{N} \frac{dE}{dx}, \quad (2.6)$$

which is called the *stopping cross section*. The stopping cross section is a measurement of the



ability that the chemical species in the target has to slow down the incident ions.

Figure 2.5 shows an RBS spectrum for a film of gold (Au) on top of a film of aluminum on carbon (C). The lighter atom gives a signal at low energies with a low yield. The heavier atom produces a signal at high energies with a high yield. The difference in energies is due to the different kinematic factors  $K$  and the depth of each element. The differences in yield height between Al and Au are due to the different cross sections. Using the stopping cross section values, it is possible to convert the energy values of the horizontal axis of the spectrum to depth value and it allows us to extract the concentration profile of the two elements that compose the film. It is important to note that RBS spectra have slopes at the edges due to various

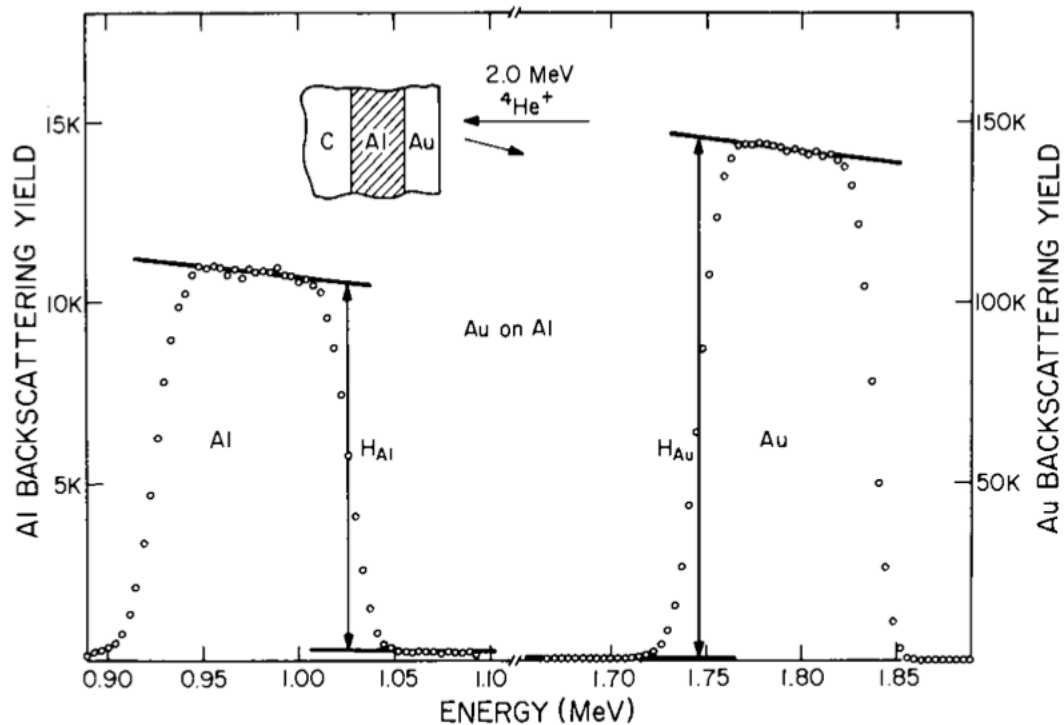


Figure 2.5: Example of a typical RBS spectrum pointing out the edge slopes and the higher number of count as the film depth increases (lower peak energies) [11].

factors, such as fluctuations in beam energy, fluctuations in energy loss, and the resolution of the detection system. In addition to fluctuations, as the beam penetrates the sample and loses energy, the scattering cross section increases (as it is proportional to  $E^{-2}$ ) and for this reason, the number of counts increases for deeper layers of the sample.

Combining all the concepts presented so far, it is possible to extract, from the measured

spectra, information about the sample elements, as well as the concentration profile of each one of them. In this project, this will be very useful for determining the concentration of the  $\text{Si}_{1-x}\text{Ge}_x$  nanoparticles and their distribution profile along the sample depth. Elemental depth profiles obtained using RBS will be compared with computer simulations, allowing us to quantify quantum dots stoichiometry after different growth processes in these systems.

### 2.2.2 Channelling

The concepts presented so far refer to amorphous targets. When the target is crystalline, an important effect can occur: channeling. Channeling occurs when the ions of the beam are conducted through channels formed by lines or planes of atoms, as shown in Figure 2.6, and, as a result, a shadow cone is formed. This happens because the surface atoms scatter most of the beam ions at small angles and direct them into the interior of the crystalline channels, so that the ions do not encounter the atoms of the lower layers of the sample. The collisions occurring

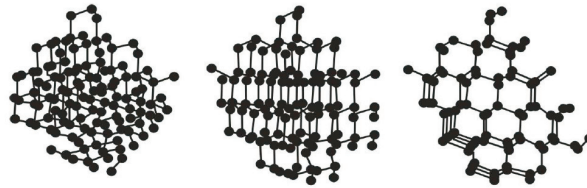


Figure 2.6: A silicon crystal is seen from different angles. On the left, it is viewed from a random angle so that the structure appears to be amorphous. In the middle, the sample is rotated and channels formed by horizontal planes can be seen. On the right, with proper angles, channels are formed by lines of silicon atoms. Adapted from [11].

within the channels will be weak, merely deflecting the trajectory of ions at small angles. In practical terms, this implies that the number of backscattered particles and, consequently, the count, will drop significantly, except when there is something blocking the channels. Figure 2.7 compares an RBS spectrum in which the sample is not aligned with the beam (referred to as a random spectrum) with a spectrum for which the beam is aligned with a crystallographic direction, i.e., it is channeled. In the channeled spectrum, the number of counts originating from the crystalline substrate is reduced, making it easier to detect the silicon atoms in the amorphous layer on the surface. The number of counts on the y-axis in the Figure 2.7 is formally called the yield. From RBS spectra collected in random and channeling alignments,

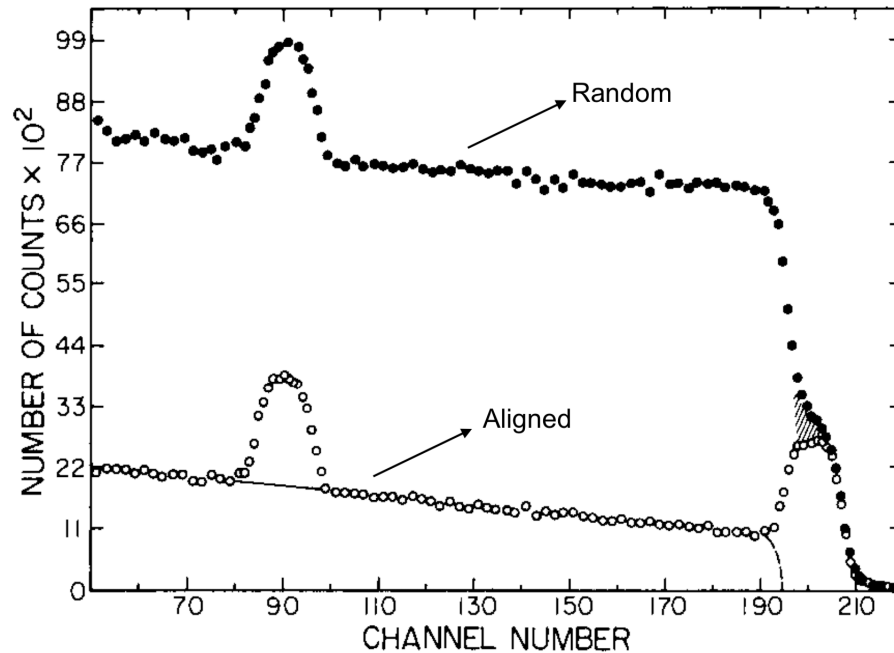


Figure 2.7: Comparison between a channeled (aligned) spectrum and a random spectrum from crystalline Si covered with 130 nm SiO<sub>2</sub>. The peak at channel 200 comes from Si in the oxide. The peak at channel 90 is from oxygen. Adapted from [11].

it is possible to calculate the concentration of interstitial defects  $N_d(z)$  at the depth  $z$  by

$$N_d(z) = \chi(z) N, \quad (2.7)$$

where  $N$  is the atomic density of the host material in atoms/cm<sup>2</sup>, and  $\chi(z)$  is the ratio of the aligned yield to the random yield at depth  $z$  [13].

This technique is applied for the quantification and spatial distribution analysis of crystal disorder within the crystal lattice, specifically focusing on interstitial defects. Additionally, it facilitates the determination of composition and thickness in amorphous layers, as well as the assessment of the substitutability of impurity atoms within the lattice.

The equipment used for RBS characterization is part of the Tandatron Accelerator Laboratory at Western University [6], as shown in Figure 2.2. The dedicated RBS line has a chamber where the sample holder is a high precision 4-axis manipulator that allows targeting of the sample within  $\pm 0.5$  mm and orientation of the sample with respect to the ion beam with a precision of hundredths of a degree. A particle detector is placed inside the chamber to perform

the backscattered particle counting linked to a data acquisition system with a multichannel analyzer (MCA). Silicon barrier detectors are the type of detectors employed. Upon penetrating the detector, each particle generates an electrical signal that is amplified and sent to a multichannel analyzer. The multichannel analyzer sends a signal to a specific channel based on the amplitude of the received signal. Each channel has a counter that accumulates the number of signals received from the multichannel analyzer, thus determining the number of particles that reached the detector within each energy range. The energy resolution of the detector is 12 keV, and it typically has solid-angle-defining aperture (slit) of  $1.0 \text{ mm} \times 0.2 \text{ mm}$  with the longer dimension oriented vertically.

### 2.2.3 Photoluminescence (PL)

Photoluminescence spectroscopy is a contactless and non-destructive method to investigate the electronic structure of materials. A light beam with defined wavelength strikes a sample causing a deviation from the equilibrium condition in a process called photoexcitation. The excess energy provided by the light source can be absorbed in different ways. One of them is the energy absorption by valence electrons, which the photoexcitation process causes electrons within the material to move to permissible excited states. When these electrons return to their equilibrium states, their excess energy is released, which may include light emission or not (radiative and non-radiative processes). This phenomenon of light emission by the sample is called luminescence. For the case of photon excitation, this luminescence is called photoluminescence. Figure 2.8 illustrates this process.

The energy of the emitted light (photoluminescence) is related to the energy difference between the two levels of the electronic states involved in the transition. The most common radiative transition in semiconductors is between states located in the conduction and valence bands, whose energy difference is the prohibited bandwidth (bandgap). However, if the excitation energy is less than the prohibited bandwidth, no optical absorption will occur as long as the material does not have any impurity or defect levels within the prohibited bandwidth. Through PL measurements, the bandgap can be determined, which is particularly useful when working with new semiconductor compounds. Radiative transitions in semiconductors also

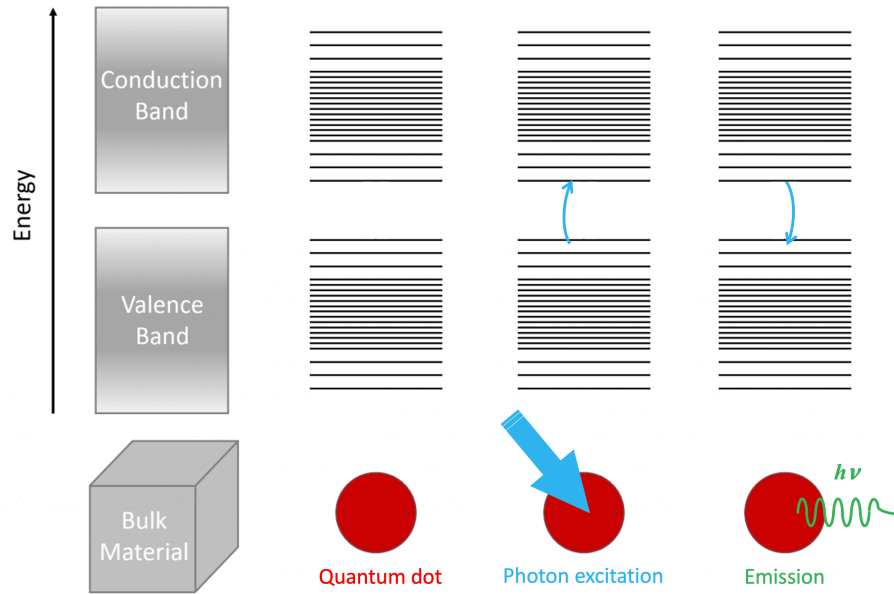


Figure 2.8: Basic representation of a radiative recombination process (photoluminescence), where the incident light beam is represented in blue, while the emitted light due to the recombination process is represented in green. Adapted from [14].

involve levels of localized defects. The photoluminescence energy associated with these levels can be used to identify specific defects and the intensity of the PL to determine their concentration. The return to the equilibrium condition, also known as recombination, can involve both radiative and non-radiative processes. In this way, photoluminescence analysis can help to understand the physics behind the recombination mechanisms.

In this project, steady-state photoluminescence measurements were carried out at room temperature to study the emission of the QDs in the UV-Vis and NIR ranges. Photoluminescence in the time domain (time-resolved photoluminescence - TRPL) was employed to study the lifetime of these recombination processes. More details about this technique and its variations can be found in [15].

Steady-state PL and TRPL at room-temperature were obtained using the Horiba Fluorolog-QM-75 [16] with the Hamamatsu photomultiplier (PMT) R928 detector for the ultra-violet-visible (UV-Vis) and the DSS-IGA020 InGaAs solid state detector (photodiode) for the near-infrared (NIR) range. Figure 2.9 shows their quantum efficiency and responsivity for the PMT and the photodiode, respectively.

The system is equipped with a 75 W Xe arc lamp for steady-state measurements and, de-

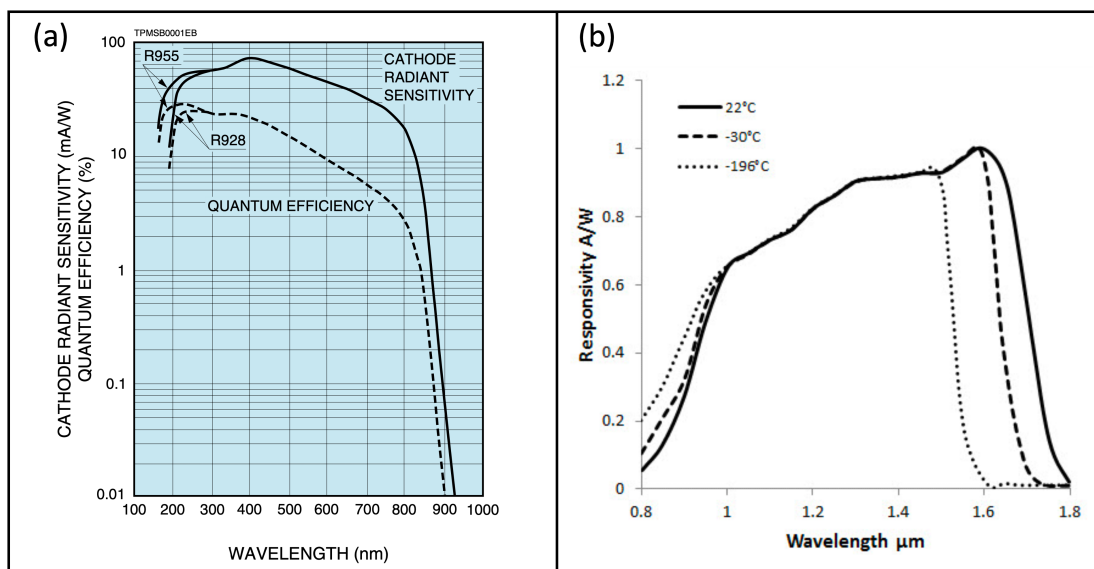


Figure 2.9: Efficiency properties of the photodetectors used in this work: (a) PMT R928 quantum efficiency, (b) DSS-IGA020 photodiode responsivity. Reproduced from [17] and [18].

pending on the lifetime to be measured, it has a pulsed laser [19] and pulsed LED [20] for time-resolved measurements. Figure 2.10 shows the system used for PL and TRPL measurements.

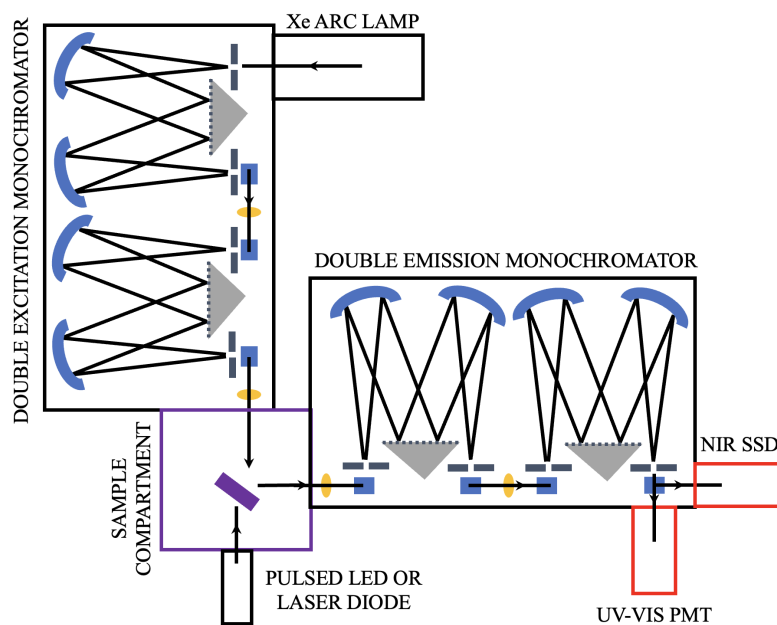


Figure 2.10: Horiba Fluorolog-QM-75-22 system schematic used in this work.

## 2.2.4 Low energy electron diffraction (LEED)

Low-energy electron diffraction is a surface and near-surface technique in which low-energy electrons (0 - 500 eV) are directed towards the surface of the sample being measured. As these electrons collide with the surface of the sample, they diffract in different directions depending on the surface crystallography. After the diffraction, they pass through the retarding grids in the spectrometer and collide with a phosphor screen, which emits light and shows a diffraction pattern. This process is illustrated in Figure 2.11(a). The pattern that is created on the phosphor screen is called a LEED pattern, and it is shown in Figure 2.11(b). The LEED pattern is a reciprocal space representation of the surface lattice structure with long range order [21]. It is worth highlighting that LEED is a technique used only for single crystals, and if the sample is not conductive, charging may occur, making the characterization not feasible. The intensity of the diffraction peak depends on the electron flux, and the pattern can provide information on the symmetry and geometry of crystal structure on the sample surface, as well as surface overlayers [23].

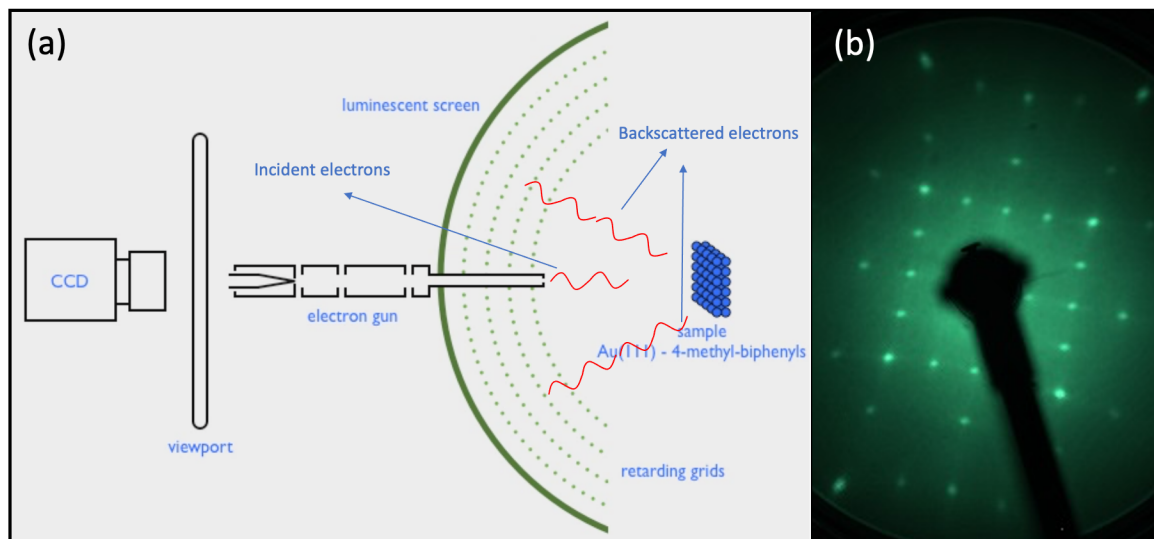


Figure 2.11: (a) Working principle schematic of LEED. (b) Example of a LEED pattern. Adapted from [22].

Additional research was done in this thesis to calculate the surface Debye temperature based on the intensity of the low energy diffraction spots of a solid sample. In particular, I analyzed specific diffracted spot intensities as a function of temperature to calculate the Debye temperature of silicon samples. These samples have different concentration of defects, allowing one to associate the Debye temperature to the concentration of defects and disorder within the near-surface region. The details about this procedure are described in the next chapter.

The equipment used to obtain LEED patterns was the INTEGRAL-LEED Spectrometer model BDL800IR [24] located at OCI Vacuum Microengineering Inc.. Its schematic is presented in Figure 2.12.

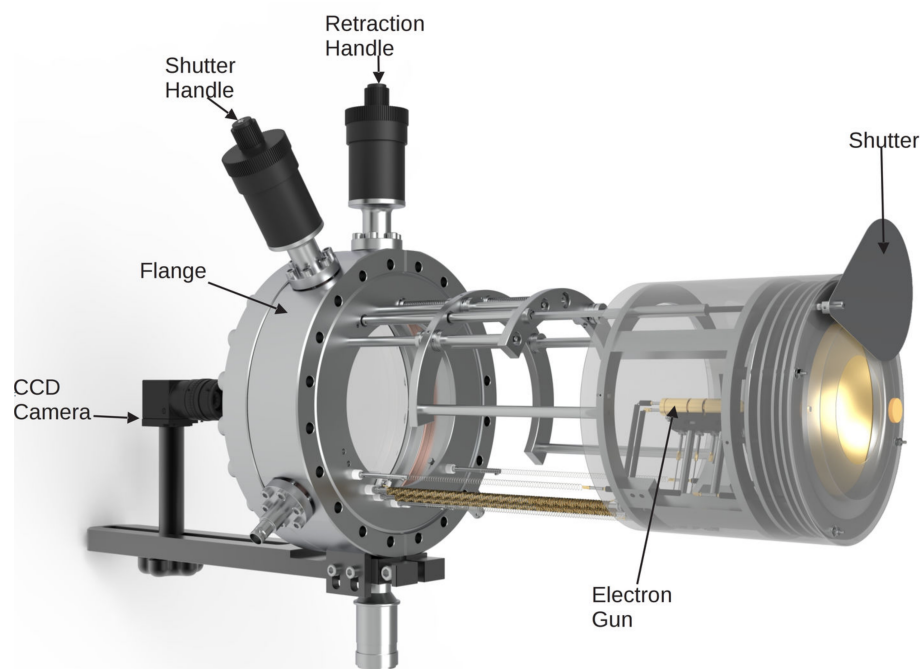


Figure 2.12: LEED spectrometer used in this work. Copied from [24].

### 2.2.5 Other techniques

In addition to the characterization techniques presented so far, supplementary methods were also employed in this thesis, although to a lesser extent. Positron annihilation spectroscopy (PAS), Raman spectroscopy, and X-ray diffraction were employed as supportive techniques and were conducted either through collaboration or at external user facilities. Positron annihilation spectroscopy (PAS) offers insights into the structural defects (vacancies) in materials by



analyzing the annihilation of positrons with electrons. Raman spectroscopy provides valuable information about molecular vibrations, contributing to the identification of compounds and structural changes, and X-ray diffraction enables the investigation of the crystalline structures of our quantum structures. Despite their importance in complementing the overall analysis, a detailed discussion of these techniques is not provided in this thesis due to their limited use and the collaborative nature.

# References

- [1] A.D. Pogrebnjak (Ed.), *Ion Implantation: Synthesis, Applications and Technology* (Nova Science Publishers, Hauppauge, NY, USA, 2019).
- [2] R. Hellborg, H. Whitlow, Y. Zhang (Editors) *Ion Beams in Nanoscience and Technology* (Springer, New York, NY, USA, 2010).
- [3] M. Nastasi and J. W. Mayer, *Ion Implantation and Synthesis of Materials* (Springer Berlin Heidelberg, 2006).
- [4] <http://www.srim.org/index.htm>  
Accessed on January 31st, 2024.
- [5] <https://hzdr-innovation.de/en/products/simulation-software-tridyn/>  
Accessed on March 1st, 2024.
- [6] [https://isw.physics.uwo.ca/facilities\\_techniques/index.html](https://isw.physics.uwo.ca/facilities_techniques/index.html).  
Accessed on January 20th, 2024.
- [7] Hugh O. Pierson, *Handbook of Chemical Vapor Deposition (CVD): Principles, Technology, and Applications* (Noyes Publications, 1999)
- [8] F. Iacona, G. Franzò, and C. Spinella, Correlation between Luminescence and Structural Properties of Si Nanocrystals, *Journal of Applied Physics* 87, 1295 (2000).
- [9] <https://www.semicore.com/news/118-what-is-plasma-enhanced-chemical-vapor-deposition-pecvd>  
Accessed on March 1st, 2024.
- [10] <https://nanofab.uwo.ca>.  
Accessed on February 1st, 2024.
- [11] W. K. Chu, J. W. Mayer, and M. A. Nicolet, *Backscattering Spectrometry* (Academic Press, 1978).

- [12] H. Bernas (Editor), *Materials Science with Ion Beams* (Springer Berlin Heidelberg, 2010).
- [13] Y. Wang, M. Nastasi, *Handbook of Modern Ion Beam Materials Analysis* (Materials Research Society, 2009).
- [14] <https://www.edinst.com/perovskite-quantum-dots/>  
Accessed on January 31st, 2024.
- [15] J. R. Lakowicz (Editor), *Principles of Fluorescence Spectroscopy* (Springer US, 2006).
- [16] <https://www.horiba.com/int/scientific/products/detail/action/show/Product/fluorolog-qm-1997/>  
Accessed on January 20th, 2024.
- [17] [https://www.hamamatsu.com/us/en/product/optical-sensors/pmt/pmt\\_tube-alone/side-on-type/R928.html](https://www.hamamatsu.com/us/en/product/optical-sensors/pmt/pmt_tube-alone/side-on-type/R928.html)  
Accessed on January 20th, 2024.
- [18] <https://static.horiba.com/fileadmin/Horiba/Products/Scientific/OpticalComponentsandOEM/SinglepointDetectors/SolidstateDetectors/DSS-IGA020.pdf>  
Accessed on January 20th, 2024.
- [19] <https://www.horiba.com/pol/scientific/products/detail/action/show/Product/deltadiode-1101/>  
Accessed on January 20th, 2024.
- [20] <https://www.horiba.com/int/scientific/products/detail/action/show/Product/spectraled-1095/>  
Accessed on January 20th, 2024.
- [21] D. J. O'Connor, B. A. Sexton, and R. St. C. Smart, *Surface Analysis Methods in Materials Science* (Springer Berlin Heidelberg, 1992).
- [22] [http://www.ocivm.com/lowenergyelectron\\_diffraction.html#LEED-Animation](http://www.ocivm.com/lowenergyelectron_diffraction.html#LEED-Animation)  
Accessed on January 20th, 2024.
- [23] M. A. Van Hove, W. H. Weinberg, and C.-M. Chan, *Low-Energy Electron Diffraction: Experiment, Theory and Surface Structure Determination* (Springer Berlin Heidelberg, 1986).

- [24] [http://www.ocivm.com/spectrometer\\_dl800ir.html](http://www.ocivm.com/spectrometer_dl800ir.html)  
Accessed on January 20th, 2024.

# Chapter 3

## Surface Debye temperature determination from LEED: correlation to defects in epitaxial films<sup>1</sup>

### 3.1 Introduction

The Debye temperature ( $\theta_D$ ) of a solid is an important parameter for materials because of the role it plays in many electronic and thermodynamic properties. This temperature is a representation of the stiffness of the bonds between atoms and it is defined as [1]:

$$\theta_D = \frac{\hbar}{k_B} \omega_D, \quad (3.1)$$

where  $\hbar$  is Planck's constant divided by  $2\pi$ ,  $k_B$  is Boltzmann's constant, and  $\omega_D$  is the Debye characteristic frequency, which is associated with the highest frequency phonon mode. Above this frequency, more molecular or atomic vibration is observed to the detriment of collective vibration.

The under-coordinated surface atoms of a solid tend to be more loosely bound and more energetic than their bulk counterparts [2, 3]. The Debye temperature tends to decrease in the vicinity of the surface such that the end point value found for the top atomic layer is known as the surface Debye temperature. The impact of the surface  $\theta_D$  is significant. The increased

---

<sup>1</sup>This chapter is reproduced with permission from Surface Science volume 723 (2022) by Matheus C. Adam et al., DOI: <https://doi.org/10.1016/j.susc.2022.122104>

vibrational amplitude at the surface, due to the lower surface Debye temperature, can allow for the melting of a solid from the surface inward in some materials [2] at temperatures below the bulk melting point. An important interconnected phenomenon is the presence of defects in the surface and near-surface layers. Interpretation of surface  $\theta_D$  is more complex in the presence of defects [4], motivating research to develop new tools to study defects and their contribution to the surface Debye temperature [5]. The sensitivity of  $\theta_D$  to defects, and the ability to extract  $\theta_D$  from temperature-dependent low energy electron diffraction (LEED) measurements, suggest the possibility to use LEED as a tool for near-surface defect quantification.

The Debye temperature in the bulk and on surfaces has been measured using various experimental techniques, including x-ray diffraction [6, 7], helium atom scattering [8, 9], reflection high energy positron diffraction [10], ultraviolet photoemission spectroscopy [11], and Mossbauer spectroscopy [12]. The ability of such techniques to measure the true surface Debye temperature, rather than the bulk or a combination of the surface and bulk, depends on their surface specificity. LEED uses the constructive interference of a mono-energetic beam of electrons in the low energy range of 10 – 1000 eV that has been scattered off the surface of a single crystal to measure the interatomic distances and elucidate the surface structure [3]. LEED diffraction patterns can be used to probe surface structures and distances with high sensitivity. LEED diffraction patterns are modelled using dynamical LEED theory, which takes into account the preponderance of multiple scattering events. LEED peak intensities and widths depend on the temperature, i.e. on the vibration of atoms on the surface. There have also been efforts in the past to determine surface  $\theta_D$  using LEED complemented by theoretical approaches [13, 14].

LEED is commonly employed to probe the properties of surfaces, such as structure or disorder, since low-energy electrons which interact strongly with matter are sensitive to only a limited number of atomic layers near the surface. Within the kinematic approximation, the intensity of diffracted electrons  $I$  can be written as [3]:

$$I - I_b = I_0 e^{-2M} , \quad (3.2)$$

where  $I_b$  is the background intensity,  $I_0$  is the incident intensity, and  $2M$  is the Debye-Waller factor. This factor is a function of the electron mass  $m_e$ , the electron energy  $E$ , the angle of

incidence  $\alpha$ , the inner potential of the crystal  $V_0$ , the temperature  $T$  of the sample, the mass of the atoms in the crystal  $m_a$ , Boltzmann's constant  $k_B$ , and the Debye temperature  $\theta_D$ :

$$2M = \frac{24 m_e (E \cos^2 \alpha + V_0)}{m_a k_B (\theta_D)^2} T . \quad (3.3)$$

Calculation of the surface Debye temperature experimentally from a LEED pattern is relatively straightforward, as equations (3.2) and (3.3) can be rewritten to provide  $\ln[(I - I_b)/I_0]$  as a function of  $T$ . Then the surface  $\theta_D$  is obtained by measuring the intensities of the diffraction peaks as a function of temperature. It is important to note that the measured  $\theta_D$  is an average over a few layers of the sample that are penetrated by the electron beam. At electron energies in the range of 50 – 150 eV, the mean free path of electrons is at its minimum ( $\approx 5 - 8 \text{ \AA}$ ), and  $\theta_D$  can be called the surface Debye temperature [3].

Ideal defect-free solids have characteristic bulk  $\theta_D$  values. In real materials it is known that defects will contribute to disorder in the bulk and on the surface, and therefore will contribute to the diffraction peak width and peak profile. This fact will lead to a different Debye temperature. Defect characterization and quantification play an important role in materials science, and defect engineering can be used to modify optical and electrical properties of materials to suit different applications. No single experimental technique can address all type of defect characteristics and concentrations. For example, positron annihilation offers very high sensitivity for open volume defects (vacancies, vacancy clusters, voids), for concentrations as low as  $10^{16} \text{ cm}^{-3}$  [15, 16, 17], however the technique saturates at a moderate concentration of about  $10^{19} \text{ cm}^{-3}$  [18], limiting its range of application. Ion scattering using channeling offers sensitivity to interstitials, lattice disorder and thermal vibrations. It has been applied to point defects produced by irradiation [19] and to dislocations [20]. High resolution electron microscopy is useful to visualize extended defects (voids, dislocations) but produces local measurements and typically requires lengthy sample preparation which may modify initial defect structures [21].

The goal of this paper is two-fold. First, we examine the experimental methodology for the determination of surface Debye temperature by LEED. The second goal is to provide a preliminary evaluation of the ability to quantify near-surface defects by LEED, by a comparison between single crystal silicon and silicon heteroepitaxial films. LEED measurements can be

used to measure the Debye temperature of a solid sample, and the calculated Debye temperature can be correlated with defects and disorder in the near-surface region. To corroborate this method, we compare  $\theta_D$  calculations with ion channeling and positron annihilation spectroscopy (PAS) measurements conducted on the same set of samples.

## 3.2 Experimental details

Two silicon films with 1.0  $\mu\text{m}$  and 0.6  $\mu\text{m}$  thicknesses were grown by hetero-epitaxy on  $\text{Al}_2\text{O}_3$  (1102) sapphire substrates, here referred to as SoS. The sapphire substrates were oriented along the R-plane. Additionally, a p-doped Si (001) single crystal sample with nominal resistivity in the range from 1 to 10  $\Omega \cdot \text{cm}$  was used as a defect-free reference. Two epitaxial film thicknesses allow us to study and to compare defect relaxation towards the surface in the epitaxial layers, since the lattice mismatch between Si and  $\text{Al}_2\text{O}_3$  produces strain which is a maximum at the interface and decreases as the film grows, which reduces the number of defects. Prior to loading the reference sample into the vacuum system, hydrogen fluoride (HF) etching was done to remove surface oxide, unless stated otherwise.

A low energy electron diffraction (LEED) instrument incorporating a position-sensitive pulse-counting detector with high bias current microchannel plates was used to rapidly collect digital LEED images with low total electron exposure. LEED measurements were conducted at OCI Vacuum Microengineering. Details of this system can be found on OCI's website [22]. A contamination-free silicon surface was identified by obtaining a  $2 \times 1$  Si (001) LEED pattern after heating the sample in UHV. In order to calculate the surface Debye temperature  $\theta_D$ , we used MultLEED software [22] to select the peak of interest. Next, the sample was heated to 700°C using an e-beam heater installed behind the sample. Then the intensity  $I$  of the diffraction peak was recorded as a function of temperature during controlled cooling to room temperature. Multiple peak intensities were recorded at different electron energies and compared, and the most representative examples are shown in the results section below.

Rutherford backscattering spectroscopy (RBS) was applied to probe elemental depth profiles for all samples, in random and channeling geometries. When a highly collimated beam of ions is directed at a crystalline target along a direction of high symmetry, deflection of the in-



cident ions from the atoms along a row parallel to the beam leads to the formation of a shadow cone, therefore reducing the probability of scattering from lattice atoms located deeper within the crystal. In the channeling geometry, the majority of ions cannot be scattered until they collide with an interstitial atom, resulting in a small angle deflection. The measurements were carried out at the Western University Tandatron Accelerator Facility, using a monoenergetic beam of  $\text{He}^+$  at 2.0 MeV with a Si charged particle detector positioned at a scattering angle of  $170^\circ$ . For random geometry spectra, samples were continuously rotated around the azimuth with a tilt angle of  $5^\circ$  during data acquisition to avoid channeling. For channeling measurements, samples were aligned to the [001] crystallographic direction to quantify the number of atoms in the crystalline lattice that were displaced from their ideal lattice sites. Sb-implanted Si and diamond-like carbon standards were used to calibrate the solid angle of the detector and its channel-to-energy conversion coefficient. The uncertainty of ion yields obtained by RBS measurements derived from this process is close to 3.5%. Sb areal density was estimated with an accuracy of approximately 2.2%. RBS spectra were fitted using SIMNRA [23], a MS Windows software for the simulation of charged particle energy spectra for ion beam analysis with incident ions from about 100 keV to many MeV, to determine film thicknesses and compositions.

In addition to LEED and RBS, positron annihilation spectroscopy (PAS) was used to provide complementary information on defect structures in the films. A monoenergetic beam of positrons obtained from a  $\text{Na}^{22}$  source, of controlled energy from 25 eV to 70 keV, was applied to the samples. The broad energy spectrum of the beta decay is moderated with a thin tungsten single crystal foil to obtain monoenergetic positrons. The system has a high purity Ge detector with energy resolution of 1.40 keV FWHM at the annihilation line energy of 0.511 MeV. Positrons annihilate with electrons in the sample, producing two 511 keV gamma rays. The 511 keV annihilation lineshape is Doppler broadened due to the motion of the annihilating electron, thus the lineshape is sensitive to the electronic environment. In particular, positrons tend to trap into vacancy-type defects, which is observed by a reduction in Doppler broadening. The lineshape is parameterized using the “S”, or “sharpness” parameter – more defects result in an increase in S. Data analysis is confounded by the broad positron implantation profile, and the positron diffusion that occurs after implantation. Data are modelled using POSTRAP [24]

which takes a user-supplied model as input, and generates  $S$  vs positron energy for comparison to experimental data. PAS measurements were performed at the Institute of Materials Research at Washington State University. Positron-beam techniques are non-destructive, possess a high detection sensitivity for vacancy and open volume defects, have no need for sample preparation, and have moderate depth resolution [15, 16, 17]. These characteristics are appropriate to our study and complement RBS measurements since RBS is sensitive mostly to interstitial defects.

### 3.3 Results and discussion

Multiple LEED patterns were acquired for all three samples at multiple energies and three diffraction spots were selected for Debye temperature analysis for quantification and comparison:  $(0\ 1)$ ,  $(-1/2\ 0)$ , and  $(1\ 1)$ . The fit of the natural log of LEED intensities for  $(0\ 1)$  diffraction spots as a function of temperature is shown in Figure 3.1. Note that while diffraction intensity

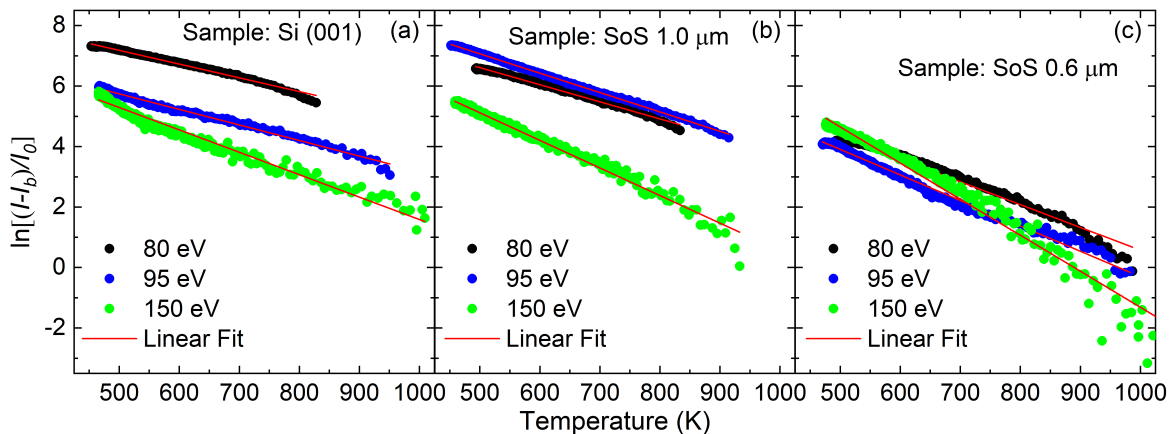


Figure 3.1: LEED diffraction intensities measured at spot  $(0\ 1)$  as a function of temperature for samples (a) Si  $(001)$ , (b) SoS  $1.0\ \mu\text{m}$ , and (c) SoS  $0.6\ \mu\text{m}$ .

slopes were reproducible for the same energy, different slopes were measured for different incident energies: 80, 95 and 150 eV. We can observe that for temperatures above 900K, there is significant scatter in the peak intensities, especially for SoS  $1.0\ \mu\text{m}$  and SoS  $0.6\ \mu\text{m}$  measured at 150 eV. This can be related to the reconstruction of the Si surface that occurs at about this temperature [25, 26]. In order to avoid the noisy data in this region, the linear fitting was

performed for temperatures below 850K for these samples and this energy. The linear fitting process for the (0 1) spot has a slope standard error of 0.5% on average, and the results of the linear fits for all samples at different spots and energies are presented in Table 3.1.

Sample	Fitting parameters	Spot (0 1)			Spot (-1/2 0)			Spot (1 1)		
		80 eV	95 eV	150 eV	80 eV	95 eV	150 eV	80 eV	95 eV	150 eV
Si (001)	Slope	4.54	5.14	7.40	4.38	5.01	7.05	4.61	4.73	6.78
	Std. dev.	3.43	3.48	7.48	5.24	8.61	55.5	50.1	5.51	43.0
	R <sup>2</sup>	0.988	0.989	0.974	0.978	0.964	0.560	0.233	0.988	0.770
SoS 1.0 $\mu\text{m}$	Slope	5.65	6.40	9.12	5.52	6.00	8.90	5.24	5.76	7.80
	Std. dev.	3.52	1.10	5.85	5.61	3.26	14.9	3.93	3.13	7.28
	R <sup>2</sup>	0.994	0.999	0.987	0.986	0.990	0.930	0.984	0.994	0.976
SoS 0.6 $\mu\text{m}$	Slope	7.57	8.43	11.9	5.92	6.56	10.0	6.39	6.19	9.12
	Std. dev.	7.63	4.44	11.0	8.83	2.40	41.6	4.28	3.51	15.5
	R <sup>2</sup>	0.977	0.991	0.976	0.980	0.996	0.740	0.988	0.994	0.937

Table 3.1: Fitting results for all spots and energies used in LEED measurements. The absolute value of the slope is presented in  $\times 10^{-3} \text{ K}^{-1}$  and its standard deviation is in  $\times 10^{-5} \text{ K}^{-1}$ .

Figure 3.2 presents surface  $\theta_D$  results obtained from LEED measurements for all samples at three different energies (80 eV, 95 eV and 150 eV) and at three different spots: (0 1), (-1/2 0), and (1 1)<sup>2</sup>. The value of  $\theta_D$  averaged over the three energies at which LEED patterns were

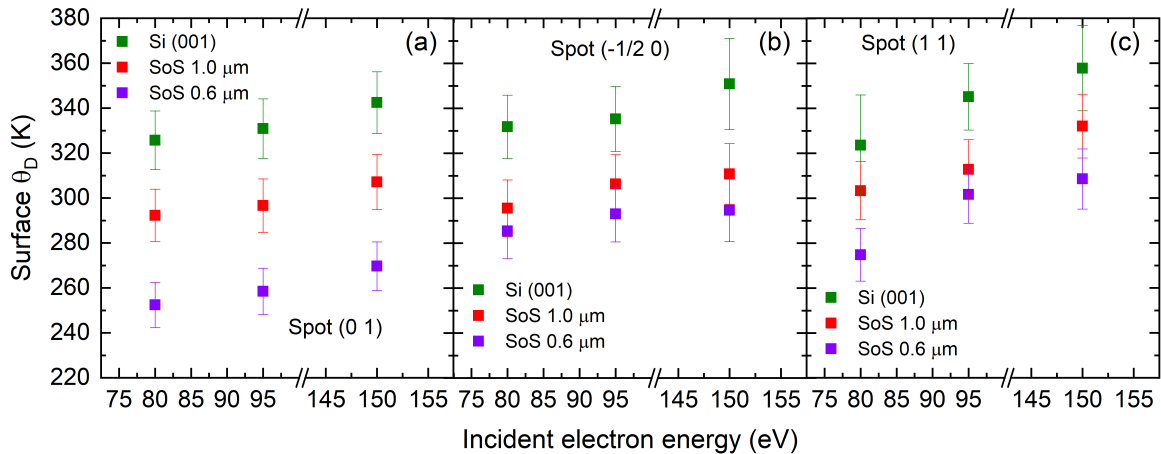


Figure 3.2: Calculated surface Debye temperature from LEED measurements at 80 eV, 95 eV and 150 eV incident electron energy, at spots (a) (0 1), (b) (-1/2 0), and (c) (1 1). Table 3.2 presents a summary of surface  $\theta_D$  measured for these energies.

taken at spot (0 1) is 333 K for the reference sample Si (001), 299 K for SoS 1.0  $\mu\text{m}$ , and

<sup>2</sup>Spot (-1/2 0) corresponds to the reconstructed surface, while spots (0 1) and (1 1) correspond to the non-reconstructed surface.

260 K for SoS  $0.6 \mu\text{m}^3$ . Surface  $\theta_D$  calculated from LEED patterns is summarized in Table 3.2.

		Spot (0 1)			Spot (-1/2 0)			Spot (1 1)		
		80 eV	95 eV	150 eV	80 eV	95 eV	150 eV	80 eV	95 eV	150 eV
Si (001)	$\theta_D$	326	331	342	332	335	351	323	345	358
	$\delta\theta_D$	13	13	14	14	15	20	22	15	19
SoS 1.0	$\theta_D$	292	297	307	296	306	311	303	313	332
	$\delta\theta_D$	12	12	12	13	13	13	13	13	14
SoS 0.6	$\theta_D$	252	258	270	285	293	295	275	302	308
	$\delta\theta_D$	10	10	11	12	12	14	12	13	13

Table 3.2: Surface  $\theta_D$  and its total uncertainty  $\delta\theta_D$  calculated from LEED measurements at spots (-1/2 0) and (1 1) for incident electron energies of 80 eV, 95 eV and 150 eV. All values in Kelvin.

Our experimentally measured values are lower than the bulk Si value reported in the literature [1], which is 645 K. Nonetheless, our results are consistent with previous studies in which a Si surface  $\theta_D$  temperature of 340 K at 75 eV was measured using the same method we used in this work [27]. Lower surface  $\theta_D$  calculated from LEED compared to bulk  $\theta_D$  has been reported in the literature for several semiconductors and metals, as shown in Table 3.3.

	Surface $\theta_D$ (K)	Bulk $\theta_D$ (K)
Si (001) [27]	340	645
Ge (001) [28]	215	290
Al (001)	189	370
Ag (111)	155	225
Cu (001)	210	322

Table 3.3: Comparison between surface and bulk  $\theta_D$  for several semiconductors and metals. Adapted from [3], except where indicated.

We observe for all samples that surface  $\theta_D$  increases as the electron incident energy increases. This behaviour has been previously observed [2] and it is due to sampling depth in the crystal, i.e. the larger the probing energy, the more atomic layers contribute to the diffraction pattern, which brings more contribution from the bulk vibration modes. The Debye temperature value (330 K) deduced from our analysis is lower compared to results by Dygo et. al.

<sup>3</sup>For a given sample, the spot (0 1) has the same surface  $\theta_D$ , within the uncertainty, across all energies. The average surface  $\theta_D$  measured at the spot (0 1) is equal to  $333 \pm 13$  K for the reference sample Si (001),  $299 \pm 12$  K for SoS  $1.0 \mu\text{m}$ , and  $260 \pm 10$  K for SoS  $0.6 \mu\text{m}$ , showing higher surface  $\theta_D$  for thicker films. This comparison fails the overlap test for the other spots due to the lack of good experimental data, leading to higher uncertainty.

[29] where  $\theta_D$  of  $490 \pm 15$  K was calculated from ion channeling data, which is sensitive to collective vibrations in the near-surface region that can be 50 – 100 nm thick. On the other hand, Soares et. al. [13] have studied surface Debye temperature and thermal vibrations using a layer-by-layer approach. They have applied LEEDFIT code on CdTe (110) LEED patterns and were able to find good values for the vibrational amplitudes of the first two planes of atoms. This is the only example we are aware of in which layer-by-layer estimates were done for semiconductor Debye temperatures, and contributions of defects were not considered [13]. Our method gives an averaged value for the top surface Debye temperature, but additionally provides information on defect density, as we discuss below.

The total uncertainty of surface  $\theta_D$  ( $\delta\theta_D$ ) calculated from LEED measurements is represented by the error bars in Figure 3.2 and is equal to 4%, for spot (0 1). It was calculated considering two contributions: the linear fitting process standard error of 0.5% and the relative uncertainty in the incident beam energy values, which is close to 3% (incident electron energy is one of the parameters in Eq. (3.3)). Other sources of uncertainty like the incident angle  $\alpha$  and the temperature  $T$  were not considered in uncertainty analysis because they have contributions smaller than 0.5%. For the other two spots, the standard error of the linear fitting process was not uniform. Therefore,  $\delta\theta_D$  was calculated for each point and is presented in the Table 3.2.

Next, we establish the connection between surface Debye temperature and defect concentrations on the Si surface. Figure 3.3 presents RBS results obtained with random and channeling alignments for the three samples described in the previous section. Figure 3.3(a) shows the RBS spectrum obtained from the Si (001) reference sample with the native oxide layer removed prior to analysis. Scattering yield for the sample aligned in the [001] direction is compared to a random geometry spectrum. Single crystal Si (001) in channeling mode exhibits mostly scattering from disordered surface layers, with a surface peak at 1130 keV and with very low scattering yield ( $\chi_{dc} < 2 - 3\%$ ) below the surface corresponding to a very low defect concentration, as expected.

Good epitaxy can be achieved only when the lattice parameters of the substrate and epitaxial film are almost the same. When the stress in a strained epitaxial layer exceeds its elastic modulus, the strain is accommodated by the creation of misfit dislocations in Si and Ge films [30]. From RBS spectra collected in random and channeling alignments, we have calculated

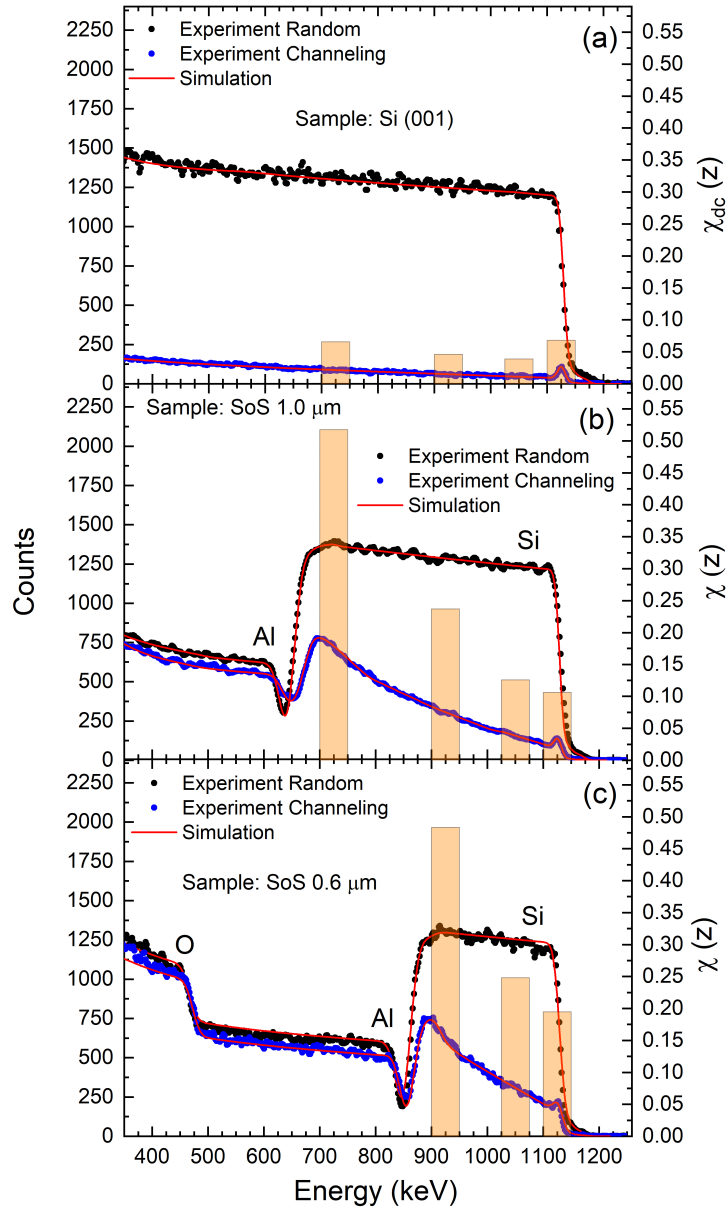


Figure 3.3: Random and channeling spectra along with the normalized yield  $\chi$  on the right scale, of samples (a) Si (001), (b) SoS 1.0  $\mu\text{m}$ , and (c) SoS 0.6  $\mu\text{m}$ .

the normalized yield  $\chi(z)$  in order to quantify the amount of interstitial defects detected when comparing random and channeling modes on the samples SoS 1.0  $\mu\text{m}$  and SoS 0.6  $\mu\text{m}$ , in Figure 3.3(b) and 3.3(c), respectively. This parameter is defined as the ratio of the aligned yield to the random yield, and it is presented as a histogram with its scale on the right axis of Figure 3.3. In Figure 3.3(a),  $\chi_{dc}(z)$  is the dechanneled fraction of incident ions at depth  $z$ , and was calculated by dividing the aligned yield by the random yield for the reference sample Si (001).

As this sample is a high purity bulk crystal, it is assumed to have considerably fewer defects than the epitaxial layers, i.e. we assume all contributions to  $\chi_{dc}(z)$  originate from dechanneling effects and multiscattering events. Therefore, the defect density in the epitaxial samples  $N_d(z)$  as a function of depth can be expressed as [31]:

$$N_d(z) = \frac{\chi(z) - \chi_{dc}(z)}{1 - \chi_{dc}(z)} N, \quad (3.4)$$

where  $N$  is the atomic density of the host material in atoms/cm<sup>2</sup>.

The energy intervals for the  $N_d(z)$  calculation presented in Figure 3.3 were chosen to represent four layers of approximately the same thickness. The first layer is at the surface (1100 – 1150 keV) and corresponds to the RBS surface peak. The second one, a near-surface layer (1025 – 1075 keV) was selected below the surface layer, and finally, two thin layers corresponding to the bulk Si (900 – 950 keV and 700 – 750 keV) were analyzed. These energy ranges correspond to depths of  $\approx 500$  nm and  $\approx 900$  nm below the surface, respectively. It is observed qualitatively that the behaviour of  $\chi_{dc}(z)$  is different when compared to  $\chi(z)$  of epitaxial films: its highest value is present at the surface, decreases in the near surface, and slightly increases in the bulk. This small increment of  $\chi_{dc}(z)$  in the bulk can be explained by the interaction of the incident particles with the crystal nuclei and their electronic cloud, which causes an increase in the probability of undergoing collisions (multiple scattering) as we probe deeper into the sample. Consequently, these interactions lead to more scattering events, which are manifested as an increment of counts and an increase in  $\chi_{dc}(z)$ . Table 3.4 presents defect densities  $N_d(z)$  obtained from ion channeling measurements for the epitaxial Si samples.

	$N_d$ (cm <sup>-2</sup> )			
	Near Si/Al <sub>2</sub> O <sub>3</sub> interface	600 nm below surface	300 nm below surface	Surface
SoS 1.0 $\mu$ m	$3.29 \times 10^{14}$	$1.36 \times 10^{14}$	$6.16 \times 10^{13}$	$7.28 \times 10^{13}$
SoS 0.6 $\mu$ m	$3.12 \times 10^{14}$	NA	$1.49 \times 10^{14}$	$1.33 \times 10^{14}$

Table 3.4: Summary of defect areal density calculations from RBS and ion channeling measurements using equation (3.4). NA stands for “not applicable”.

From comparison of the two epitaxial films, we observe that the defect concentration is the highest near the Si/Al<sub>2</sub>O<sub>3</sub> interface and decreases closer to the top surface. Energy intervals

for  $\chi(z)$  calculations were selected to be constant between the two samples to ensure we can compare the two  $N_d(z)$  values for relatively similar surface and near-surface layers. The thinner  $0.6 \mu\text{m}$  sample shows a higher defect concentration than the  $1 \mu\text{m}$  sample at their respective surface layers. This difference is expected because the SoS  $0.6 \mu\text{m}$  sample has smaller thickness to reduce lattice strain and therefore defect density. Thus, the reduction of  $N_d(z)$  values in the epitaxial films from the Si/ $\text{Al}_2\text{O}_3$  interface to the near-surface layer and finally to the surface can be connected to a gradual reduction of strain in the epitaxial film.

Figure 3.4 shows positron annihilation spectroscopy (PAS) data for all three samples, with Si (100) used as a reference. The sharpness, or S-parameter was measured as a function of

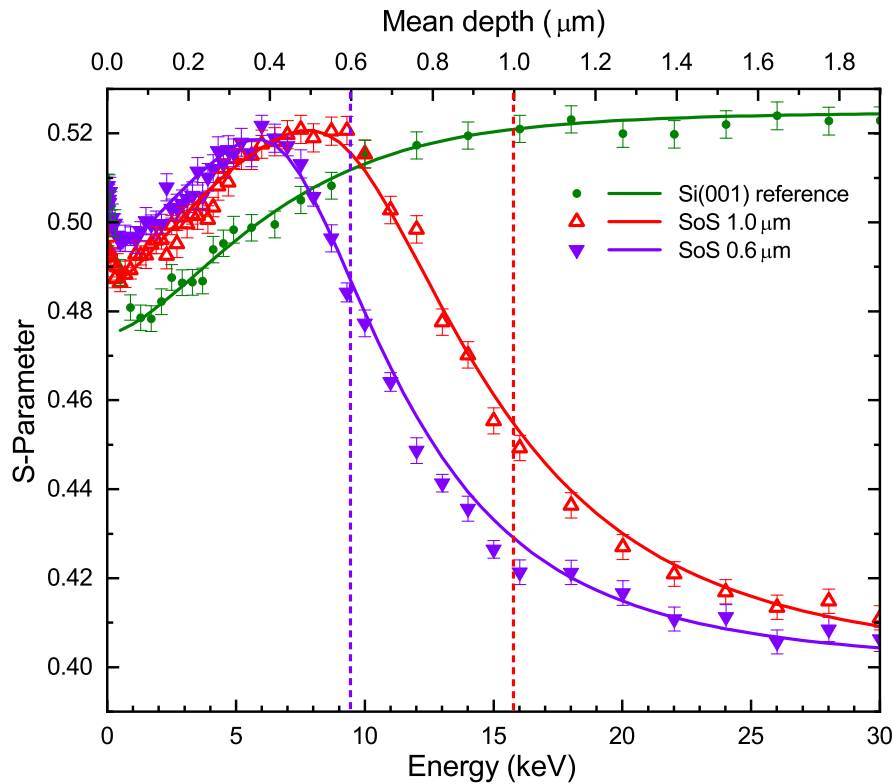


Figure 3.4: S-parameter as a function of incident positron energy and depth from 0 to 30 keV. Solid lines show results of modeling using POSTRAP.

positron energy from 0 to 70 keV which is sufficient to probe from the surface up to the Si/ $\text{Al}_2\text{O}_3$  interface, and into the sapphire bulk region. Results are presented up to 30 keV to focus on the surface and near-surface data. Solid lines show the results of modelling the



positron data using POSTRAP, and the vertical dashed lines indicate the interface position in microns and in keV.

In order to quantify defect densities from PAS<sup>4</sup>, the Si (001) reference was modelled with no defects, and with a 2000 V/cm electric field extending from the surface to a depth of 1000 nm, which is required since band-bending near the surface affects the positron diffusion. Sample SoS 0.6  $\mu\text{m}$  was divided into 2 layers each of thickness 300 nm, plus an interface layer. The modelled interface layer has a short positron diffusion length, and has the S-parameter of bulk silicon. This models the potential step at the interface which prevents positrons from diffusing from the Si layer into the substrate. The defect concentrations in the two silicon layers were constrained to have defect concentrations in the same ratio ( $\approx 2.1 : 1$ ) as the 2 layers extracted from RBS data. The calculated areal densities were  $2.25 \times 10^{12} \text{ cm}^{-2}$  from top surface down to 300 nm depth and  $4.80 \times 10^{12} \text{ cm}^{-2}$  for near the Si/Al<sub>2</sub>O<sub>3</sub> interface (from 300 nm down to 600 nm depth). Sample SoS 1.0  $\mu\text{m}$  was divided into 3 layers: 0 – 330 nm, 330 – 660 nm, 660 – 1000 nm, and an additional interface layer as described above. Defect concentrations were constrained by RBS data following the same methodology applied for the other film, which ratio is 5.3 : 2.3 : 1. Then the calculated areal densities using POSTRAP are  $7.14 \times 10^{12} \text{ cm}^{-2}$ ,  $2.97 \times 10^{12} \text{ cm}^{-2}$ , and  $1.32 \times 10^{12} \text{ cm}^{-2}$ , being higher near the interface and lower at the surface. The Table 3.5 summarizes the results calculated with POSTRAP<sup>5</sup>.

	$N_d \text{ (cm}^{-2}\text{)}$		
SoS 1.0 $\mu\text{m}$	660 – 1000 nm	330 – 660 nm	0 – 330 nm
	$7.14 \times 10^{12}$	$2.97 \times 10^{12}$	$1.32 \times 10^{12}$
SoS 0.6 $\mu\text{m}$	-	300 – 600 nm	0 – 300 nm
	-	$4.80 \times 10^{12}$	$2.25 \times 10^{12}$

Table 3.5: Summary of defect areal densities obtained from PAS measurements using POSTRAP.

Summarizing the positron results: in order to reduce the number of adjustable parameters used in fitting, the relative concentrations of defects in the layers of the sample were constrained using the relative concentrations obtained from RBS, and the overall concentration

<sup>4</sup>The POSTRAP model assumed the same defect concentration profile for each sample measured by RBS, however the defect concentration in each sample was allowed to be a free parameter.

<sup>5</sup>The POSTRAP model has a considerable number of parameters with large uncertainty. Then,  $N_d$  in the region 660 – 1000 nm for the sample SoS 1.0  $\mu\text{m}$  and  $N_d$  in the region 300 – 600 nm for the sample SoS 0.6  $\mu\text{m}$  can be considered equal within the uncertainty.

was adjusted to best fit the data, assuming the S-parameter for silicon divacancies to be 1.04 times the bulk silicon S parameter. The resulting concentrations of vacancy-type defects are approximately an order of magnitude lower than the interstitial-type defect concentrations obtained from RBS. This result is consistent with a previous report of measurements of defects in ion-implanted silicon by RBS and positron annihilation [18]. Consistent with RBS, a larger vacancy-type defect concentration was found for the thinner ( $0.6 \mu\text{m}$ ) film than for the thicker ( $1 \mu\text{m}$ ) film.

The theory and experimental method applied for calculating Debye temperatures were presented in Section 2. In addition to the usual visual inspection of the diffraction pattern with a fluorescent screen, the LEED system used for the measurements allows direct quantitative determination of the electron intensity distribution. For this purpose, we can focus on one of the (01) diffraction spots and measure the beam intensity with a position sensitive detector/multichannel plate combination. Table 3.6 summarizes the calculated surface Debye temperatures for three different energies of incident electrons, along with the concentration of defects at the surface ( $N_d(0)$ ) obtained by RBS and for the near surface layer obtained by PAS. Spot (0 1) was chosen for this comparison since it has the lowest uncertainty. Both RBS and

Sample	RBS $N_d(0)$ ( $\text{cm}^{-2}$ )	PAS near-surface layer $N_d$ ( $\text{cm}^{-2}$ )	Surface $\theta_D$ (K) (0 1)			Bulk $\theta_D$ (K) [1]
			80 eV	95 eV	150 eV	
Si (001)	$4.62 \times 10^{13}$ *	–	326	331	342	645
SoS $1.0 \mu\text{m}$	$7.28 \times 10^{13}$	$1.32 \times 10^{12}$	292	297	307	645
SoS $0.6 \mu\text{m}$	$1.33 \times 10^{14}$	$2.25 \times 10^{12}$	252	258	270	645

Table 3.6: Surface Debye temperatures ( $\theta_D$ ) calculated at spot (0 1) from LEED patterns, compared to published results for bulk Si (001), concentration of defects at the surface from RBS measurements, and concentration of defects obtained from PAS measurements for near-surface layers. \* See discussion of the interpretation of this number in the text.

positron annihilation results indicate that the thinner  $0.6 \mu\text{m}$  sample has a higher defect concentration near the surface than the  $1 \mu\text{m}$  sample, and our LEED data indicate that this results in lowering the calculated  $\theta_D$  about 40 K. A similar decrease in Debye temperature is found comparing the bulk sample of Si (001) to SoS  $1.0 \mu\text{m}$ . It is important to observe that  $N_d(0)$  obtained by RBS for Si (001) represents the number of Si atoms on the surface and it was calculated assuming  $\chi_{dc}(z) = 0$  in Eq. (3.4), according to the procedure described in [31]. Moreover, it was possible to relate surface Debye temperature to the concentration of defects  $N_d$  measured

by RBS using the following empirical equation:  $\theta_D = (365 \pm 14) - (8.1 \pm 1.5) \times 10^{-13} N_d$ , where  $\theta_D$  is in K and  $N_d$  in  $\text{cm}^{-2}$ .

It is known that Debye temperature is associated with the highest frequency phonon mode. Above this frequency (or energy), more atomic or molecular vibration and less collective (phonon) vibrations are stable to be observed<sup>6</sup>. The Debye energies calculated for our samples are  $29 \pm 1$  meV for Si (001),  $26 \pm 1$  meV for SoS  $1.0 \mu\text{m}$ , and  $22 \pm 1$  meV for SoS  $0.6 \mu\text{m}$ . Surface phonons for Si (001) have been investigated experimentally by high-resolution electron energy loss spectroscopy by Tagaki et. al. [32], who reported acoustic phonons below 17.28 meV, and 12, 20, 30, 33, 49 and 64 meV losses attributed to six vibrational modes related to the Si surface dimer. Based on our estimated Debye energy values, acoustic phonons are going to be stable in Si (001), while surface optical phonons predicted at 10 to 15.2 THz (41.4 to 66.3 meV) by other researchers computationally [33] are unlikely to be experimentally observed. The introduction of defects in the material introduces discontinuities in the crystal lattice that can break the collective modes of vibration, and so the decrease in Debye temperature reported here can be explained by the higher concentration of defects found in these films.

It is important to note that the choice of which LEED spot to use in the calculation of Debye temperature may affect the results. We have chosen the (01) diffraction spots, since  $(\frac{1}{2} 0)$  spots may have additional contributions from surface impurities. Additionally, the inclusion of the inner potential in the calculation of surface  $\theta_D$  creates difficulty, as not all crystalline substances have recorded inner potentials. In this work, only silicon was used, and experimental values of the inner potentials have been reported in the literature ranging from 9.26 V to 12.52 V [34]. An inner potential of 9.26 V was assumed in our calculations, since this value is the most consistently used in the literature. For further application to compound materials, the mass of the atoms in the crystal,  $m_a$  in equation (3.3), does not apply for diatomic crystals, which is a limitation of the theory.

---

<sup>6</sup>This means that vibrations at the atomic or molecular level become more pronounced above the Debye temperature.

### 3.4 Conclusions

In the present work, surface Debye temperature was estimated using LEED patterns as a function of temperature for Si (001) and for two Si epitaxial films of 1.0  $\mu\text{m}$  and 0.6  $\mu\text{m}$ . A lower value was found for surface  $\theta_D$  for epitaxial films than for a single crystal Si wafer. The value of  $\theta_D$  averaged over the three energies at which LEED patterns were measured is 333 K for Si (001), 299 K for SoS 1.0  $\mu\text{m}$ , and 260 K for SoS 0.6  $\mu\text{m}$ . The normalized yield  $\chi(z)$ , which is defined as the ratio of RBS aligned yield to the random yield, can be related to the concentration of interstitial defects  $N_d(z)$ .  $N_d(z)$  was calculated for different depths, having the highest concentration at the Si/ $\text{Al}_2\text{O}_3$  interface and becoming lower towards the surface. The near-surface concentration of defects calculated from RBS was  $4.62 \times 10^{13} \text{ cm}^{-2}$  for Si (001),  $7.28 \times 10^{13} \text{ cm}^{-2}$  for SoS 1.0  $\mu\text{m}$  and  $1.33 \times 10^{14} \text{ cm}^{-2}$  for SoS 0.6  $\mu\text{m}$ . PAS results also showed that the thinner epitaxial layer has more defects in the near-surface layer compared to the thicker film:  $1.32 \times 10^{12} \text{ cm}^{-2}$  for SoS 1.0  $\mu\text{m}$  and  $2.25 \times 10^{12} \text{ cm}^{-2}$  for SoS 0.6  $\mu\text{m}$ . We conclude that LEED measurements of the surface Debye temperature exhibit good sensitivity to near-surface defect concentrations, and may have potential as a quantitative tool for defect characterization, given further work to achieve calibration for a particular sample set.

# References

- [1] C. Kittel, Introduction to solid state physics, 8th ed., J. Wiley, New York, 2005.
- [2] J.T. Yates Jr., Experimental Innovations in Surface Science: A Guide to Practical Laboratory Methods and Instruments, 2nd ed., Springer International Publishing, 2015.
- [3] M.A. Van Hove, W.H. Weinberg, C.-M. Chan, Low-Energy Electron Diffraction, Springer, Berlin, 1986.
- [4] J. Spitaler, S.K. Estreicher, *Front. Mater.* 5 (2018) 70.
- [5] M. Henzler, *Appl. Surf. Sci.* 11/12 (1982) 450.
- [6] M. Chollet, J. Lechelle, R.C. Belin, J.-C. Richaud, *J. Appl. Cryst.* 47 (2014) 1008.
- [7] C. Young, J. Petrosky, J.M. Mann, E.M. Hunt, D. Turner, P.A. Dowben, *J. Phys.: Condens. Matter* 29 (2017) 035005.
- [8] W. Steurer, A. Apfalter, M. Koch, W.E. Ernst, B. Holst, *Surf. Sci.* 602 (2008) 1080 .
- [9] A. Tamtögl, M. Mayrhofer-Reinhartshuber, P. Kraus and W.E. Ernst, *Surf. Sci.* 617 (2013) 225.
- [10] Y. Fukaya, A. Kawasuso, K. Hayashi and A. Ichimiya, *Appl. Surf. Sci.* 237 (2004) 29.
- [11] C. Waldfried, D.N. McIlroy, J. Zhang, P.A. Dowben, G.A. Katrich, E.W. Plummer, *Surf. Sci.* 363 (1996) 296.
- [12] S.M. Dubiel, J. Cieslak, B.F.O. Costa, *J. Phys.: Condens. Matter* 22 (2009) 055402.
- [13] E.A. Soares, V.E. de Carvalho, V.B. Nascimento, *Surf. Sci.* 431 (1999) 74.
- [14] D.P. Jackson, *Surf. Sci.* 43 (1974) 431.
- [15] D.W. Lawther, P.J. Simpson, *Defect and Diffusion Forum* 138-139 (1996) 1.

- [16] P. Asoka-Kumar, K.G. Lynn, D.O. Welch, *J. Appl. Phys.* 76 (1994) 4935.
- [17] R. Krause-Rehberg, H.S. Leipner, *Positron Annihilation in Semiconductors*, Springer, Berlin, 1999.
- [18] P.J. Simpson, M. Vos, I.V. Mitchell, C. Wu, P.J. Schultz, *Phys. Rev. B* 44 (1991) 12180.
- [19] K.L. Merkle, P.P. Pronko, D.S. Gemmell, R.C. Mikkelsen, J.R. Wrobel, *Phys. Rev. B* 8 (1973) 1002.
- [20] S.T. Picraux, D.M. Follstaedt, P. Baeri, S.U. Campisano, G. Foti, E. Rimini, *Radiat. Effects* 49 (1980) 75.
- [21] D.B. Williams, C.B. Carter, *Transmission Electron Microscopy*, 2nd ed., Springer US, 2009.
- [22] OCI Vacuum Microengineering Inc.. <http://www.ocivm.com/> (accessed 6 December 2021).
- [23] SIMNRA - Computer simulation of RBS, ERDA, NRA, MEIS and PIGE by Matej Mayer. <https://home.mpcdf.mpg.de/~mam/index.html> (accessed 6 December 2021).
- [24] G. C. Aers, in *Positron Beams for Solids and Surfaces* edited by P.J. Schultz, G. Mas-soumi, P.J. Simpson, AIP, New York, 1990.
- [25] K. Terakura, T. Yamasaki, Y. Morikawa, *Phase Transitions* 53 (1995) 143.
- [26] L.V. Arapkina, V.A. Yuryev, K.V. Chizh, V.M. Shevlyuga, M.S. Storojevyh, L.A. Krylova, L.A. Krylova, *Nanoscale Research Letters* 6 (2011) 218.
- [27] A. Ignatiev, F. Jona, *Surf. Sci.* 42 (1974) 605.
- [28] C.A. Meli, E.F. Greene, *J. Chem. Phys.* 101 (1994) 7139.
- [29] A. Dygo, T.P.J.M. Smulders, D.O. Boerma, *Nucl. Inst. Meth. Phys. Res. B* 64 (1992) 701.
- [30] M. Henini, *Molecular Beam Epitaxy*, 2nd ed., Elsevier, 2018.
- [31] Y. Wang, M. Nastasi, *Handbook of Modern Ion Beam Materials Analysis*, Materials Research Society, 2009.
- [32] N. Takagi, S. Shimonaka, T. Aruga, M. Nishijima, *Phys. Rev. B* 60 (1999) 10919.
- [33] W.-W. Zhang, H. Yu, S.-Y. Lei, Q.-A. Huang, *J. Phys. D: Appl. Phys.* 44 (2011) 335401.

- [34] P. Kruse, M. Schowalter, D. Lamoen, A. Rosenauer, D. Gerthsen, *Ultramicroscopy* 106 (2006) 105.

# Chapter 4

## Light emission from SiGe quantum structures in SiO<sub>2</sub> produced by Si and Ge co-implantation

### 4.1 Introduction

Silicon has been the dominant semiconductor material in the electronic industry due to its low defect concentration at the interface with silicon oxide and its versatility in terms of acceptable dopants and doping levels. However, Si is an indirect bandgap semiconductor and lacks efficient light emission. The focus of numerous publications has been on Si quantum structures (Si-QSs) and their potential applications in Si-based optoelectronic devices using the quantum confinement effect [1, 2, 3]. These investigations have consistently observed a shift of the photoluminescence (PL) peak to higher energy as the size of the QS decreases, particularly from the near-infrared (NIR) to the visible region. The optical properties of quantum structures formed through ion implantation exhibit significant variability due to the wide range of experimental parameters available for the formation of quantum dots (QDs). Factors like the concentration of defects at the interface, the amount of stress, and dielectric effects from the matrix material will vary depending on fabrication parameters [4]. Another distinction in the properties of QDs arises from their degree of crystallinity: amorphous QDs exhibit strong quantum confinement effects, as evidenced by measurements of confinement constants [5] and lifetimes [6].



Studies have demonstrated that Si-QDs exhibit a limited wavelength peak emission window determined by the Bohr radius, ranging from approximately 500 nm [7] to 1000 nm [4]. Once the diameter of the QD increases beyond 4.5 nm (Si Bohr radius), the quantum confinement progressively weakens. A possible alternative to extend the emitted wavelengths is making a compound QD, for instance SiC or SiGe. SiGe quantum structures allow tuning of the optical properties, since the electronic band structure of the  $\text{Si}_{1-x}\text{Ge}_x$  alloy depends on  $x$ .

The literature regarding  $\text{Si}_{1-x}\text{Ge}_x$  QDs formed by ion implantation into insulating matrices like silicon dioxide is not extensive. Most of the relevant publications are reviewed in Chapter 1, section 1.2, and a brief summary is provided here. To the best of our knowledge, the first work about this particular system was published by Zhu et al. in 1995 [8]. In that work,  $\text{Si}^+$  and  $\text{Ge}^+$  were implanted into amorphous  $\text{SiO}_2$  with energy and fluences of 215 keV,  $3 \times 10^{17} \text{ cm}^{-2}$  and 500 keV,  $3 \times 10^{17} \text{ cm}^{-2}$ , respectively. Then, the samples were annealed at 1000 °C or at 1100 °C for 1 h in Ar with 5%  $\text{H}_2$ . Formation of spherical precipitates with maximum diameter of 15 nm was observed by transmission electron microscopy (TEM) after annealing to 1000 °C. On the other hand, annealing to nearly the melting temperature of 1100 °C showed particles with dimensions greater than 100 nm and some coalesced particles. In both cases, x-ray diffraction (XRD) showed formation of SiGe crystals.

A different technique to produce  $\text{Si}_{1-x}\text{Ge}_x$  QSS was used by Takeoka et al. [9]. Silicon dioxide films containing  $\text{Si}_{1-x}\text{Ge}_x$  nanocrystals were deposited using RF sputtering with three targets simultaneously ( $\text{SiO}_2$ , Si, and Ge). After deposition, samples were annealed in  $\text{N}_2$  gas at a 1100 °C. Different compositions were produced by varying the deposition rates independently. High-resolution transmission electron microscopy (HRTEM) showed the growth of spherical nanocrystals with an average diameter of 4.6 nm in an amorphous  $\text{SiO}_2$  matrix. Raman spectroscopy showed three peaks for the samples containing Ge, in accord with the spectrum of bulk  $\text{Si}_{1-x}\text{Ge}_x$  alloy crystals previously published [10]. Takeoka et al. also studied photoluminescence at room temperature, and showed that the PL peak shifted to lower energies as Ge content increased [11]. PL measurements also revealed that intensity decreased as Ge content increased. The author states one of the reasons is the diameter increment for higher Ge concentrations, since the size of nanocrystals is close to the Bohr radius. Another reason is the density of defects associated with  $\text{Si}_{1-x}\text{Ge}_x$  nanocrystals and the  $\text{SiO}_2$  interface, which

may increase with higher Ge content. Takeoda also studied PL transients and found that the lifetime for all samples was on the order of a microsecond, and became shorter with increasing germanium concentration.

Mogaddam et al. have also used the co-sputtering of three targets simultaneously (SiO<sub>2</sub>, Si, and Ge) [12]. The typical thickness of deposited films was about 350 nm. The deposition parameters were fixed to study the effect of annealing time on the local structure of the samples, which were thermally annealed at 1100 °C in N<sub>2</sub> gas and at ambient pressure, for 1, 3, or 5 h. A decomposition tendency of the SiGe related peaks in XRD and Raman measurements in the samples annealed for longer times was observed. The author has also compared TEM imaging for samples annealed for 1 and 3 h. In this case, there were mixtures of nanocrystals of many sizes within the co-sputtered layer for both samples. This large variation can be understood by the Ostwald ripening process where large nanocrystals grow at the expense of the smaller ones. However, the size distribution comparison of these two samples indicates that for the sample annealed for 3 h, the number of nanocrystals with sizes smaller than 10 nm is about three times that of the sample annealed for 1 h. In addition, large nanocrystals with sizes of approximately 150 nm were formed accompanied by a significant decrease in the number of nanocrystals having a moderate size of 50 nm.

In a more recent paper [13], Zhong et al. formed SiGe nanocrystals in SiO<sub>2</sub> films using consecutive implantation of Si<sup>+</sup> and Ge<sup>+</sup> ions with energies of 36 keV and 70 keV, respectively. The mean projected range of both ions was about 50 nm, without consideration of the sputtering effect. Formation of SiGe alloy was confirmed by XRD. The author also identified nanocrystals in the silicon oxide matrix using HRTEM, with diameters between 3 and 4 nm. The paper also presents the results of PL measurements and time-resolved PL. These results will be discussed further in the following sections.

This work focuses on Si and Ge ion implantation to produce Si<sub>1-x</sub>Ge<sub>x</sub> QSS within an amorphous SiO<sub>2</sub> matrix, with varying Ge content, and places particular emphasis on the effect of thermal annealing sequence on the optical and structural properties of these quantum structures. Moreover, we aim to understand the behaviour of luminescence properties as a function of SiGe QD preparation. We employed steady-state and time-resolved photoluminescence to understand how the wavelength and the lifetimes of the QSS are dependent on fabrication

steps. Raman spectroscopy was employed to provide insight into the structural properties of the  $\text{Si}_{1-x}\text{Ge}_x$  QSS, and RBS was used to investigate the depth profile of the implanted ions. By integrating these experimental approaches, we aim to contribute to the advancement of optoelectronic materials and devices.

## 4.2 Experimental details

In order to synthesize SiGe QDs, thermally grown  $1\ \mu\text{m}$   $\text{SiO}_2$  on a p-type silicon (100) substrate was implanted with Si and Ge ions at the Western University Tandetron Accelerator Facility. First, Si implants were performed at room temperature with  $8.05 \times 10^{16}$  ions/ $\text{cm}^2$  dose at 40 keV for all samples. The projected range calculated with SRIM (Stopping and Range of Ions in Matter) software [14, 15], with sputtering correction, was 40 nm. After Si implantation, the samples were divided into two groups: the first group, referred to as SiAGeXA, was annealed in an  $\text{N}_2$  atmosphere for 1 h at  $1100^\circ\text{C}$  and then implanted with Ge. The second group, referred to as SiGeXAA, did not undergo annealing between the Si and Ge implants. However, the same thermal annealing was done after Si and Ge implants. Later, both sets were annealed at  $900^\circ\text{C}$  for 30 min in  $\text{N}_2$  atmosphere to incorporate Ge into the quantum structures. Finally, all samples were subjected to forming gas annealing for interface passivation at  $500^\circ\text{C}$  for 30 min. Figure 4.1 shows the sequence of sample preparation.

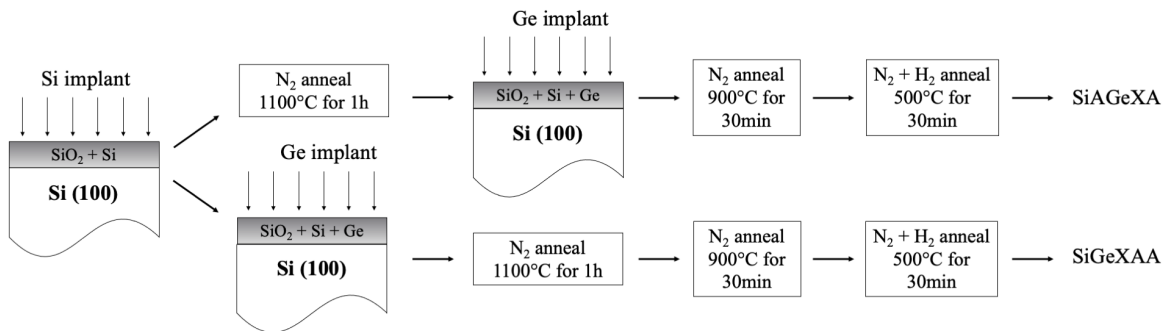


Figure 4.1: Process flow illustrating the sample preparation in this work. Si was implanted with  $8.05 \times 10^{16}$  ions/ $\text{cm}^2$  at 40 keV. Ge implanted doses varied from  $1.30 \times 10^{15}$  to  $2.10 \times 10^{16}$  ions/ $\text{cm}^2$ , at 55 keV. The diagram also includes the nomenclature for each sample set, where “X” stands for Ge concentration. “A” stands for anneal.

Germanium implantation energy was chosen to be 55 keV in order to overlap with the Si

implanted profile. Ge implanted doses were 0.5 at.%, 1.0 at.%, and 2.0 at.% for the first sample set, and the second set had two additional samples corresponding to Ge doses of 4.0 at.% and 7.5 at.%. Table 4.1 presents the implanted doses, as well as the sample nomenclature that will be used. A reference sample was prepared with only Si implantation at 40 keV with  $8.05 \times 10^{16}$

	Sample name	Ge peak at. %	Dose (ions/cm <sup>2</sup> )
Reference sample	Si_1100C_FG	0	0
Sample set SiAGeXA	SiAGe0.5A	0.5	$1.30 \times 10^{15}$
	SiAGe1.0A	1.0	$2.61 \times 10^{15}$
	SiAGe2.0A	2.0	$5.28 \times 10^{15}$
Sample set SiGeXAA	SiGe0.5AA	0.5	$1.30 \times 10^{15}$
	SiGe1.0AA	1.0	$2.61 \times 10^{15}$
	SiGe2.0AA	2.0	$5.28 \times 10^{15}$
	SiGe4.0AA	4.0	$1.08 \times 10^{16}$
	SiGe7.5AA	7.5	$2.10 \times 10^{16}$

Table 4.1: Ge implanted dose for each sample in this work. The sample nomenclature is also presented, being labeled chronologically.

ions/cm<sup>2</sup> dose, annealing in N<sub>2</sub> for 1 h at 1100 °C, and forming gas.

Rutherford backscattering spectroscopy (RBS) was applied to probe elemental depth profiles in random geometry in selected samples. The measurements were carried out at the Western University Tandatron Accelerator Facility, using a monoenergetic beam of He<sup>+</sup> at 500 keV with a Si charged particle detector positioned at a scattering angle of 170°. An Sb-implanted Si standard ( $4.72 \times 10^{15}$  Sb atoms/cm<sup>2</sup>) was used to calibrate the solid angle of the detector and its channel-to-energy conversion coefficient. The uncertainty of ion yields obtained by RBS measurements derived from this process is close to 3.5%. RBS spectra were fitted using MEISwin software [16] to determine the implanted depth profiles.

Photoluminescence measurements were performed with a Horiba Fluorolog-QM spectrofluorometer equipped with a 75 W xenon arc lamp and two photo detectors: a Hamamatsu R928 photomultiplier tube for the 300 – 900 nm range and a DSS-IGA020 InGaAs solid-state detector for the NIR range (850 to 1700 nm). Samples were excited at 270 nm, and a long-pass filter ( $\lambda_c = 320 \pm 6$  nm) was employed to remove any reflected light from the excitation source. All spectra presented in this work were corrected to consider grating and detector efficiencies. Time-resolved photoluminescence (TRPL) decays were acquired using a pulsed LED with ex-

citation wavelength of  $370 \pm 10$  nm and were detected with the PMT detector. Both PL and TRPL were performed with the excitation beam making an angle of  $65^\circ$  with respect to the sample normal, at room temperature.

Raman measurements were performed at Western University using a custom-built system. An argon-ion laser with a wavelength of 514.5 nm was used as an excitation source. The Raman spectra were collected by a spectrometer with a 500 mm focal length and equipped with a liquid nitrogen-cooled CCD detector. The spectrometer was calibrated using a neon lamp and a silicon substrate. The uncertainty in Raman shift measurements is in the range of 1 to  $2 \text{ cm}^{-1}$ .

### 4.3 Results and discussion

Figure 4.2 shows PL spectra in the visible range at room temperature for sample sets SiAGeXA (Figure 4.2a) and SiGeXAA (Figure 4.2b). The reference sample Si\_1100C\_FG (Si implant

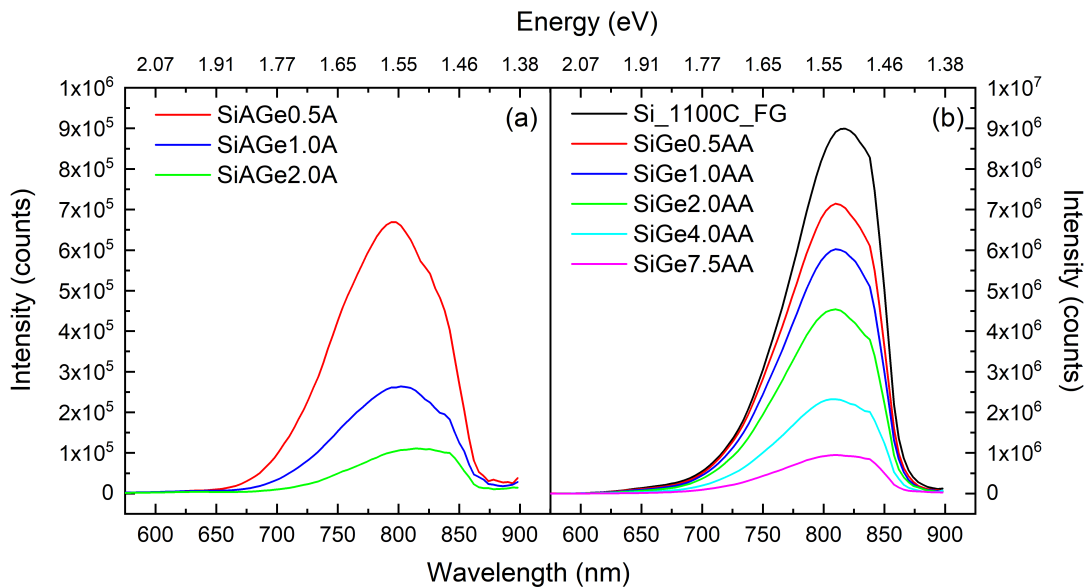


Figure 4.2: PL spectra in the UV-Vis range of (a) sample set SiAGeXA (thermal annealing between Si and Ge implants) and (b) reference sample plus sample set SiGeXAA (thermal annealing after Si and Ge implants).

only, as described in the experimental section), is also shown in Figure 4.2b for comparison. Emission from oxygen vacancy defects associated with the  $\text{SiO}_2$  matrix was observed at

about 400 nm [17]. It is not included in Figure 4.2 because, after the detector efficiency and grating corrections, its intensity becomes more than 100 times smaller compared to the emission around 800 nm. For both sample sets, it is observed that the PL intensity decreases as the concentration of germanium increases. When comparing the preparation method, samples with thermal annealing after Si and Ge implants (sample set SiGeXAA), have more than 10 times the emission intensity for the same Ge concentration. For instance, the peak intensity of SiAGe0.5A is about  $7 \times 10^5$ , while SiGe0.5AA is  $7 \times 10^6$ .

The PL emission in the NIR range (850 - 1700 nm) was also studied using the same excitation source and wavelength (270 nm), and is presented in Figure 4.3. Only emissions up

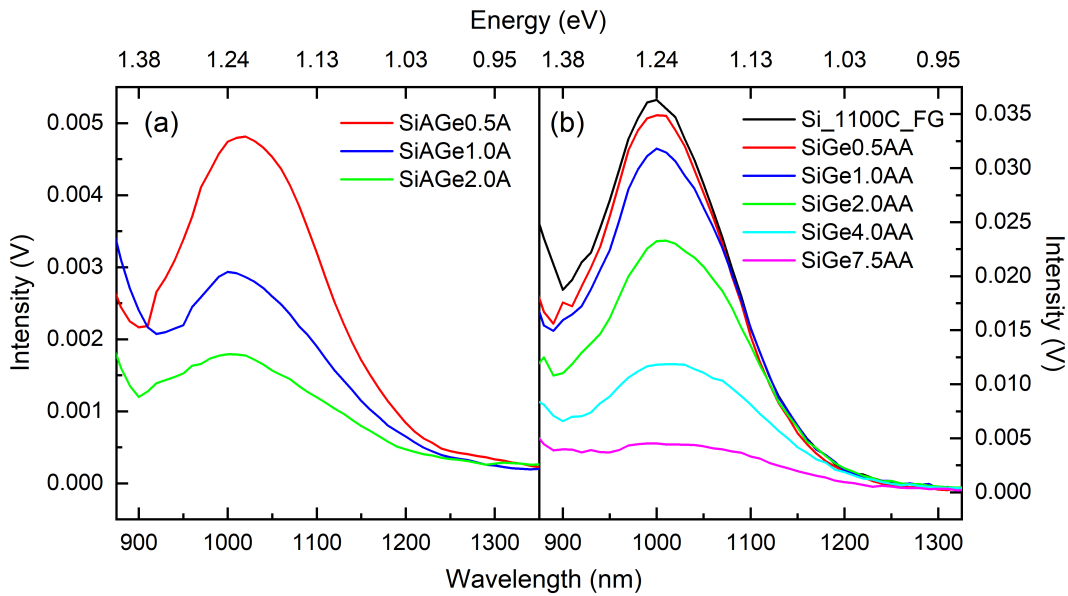


Figure 4.3: PL spectra in the NIR range of (a) sample set SiAGeXA and (b) reference sample plus sample set SiGeXAA. Note different intensity scales.

to 1350 nm are displayed since no signal was detected above this wavelength. Both sample sets behave similarly in relation to the PL intensity: the higher the Ge concentration, the less intensity is observed. When comparing the same Ge amount, sample set SiGeXAA has higher PL emission intensity. The reference sample Si\_1100C\_FG is also shown in Figure 4.3b for comparison.

While comparing the PL results from both detectors presented in Figure 4.2 and Figure 4.3, one can ask whether the peak being measured is the same, i.e. whether the peak observed around 1000 nm is an extension of the one observed around 800 nm. In an effort to clarify

the presence of one or two emission peaks, the reference sample Si\_1100C.FG was sent to the PL equipment manufacturer (Horiba) to be analyzed with a wide range detector (Hamamatsu R5509-73 photomultiplier tube, with spectral response from 300 to 1700 nm). Figure 4.4 shows the data corresponding to the reference sample being measured with this detector, demonstrating two separated peaks with the same wavelength (800 nm and 1000 nm) as measured with our detectors. The spectrum has been corrected to account for detector and grating efficiencies.

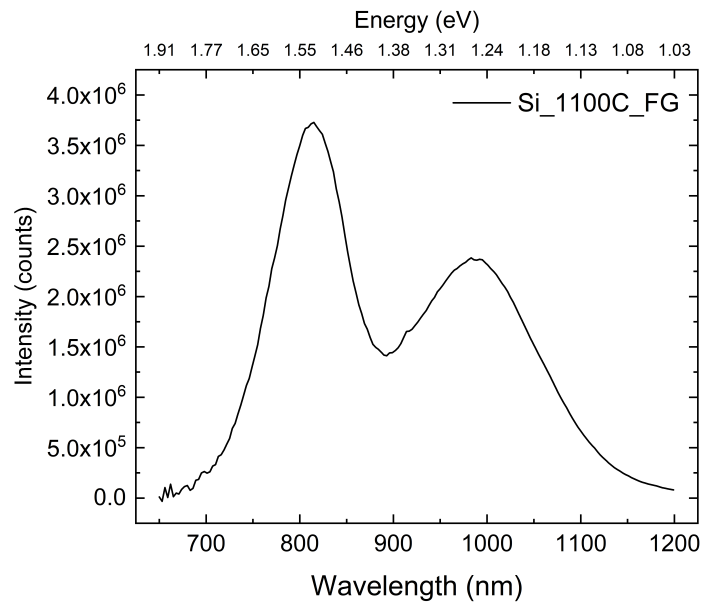


Figure 4.4: Emission spectrum of the reference sample excited with 270 nm and measured with the PMT R5509-73.

To the best of our knowledge, this is the first time two PL peaks were measured for Si and SiGe QDs, as we used two detectors covering visible and NIR spectral ranges. The reason why we have two emission peaks relies on the intrinsic characteristics of the ion implantation process. It is widely accepted that, as an initial approximation, the distribution of implanted ions can be described by a nearly Gaussian profile with a known ion range and straggle. However, there is evidence suggesting that the implanted ion distribution rarely adheres to a Gaussian shape [18]. The deviation from Gaussian behaviour depends on several factors, including the ion species, the composition of the target material, the temperature during implantation, the implantation energy, and subsequent processing steps. These factors collectively contribute to

the generation of diverse profiles, departing from the expected Gaussian distribution. There are reports in the literature of the formation of non-Gaussian distributions of sizes in quantum structures produced by ion implantation [19] and even a bimodal size distribution [20]. More recently, a nucleation and evolution model of damage was developed and implemented in an atomistic kinetic Monte Carlo simulator showing a bimodal distribution of damage caused by ion bombardment [21] for implantations of 100 keV at room temperature. According to Mok et al., different damage morphologies have distinct thermal instabilities, leading to different annealing behaviour.

In an effort to investigate the origin of the two peaks in Figure 4.4, Figure 4.5 presents the simulated Si depth profile derived from RBS measurements conducted on sample Si\_1100C\_FG before and after annealing at 1100 °C. The changes in the Si distribution due to this annealing

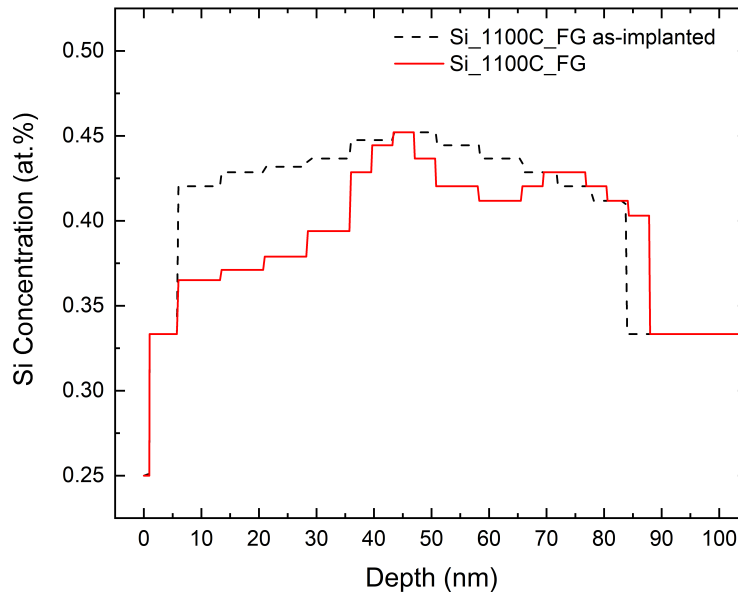


Figure 4.5: Simulated depth profiles from RBS measurements of sample Si\_1100C\_FG before and after annealing.

process are apparent. While we cannot definitively characterize the Si distribution after annealing as bimodal, we can affirm that it does not follow a Gaussian distribution. Therefore, considering the high-concentration regions around 50 nm and 80 nm, along with supporting evidence from the literature, we infer that the dual peak observed in Figure 4.4 may be at-



tributed to the presence of a quasi-bimodal distribution in the size of the quantum structures formed. Selected samples are being analyzed by transmission electron microscopy (TEM) and the results may confirm, or not, the bimodal size distribution. Another hypothesis for the PL behaviour observed in Figure 4.4 is the emission from the first two excited states  $E_1 = 1.24$  eV and  $E_2 = 1.58$  eV, calculated using equation (3) described by Barbagiovanni et al. in [4], providing a theoretical energy difference of 0.34 eV. As the measured energy difference between the two peaks is 0.28 eV, this hypothesis seems reasonable, but difficult to verify.

Continuing from our discussion of Figure 4.4, the position of the PL maximum of the UV-Vis peak is 818 nm, and the peak in the NIR is 1002 nm. They present FWHM of 80 and 130 nm, respectively. Considering the interval of wavelengths defined by FWHM, the UV-Vis peak spans from 778 to 858 nm, and the NIR peak spans from 937 to 1067 nm. Based on that and using the approach of the effective mass approximation that provides  $E_g(D) = E_g(\infty) + A/D^2$  [5], we estimate their diameters over the interval  $D_{UV-Vis} = [1.7; 2.1]$  nm and  $D_{NIR} = [2.6; 5.7]$  nm, where  $E_g(\infty) = 1.12$  eV and  $A = 1.39$  eV · nm<sup>2</sup>.

In order to study how the peak emission is influenced by Ge concentration, the wavelength of maximum emission ( $\lambda_{max}$ ) was obtained by fitting a Gaussian curve with FWHM at the peak region for both UV-Vis and NIR spectra. Figure 4.6 shows positions of PL peak maximum, both in the UV-Vis and NIR, as a function of Ge concentration and annealing sequence, and Table 4.2 summarizes them.

Sample	$\lambda_{max,UV-Vis}$ (nm)	$\lambda_{max,NIR}$ (nm)
<b>Si_1100C_FG</b>	818.1 ± 0.3	1001.6 ± 0.6
<b>SiAGe0.5A</b>	795.1 ± 0.1	1021.3 ± 0.5
<b>SiAGe1.0A</b>	800.3 ± 0.2	1011.2 ± 0.9
<b>SiAGe2.0A</b>	815.3 ± 0.5	1002.1 ± 0.8
<b>SiGe0.5AA</b>	811.8 ± 0.2	1003.4 ± 0.6
<b>SiGe1.0AA</b>	811.8 ± 0.1	1007.6 ± 0.8
<b>SiGe2.0AA</b>	809.8 ± 0.3	1014.0 ± 1.0
<b>SiGe4.0AA</b>	810.9 ± 0.4	1016.2 ± 0.9
<b>SiGe7.5AA</b>	812.0 ± 0.4	1010.9 ± 2.5

Table 4.2: Peak emission wavelength ( $\lambda_{max}$ ) obtained from PL spectra in the UV-Vis and NIR ranges.

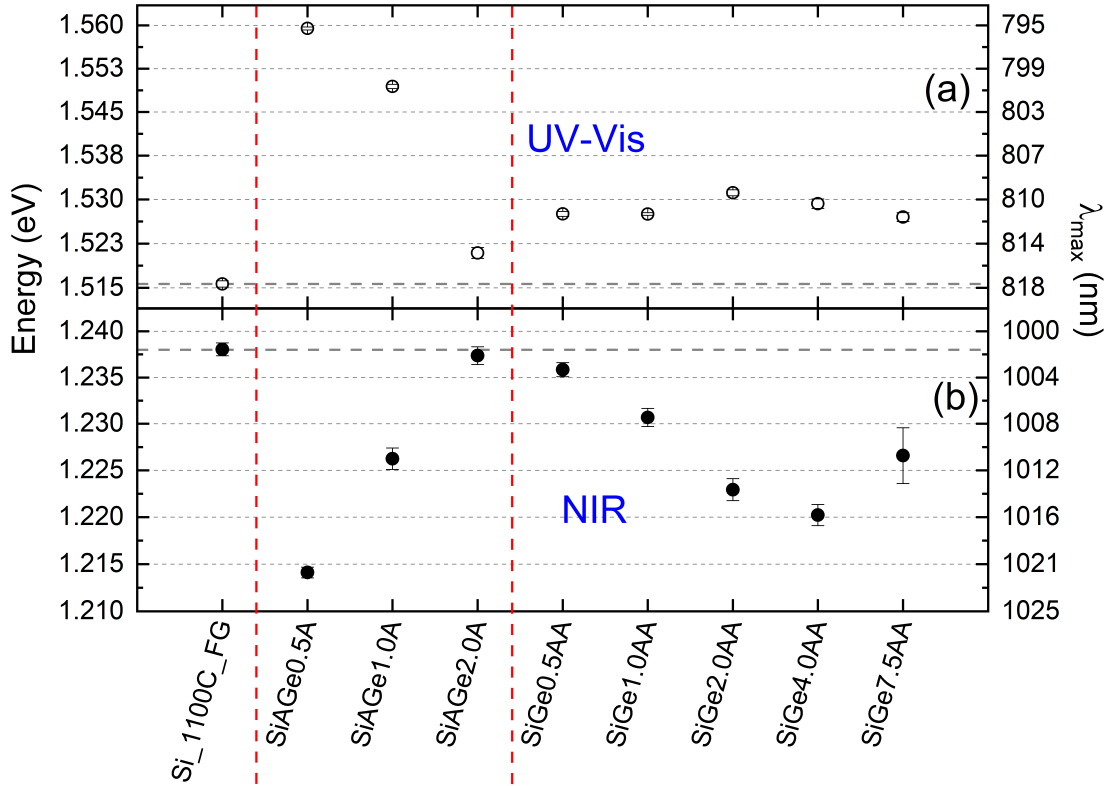


Figure 4.6: Wavelength of maximum emission,  $\lambda_{\max}$ , plotted for all samples. (a) data obtained from UV-Vis emission and (b) from NIR emission. The red dashed line separates the different sample sets.

Figure 4.6a shows how  $\lambda_{\max,UV-Vis}$  varies for each sample. We observe a shift towards lower wavelengths for both sets of samples when Ge is added. For sample SiAGe0.5A,  $\lambda_{\max,UV-Vis}$  is shifted by 23 nm (18.5 meV), while SiGe0.5AA is only shifted by 6.3 nm (5 meV). In other words, after Ge addition, sample set SiAGeXA has a significant  $\lambda_{\max,UV-Vis}$  change to higher wavelengths, although  $\lambda_{\max,UV-Vis}$  of the sample set SiGeXAA remains about the same. Thus, the light emission in the UV-Vis range has a strong dependence on the annealing order.

As we examine the wavelength of maximum emission in the NIR range in Figure 4.6b, the sample set SiAGeXA shows  $\lambda_{\max,NIR}$  increasing for 0.5 at.% and then returning to about the same  $\lambda_{\max,NIR}$  as the reference sample when the amount of Ge equals 2.0 at.%. This behaviour is the opposite of what is seen in the UV-Vis range. It is important to remember that the Ge implant in this sample set was made after post-annealing of the Si implant. It is likely that part of the Ge ions cannot be incorporated into the pre-existing Si quantum structure even after the

second annealing. Therefore, if we look at the emission in both ranges as a wide band, we can interpret it as the broadening of the emission band due to defects that were introduced by Ge implantation or by Ge segregation at the Si QSS interface [22]. As the implantation dose increases, these defects quench the emission and cause  $\lambda_{\max}$  to return to the value of the pure Si sample. However, that does not happen in sample set SiGeXAA, where  $\lambda_{\max,UV-Vis}$  remains approximately constant, while  $\lambda_{\max,NIR}$  increases consistently with increasing Ge concentration. A possible reason for this may be that the annealing occurs after the two implants, which may allow Ge to be incorporated into Si QSS, forming compound SiGe quantum dots.

To gain a better understanding of the effect of the annealing order on the luminescence properties, RBS was conducted on samples SiAGe2.0A and SiGe2.0AA. Figure 4.7a displays the RBS spectra, while Figure 4.7b illustrates the calculated Ge depth profiles from these spectra. Total germanium concentration in the sample SiAGe2.0A was measured to be  $5.36 \times 10^{15} \text{ cm}^{-2}$ ,

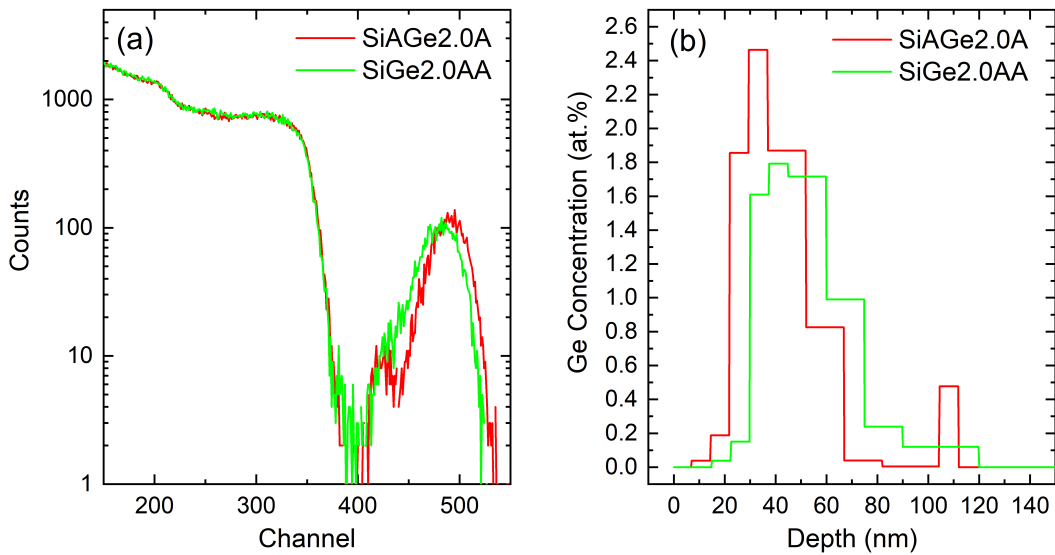


Figure 4.7: (a) RBS results of samples SiAGe2.0A and SiGe2.0AA. (b) Simulated depth profile of these measurements using MEISwin software [16].

which is 1.5% higher than the implanted dose but within RBS experimental uncertainty, and no Ge loss was detected during high-temperature anneals. On the other hand, the Ge content in sample SiGe2.0AA was found to be  $4.69 \times 10^{15} \text{ cm}^{-2}$  (11% lower than the implanted dose), revealing that some Ge was lost during the anneals. We can attribute this difference to the higher diffusivity of Ge, which is a result of the greater number of vacancies present in sample

SiGe2.0AA during the first annealing. It is likely that Ge is lost due to GeO desorption at these temperatures [23]. In fact, Figure 4.7b shows distinct Ge depth profiles between these samples, with a lower Ge concentration observed near the surface in sample SiGe2.0AA. Overall, the RBS results support our hypothesis that Ge incorporates more into the QSS in the SiGeXAA set. This is evidenced by a higher redshift in  $\lambda_{\max, \text{NIR}}$ , even though a lower concentration was found in sample SiGe2.0AA.

Photoluminescence was also applied in the time domain (time-resolved photoluminescence) to study the emission dynamics of our samples. Samples were excited by a pulsed LED with a wavelength of  $370 \pm 10$  nm. Figure 4.8a shows the decay spectra of all samples. A

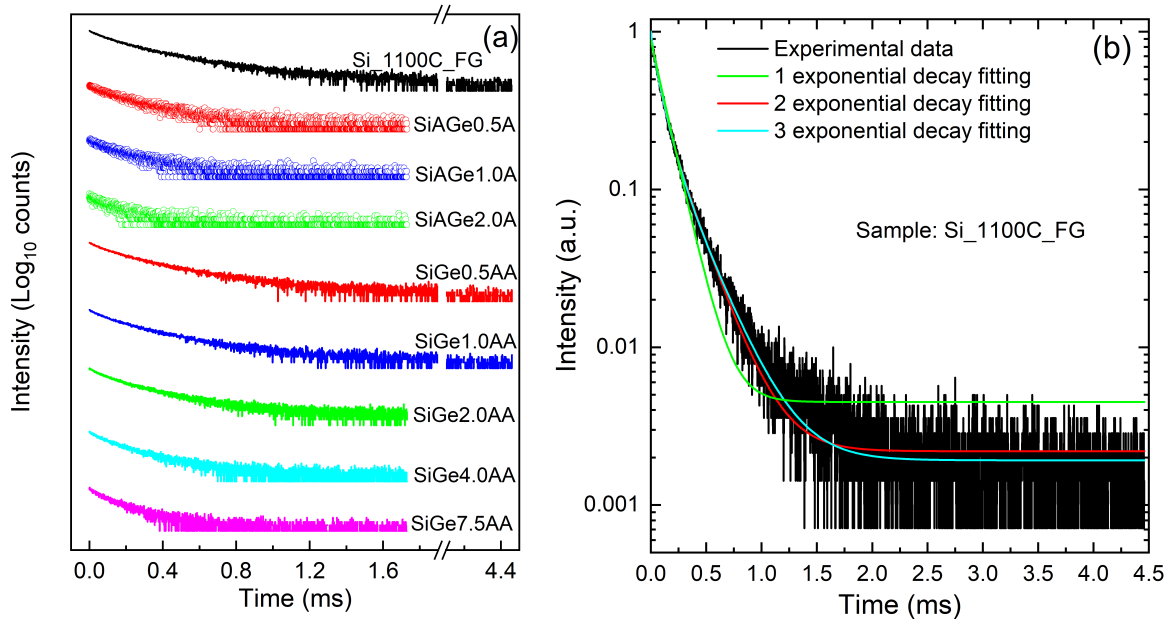


Figure 4.8: (a) Time-resolved photoluminescence decays measured at room temperature using a pulsed LED with wavelength of  $370 \pm 10$  nm. (b) TRPL experimental data from the reference sample fitted with different exponential decays.

1 ms pulse width was kept constant during all the measurements, while the observation window was either 1.7 ms or 4.5 ms. The selection of 1.7 ms or 4.5 ms windows was done considering the signal level of each sample, at the end of the window, to be at least 1000 times smaller than its initial value. The data was acquired for 600 s, resulting in a uniform background noise for all the measurements. After the time-resolved data acquisition, the curves were individually normalized and fitted with the two exponential decay curve  $y = y_0 + A_1 e^{-t/t_1} + A_2 e^{-t/t_2}$ , where  $y_0$  is an offset related to the background noise, and  $A_1$  and  $A_2$  are the weights of lifetimes  $t_1$  and  $t_2$ ,

respectively. Figure 4.8b shows the fitting for the reference sample to illustrate its quality using two exponential decays. A single exponential curve fit is not appropriate in this case because the experimental decay has two slopes in the log scale (one up to 0.5 ms and another after 0.5 ms, approximately), as shown in Figure 4.8b. The parameters obtained from the fitting of all measurements are summarized in Table 4.3.

Sample	$y_0$	$A_1$	$t_1$ ( $\mu\text{s}$ )	$A_2$	$t_2$ ( $\mu\text{s}$ )
<b>Si_1100C.FG</b>	$0.0022 \pm 0.0001$	$0.532 \pm 0.009$	$70 \pm 1$	$0.424 \pm 0.008$	$220 \pm 2$
<b>SiAGe0.5A</b>	$0.0070 \pm 0.0005$	$0.370 \pm 0.020$	$56 \pm 4$	$0.540 \pm 0.020$	$182 \pm 5$
<b>SiAGe1.0A</b>	$0.0084 \pm 0.0008$	$0.410 \pm 0.030$	$57 \pm 4$	$0.430 \pm 0.030$	$191 \pm 8$
<b>SiAGe2.0A</b>	$0.0140 \pm 0.0010$	$0.350 \pm 0.040$	$51 \pm 7$	$0.350 \pm 0.050$	$170 \pm 10$
<b>SiGe0.5AA</b>	$0.0025 \pm 0.0001$	$0.507 \pm 0.008$	$63 \pm 1$	$0.467 \pm 0.009$	$209 \pm 2$
<b>SiGe1.0AA</b>	$0.0023 \pm 0.0001$	$0.526 \pm 0.008$	$61 \pm 1$	$0.430 \pm 0.008$	$204 \pm 2$
<b>SiGe2.0AA</b>	$0.0059 \pm 0.0002$	$0.457 \pm 0.009$	$50 \pm 1$	$0.490 \pm 0.010$	$174 \pm 2$
<b>SiGe4.0AA</b>	$0.0064 \pm 0.0003$	$0.430 \pm 0.010$	$45 \pm 2$	$0.510 \pm 0.020$	$155 \pm 3$
<b>SiGe7.5AA</b>	$0.0069 \pm 0.0004$	$0.410 \pm 0.020$	$42 \pm 2$	$0.450 \pm 0.030$	$137 \pm 4$

Table 4.3: Parameters obtained from double exponential fit ( $y = y_0 + A_1 e^{-t/t_1} + A_2 e^{-t/t_2}$ ) of time-resolved photoluminescence decays.

All samples could be well fitted with a two exponential decay ( $R^2 = 0.997$ ), and each lifetime has about the same contribution. Better data would be necessary in order to meaningfully compare the fit using two and three exponentials. Another possibility would be a stretched exponential  $y = A \exp(-t/\tau)^\beta$ . However, Jayatilleka et al. [24] made an extensive study of TRPL from Si nanocrystals produced by ion implantation in  $\text{SiO}_2$  indicating that three exponential decay components provided a better fit (smaller  $\chi^2$ ) than the stretched exponential. The physical argument was based on the presence of three distinct classes of nanocrystals whose photoluminescence behaviour is a consequence of their size in relation to other nanocrystals, and luminescence-quenching defects. The three-exponential decay adopted by Jayatilleka et al. [24] resulted in the lifetimes of  $225 \mu\text{s}$ ,  $75 \mu\text{s}$ , and  $20 \mu\text{s}$ , with 0.22, 0.30, and 0.48 weights, respectively. Applying the same three-exponential decay fitting to our reference sample Si\_1100C.FG, we have  $257 \mu\text{s}$ ,  $90 \mu\text{s}$ , and  $9 \mu\text{s}$  lifetimes, with 0.30, 0.61, and 0.09 weights, respectively. Both sample sets present about the same lifetimes, although their weights are significantly different. This may be related to different size distribution of nanocrystals since their samples were made with a different ion dose and energy, and annealing process.

Returning to Table 4.3 and using the lifetimes extracted from the fitting, Figure 4.9 shows the average-weighted lifetime  $\bar{t}_w = (A_1 t_1 + A_2 t_2)/(A_1 + A_2)$ , calculated for each sample. It

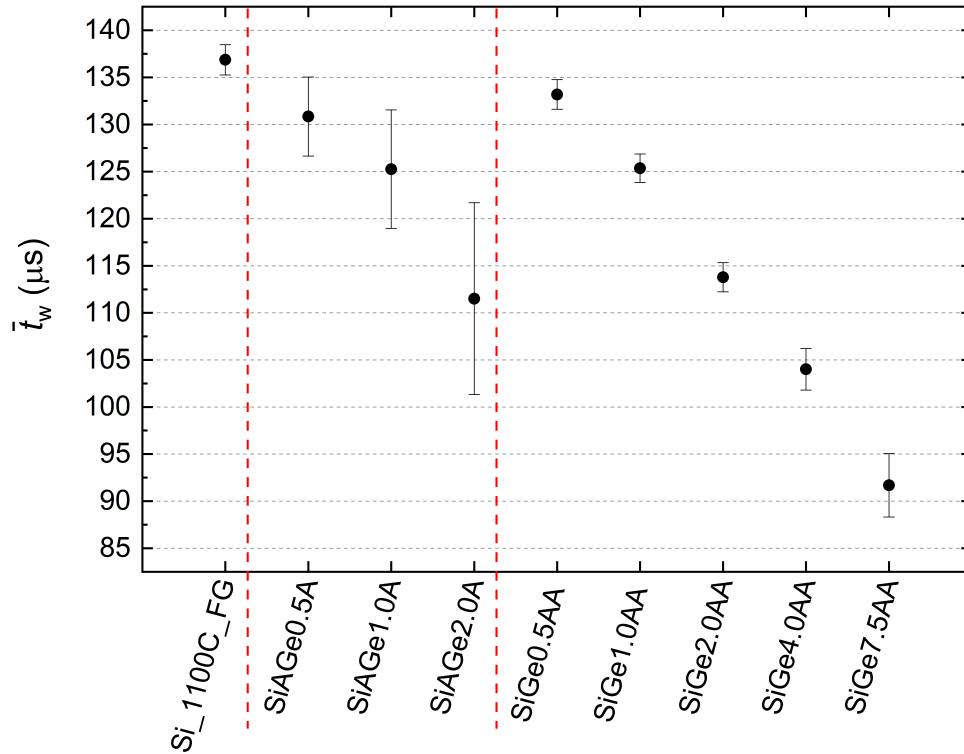


Figure 4.9: Weighted average lifetime  $\bar{t}_w = (A_1 t_1 + A_2 t_2)/(A_1 + A_2)$  for each sample, where  $A_1$  and  $A_2$  are the coefficients calculated from the exponential fitting.

can be observed that, in both set of samples,  $\bar{t}_w$  becomes shorter with increasing Ge concentration. When comparing the same concentration in different sets, we observe that sample set SiGeXAA presents higher lifetimes within the uncertainty, except when the Ge amount equals 2.0 at.%. Lifetime shortening is caused either by interface defects that increase nonradiative recombination or by an increase of the oscillator strength of the excitons. An increase of the oscillator strength means a larger overlap between hole and electron wave functions, which can be achieved by reducing the confinement region. This has been observed experimentally by Garcia et al. [25], who measured shorter lifetimes as the Si QDs diameter decreased. SiGe alloying is another way to increase the oscillator strength and has been reported by Delerue et al.[26]. Considering the fabrication method employed in the different sample sets, we can say the lifetime shortening in the sample SiAGeXA is likely due to defects from the different sam-

ple fabrication process. In the sample set SiGeXAA, this phenomenon may be more related to the oscillator strength increasing due to SiGe alloying.

Raman spectroscopy was employed to study the structural properties of the QDs, with results shown in Figure 4.10. In order to compare the presence and concentration of germanium,

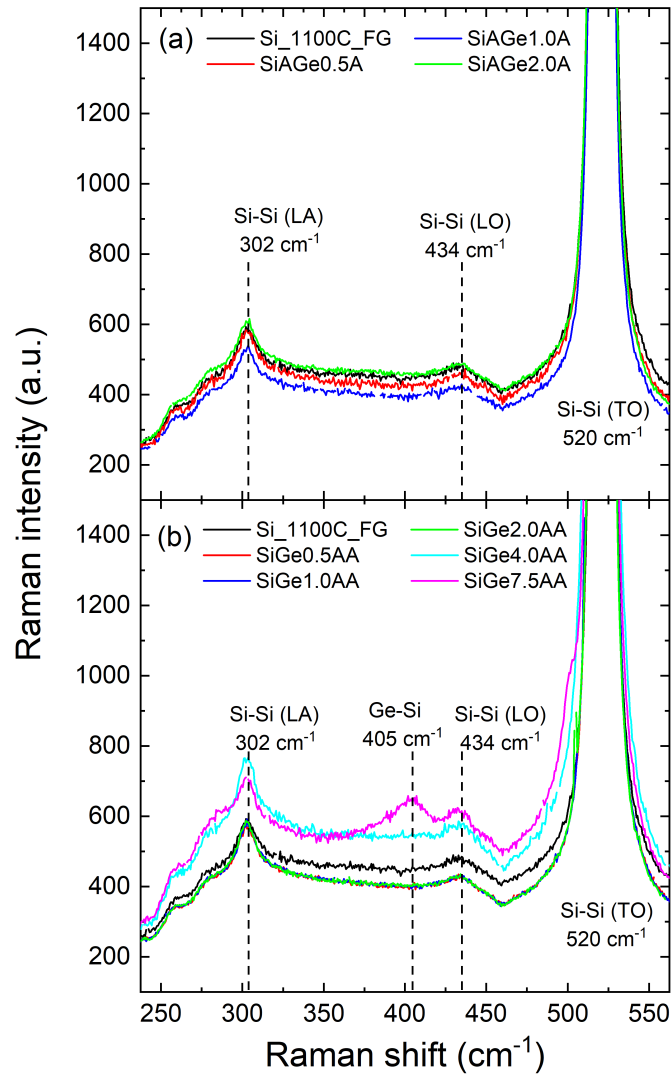


Figure 4.10: Raman spectra of (a) sample set SiAGeXA (b) sample set SiGeXAA, with the reference sample for comparison.

Figures 4.10a and 4.10b show the spectrum of the sample Si\_1100C\_FG (reference sample). Raman spectra show three vibrational modes in common for both sample sets. The first one, at  $302\text{ cm}^{-1}$ , corresponds to the longitudinal acoustic (LA) mode of the Si-Si bond. At  $434\text{ cm}^{-1}$  we have the longitudinal optical (LO) mode of the Si-Si bond, and at  $520\text{ cm}^{-1}$  the Si-Si trans-

verse optical (TO) vibrational mode appears. These three vibrational modes are well known for crystalline Si and they are typically attributed to the Si substrate [27]. Besides those modes, there is an additional peak that is exhibited only in the sample SiGe7.5AA at  $405\text{ cm}^{-1}$ . This peak is related to Si nanocrystals containing Ge impurities, and it has been identified experimentally [9, 13, 28] and predicted theoretically [29]. Its signal in the other samples of the same sample set is not detectable, probably due to the low concentration of Ge in these samples. On the other hand, the presence of Si-Ge bonding in the SiAGeXA sample set remains uncertain - the  $405\text{ cm}^{-1}$  peak is undetectable either due to the absence of bonded Ge in the QS, or due to the low concentration of Ge. The TO peak at  $520\text{ cm}^{-1}$  does not show any shift in either set of samples, likely because it is dominated by the substrate signal. Lastly, sample SiGe7.5AA presents a peak asymmetry adjacent to the  $520\text{ cm}^{-1}$  mode, which indicates that the system is under stress.

## 4.4 Conclusions

In this chapter, the effect of annealing steps sequence on the formation and luminescence properties of SiGe quantum structures was explored. In particular, we examined two sets of samples containing SiGe QSS through the implantation of Si at a constant dose while varying the Ge dose from 0.5 at.% to 7.5 at.%. The first set of samples was annealed between the Si and Ge implants, while the second set was annealed after both implants. Photoluminescence measurements revealed the presence of both visible and near-infrared bands for the QSS, indicating a wide range of particle sizes. Raman spectroscopy provided evidence of SiGe crystal formation for high Ge concentrations in samples annealed after both implants. Time-resolved photoluminescence measurements demonstrated the existence of two decay components, with shorter lifetimes associated with higher Ge content in both sets of samples. We found that successful SiGe QDs formation requires sequential implantation of Si and Ge followed by thermal annealing. An alternative annealing sequence, with intermediate anneals between Si and Ge implants, leads to formation of primarily Si QDs. Ge implantation increases defect concentration (which in turn decreases PL intensity) and a final anneal does not allow Ge atoms to incorporate into the Si QDs lattice, resulting in significantly lower PL intensity. Another possible explanation



for reduced PL intensity for higher Ge concentrations is the increased absorption of Ge. However, based on Raman results, there is no evidence of Ge-Ge bonds that could indicate the formation of Ge clusters leading to an enhanced absorption. Our TRPL results indicate two distinct time constants for pure Si QDs emissions ( $70\ \mu\text{s}$  and  $220\ \mu\text{s}$ , consistent with the literature) and show a significant decrease in the emission time constants as Ge content increases. These findings contribute to the understanding of SiGe-based materials and their potential applications in optoelectronic devices where light emission wavelength can be controlled by both Si to Ge ratio and QD diameter.

# References

- [1] G. T. Reed, Andrew P. Knights, *Silicon Photonics: An Introduction*, Wiley, 2004.
- [2] L. Pavesi, D. J. Lockwood, (Editors), *Silicon Photonics*, Springer, 2004.
- [3] G. T. Reed (Editor), *Silicon Photonics: the State of the Art*, Wiley, 2008.
- [4] E. G. Barbagiovanni, D. J. Lockwood, P. J. Simpson, and L. V. Goncharova, *Appl. Phys. Rev.* 1, 011302 (2014).
- [5] E. G. Barbagiovanni, D. J. Lockwood, P. J. Simpson, and L. V. Goncharova, *J. Appl. Phys.* 111, 034307 (2012).
- [6] Y. Kanemitsu, Y. Fukunishi, and T. Kushida, *Appl. Phys. Lett.* 77 (2), 211–213 (2000).
- [7] M. V. Wolkin, J. Jorne, P. M. Fauchet, G. Allan, and C. Delerue, *Phys. Rev. Lett.* 82, 197 (1999).
- [8] J. G. Zhu, C. W. White, J. D. Budai, S. P. Withrow, and Y. Chen, *J. Appl. Phys.* 78, 4386 (1995).
- [9] S. Takeoka, K. Toshiakiyo, M. Fujii, S. Hayashi, and K. Yamamoto, *Phys. Rev. B* 61 (23), 15988–15992 (2000).
- [10] M. I. Alonso and K. Winer, *Phys. Rev. B* 39, 10056 (1989).
- [11] H. Takagi, H. Ogawa, Y. Yamazaki, A. Ishizaki, and T. Nakagiri, *Appl. Phys. Lett.* 56, 2379 (1990).
- [12] N. A. P. Mogaddam, A. S. Alagoz, S. Yerci, R. Turan, S. Foss, and T. G. Finstad, *J. Appl. Phys.* 104, 124309 (2008).
- [13] K. Zhong, M. Lai, Y. Chen, and B. Gu, *Physica B* 407, 3660–3663 (2012).

- [14] J.F. Ziegler, J.P. Biersack, M.D. Ziegler, SRIM – The Stopping and Range of Ions in Matter, Ion Implantation Press, 2008
- [15] SRIM – The Stopping and Range of Ions in Matter. Accessed on February 15th, 2024. <http://www.srim.org>
- [16] T. Nishimura, Nuclear Instruments and Methods B 371 (2016).
- [17] M. Leone, S. Agnello, R. Boscaino, M. Cannas, and F. M. Gelardi, Phys. Rev. B 60 11475 (1999).
- [18] Ruge, I., Graul, J. (Editors). Ion Implantation in Semiconductors. Springer, Berlin, 1971.
- [19] J. P. Zhao, D. X. Huang, A. J. Jacobson, and J. W. Rabalais, Appl. Phys. Lett. 83, 3590 (2003).
- [20] Z. Liu, H. Wang, H. Li, and X. Wang, Appl. Phys. Lett. 72, 1823 (1998).
- [21] K. R. C. Mok, M. Jaraiz, I. Martin-Bragado, J. E. Rubio, P. Castrillo, R. Pinacho, M. P. Srinivasan, and F. Benistant, Mater. Sci. Eng. B 124–125, 389 (2005).
- [22] J. Weber and M. I. Alonso, Phys. Rev. B 40, 5683 (1989).
- [23] Y. Oniki, H. Koumo, Y. Iwazaki, and T. Ueno, Journal of Applied Physics 107, (2010).
- [24] H. Jayatilleka, D. Diamare, M. Wojdak, A. J. Kenyon, C. R. Mokry, P. J. Simpson, A. P. Knights, I. Crowe, and M. P. Halsall, J. Appl. Phys. 110, (2011).
- [25] C. Garcia, B. Garrido, P. Pellegrino, R. Ferre, J. A. Moreno, J. R. Morante, L. Pavesi, and M. Cazzanelli, Appl. Phys. Lett. 82, 1595 (2003).
- [26] C. Delerue, G. Allan, and M. Lannoo, J. Lumin. 80, 65 (1999).
- [27] P.H. Tan, K. Brunner, D. Bougeard, and G. Abstreiter, Phys. Rev. B 68 (12), (2003).
- [28] D. Barba, J. Demarche, F. Martin, G. Terwagne, and G.G. Ross, J. Appl. Phys. 114, 074306 (2013).
- [29] A.S. Vasin, O.V. Vikhrova, and M.I. Vasilevskiy, J. Appl. Phys. 115 (14), 143505 (2014).

# Chapter 5

## Light emission from SiGe quantum structures in SiO<sub>2</sub> produced by PECVD and Ge implantation

### 5.1 Introduction

The integration of optical emission properties with traditional microelectronics has been a long-standing challenge, primarily due to the limitations of silicon, the leading semiconductor in the microelectronic industry. Silicon indirect bandgap makes it a poor light emitter, therefore unsuitable for optoelectronic applications. Following the identification of light emission from porous Si [1], subsequent research in silicon photonics has concentrated on creating quantum structures (Qs), including quantum dots (QDs), and exploring their fundamental properties. This aims to improve optical emission from Si and facilitate its integration into Si chips [2, 3, 4, 5]. Silicon Qs can emit photons through exciton recombination within a restricted wavelength range (500 nm to 1000 nm) [6]. As the diameter of the QD exceeds the Bohr radius, the quantum confinement (QC) effect progressively weakens. A potential strategy for broadening the emitted wavelengths involves the creation of compound QDs, such as SiGe. SiGe quantum structures offer a viable solution to extend the emission further into the near-infrared, as the electronic band structure of the Si<sub>1-x</sub>Ge<sub>x</sub> alloy depends on the Ge content  $x$  and can be adjusted in order to narrow the bandgap of the QS. Similar to Si, bandgap and light emission properties of SiGe alloys can be controlled by strain [7, 8].

Different techniques have been employed to produce SiGe QDs, such as solution-based chemical techniques like colloidal synthesis [9, 10, 11], sputtering [12, 13, 14], chemical vapour deposition (CVD), and plasma-enhanced chemical vapour deposition (PECVD) [15, 16, 17], ion implantation [18, 19, 20], and molecular beam epitaxy (MBE) [21, 22, 23]. Colloidal synthesis is widely used in the fabrication CdSe and CdS [24], with a specific focus on silicon photonics relying on the other mentioned techniques because of their compatibility with the current CMOS manufacturing process. These fabrication methods can be categorized into distinct approaches. Sputtering, CVD, and PECVD initiate with the production of a substoichiometric oxide, forming QDs from the phase separation of Si and Ge during annealing. These methods result in different final properties for the QDs due to the chemical character of CVD and PECVD compared to sputtering. Bottom-up fabrication, achieved through MBE, involves depositing QDs onto a substrate surface, subsequently capped with oxide. During the ion implantation process, a supersaturation of Si and Ge are implanted into a matrix material, and upon annealing, nucleation occurs, forming QDs. Notably, ion implantation introduces a high concentration of defects during the implantation process. Therefore high-temperature annealing steps are important to reduce defect density and achieve thermodynamically stable structures.

The goal of this research is twofold. First, we fabricated SiGe QSS using a hybrid method: PECVD for  $\text{SiO}_x$  deposition plus Ge implantation with post annealing. To the best of our knowledge, this approach has not been used yet. Second, we employed steady-state and time-resolved photoluminescence to understand how the emitted wavelength and lifetimes of the QSS behave as a function of Ge concentration. X-ray diffraction and Raman spectroscopy were employed to study the structural properties of the SiGe QSS, and RBS was used to quantify the Si/Ge ratio. By systematically incorporating these experimental methodologies, we aim to elucidate the influence of germanium on the optical properties of the SiGe quantum structures.

## 5.2 Experimental details

N-type silicon (100) substrates were initially stripped with HF acid to remove the native oxide and subsequently deposited with  $\text{SiO}_x$  layers using the PECVD system, model STS 310PC,

using silane and dinitrogen oxide as precursors at the Western Nanofabrication Facility. The chamber pressure was kept constant over the process at 800 mTorr, and the substrate temperature at 300 °C. Three different ratios of gas flows were used in order to achieve different concentrations of Si excess in the film, resulting in three different SiO<sub>x</sub> films according to Table 5.1. Table 5.1 also shows their respective deposition times. Following this deposition process,

Deposition regime	SiH <sub>4</sub> flow (sccm)	N <sub>2</sub> O flow (sccm)	Process duration (min)
Alpha	370	30	15
Beta	375	25	17
Gamma	385	15	22

Table 5.1: PECVD SiO<sub>x</sub> deposition parameters.

all samples were analyzed by RBS to quantify Si to O + N ratio and film thicknesses. These results will be discussed later. SiO<sub>x</sub>N<sub>y</sub> films of each deposition regime were submitted to Ge ion implantation at 100 keV with doses of 2.0 at.%, 4.0 at.%, or 8.0 at.%. Following Ge implantation, the implanted samples, plus samples with Si excess only, were annealed in an N<sub>2</sub> atmosphere for 1 h at 1100 °C, followed by forming gas annealing for interface passivation at 500 °C for 30 min. At the end of the fabrication process, nine different Si/Ge concentration ratios were achieved plus three samples with Si excess only. For example, samples originated from the deposition regime Alpha, were labeled Alpha\_1000C\_FG, Alpha\_2\_1000C\_FG, Alpha\_4\_1000C\_FG, and Alpha\_8\_1000C\_FG.

Rutherford backscattering spectroscopy (RBS) was applied to probe elemental composition in random geometry for selected samples. The measurements were carried out at the Western University Tandatron Accelerator Facility, using a monoenergetic beam of He<sup>+</sup> at 500 keV with a Si charged particle detector positioned at a scattering angle of 170°. An Sb-implanted Si standard ( $4.72 \times 10^{15}$  Sb atoms/cm<sup>2</sup>) was used to calibrate the solid angle of the detector and its channel-to-energy conversion coefficient. The uncertainty of ion yields obtained by RBS measurements derived from this process is close to 3.5%. RBS spectra were fitted using MEISwin software [25] to determine the implanted depth profiles.

The Rigaku SmartLab, at Surface Science Western, was employed for crystallographic structure analysis of the SiGe QDs in selected samples using grazing incidence X-ray diffraction (GIXRD) at 1°. The diffractometer has a Cu K $\alpha$  radiation source with  $\lambda = 0.15418$  nm

and is equipped with a high-precision theta-theta goniometer with a horizontal sample mount.

Raman measurements were performed at Western University using a custom-built system. An argon-ion laser with a wavelength of 514.5 nm was used as an excitation source. The Raman spectra were collected by a spectrometer with a 500 mm focal length and equipped with a liquid nitrogen-cooled CCD detector. The spectrometer was calibrated using a neon lamp and a silicon substrate. The uncertainty in Raman shift measurements is in the range of 1 to 2  $\text{cm}^{-1}$ .

Photoluminescence measurements were performed with a Horiba Fluorolog-QM spectrofluorometer equipped with a 75 W xenon arc lamp and two photo detectors: a Hamamatsu R928 photomultiplier tube for the 300 – 900 nm range and a DSS-IGA020 InGaAs solid-state detector for the NIR range (850 to 1700 nm). Samples were excited at 270 nm, and a long-pass filter ( $\lambda_c = 320 \pm 6$  nm) was employed to remove any reflected light from the excitation source. All spectra presented in this work were corrected to consider grating and detector efficiencies. Time-resolved photoluminescence decays were acquired using a pulsed LED with excitation wavelength of  $370 \pm 10$  nm and were detected with the PMT detector. Both PL and TRPL were performed with the excitation beam making an angle of  $65^\circ$  with respect to the sample normal, at room temperature.

### 5.3 Results and discussion

The fabricated samples were measured with RBS to determine their Si excess concentration in relation to a stoichiometric silicon dioxide film ( $\text{SiO}_2$ ), and film thickness. Initially, a set of samples was deposited on carbon substrates to estimate Si:(O+N) ratio more accurately. Secondly, the range of deposition conditions were selected, and films were grown on Si substrates. Table 5.2 shows MEISwin results after analyzing RBS measurements. It is important to note that RBS measurements revealed an average of 18 at.% nitrogen content in the films. For simplicity, we assumed that nitrogen replaces oxygen in the silicon dioxide matrix in the calculation of Si excess. As Ge was implanted with known dose, we can calculate the atomic content of Ge in relation to the excess of Si in the films using the chemical formula  $\text{Si}_{1-x}\text{Ge}_x$ . This approach yields Ge atomic content  $x$  ranging from 0.04 to 0.29, as stated in Table 5.2.

Sample	Si excess (at. %)	Ge dose (at. %)	$x$	Thickness (nm)
Alpha_2_1100C_FG	20	2	0.09	225
Alpha_4_1100C_FG	20	4	0.17	225
Alpha_8_1100C_FG	20	8	0.29	225
Beta_2_1100C_FG	30	2	0.06	232
Beta_4_1100C_FG	30	4	0.12	232
Beta_8_1100C_FG	30	8	0.21	232
Gamma_2_1100C_FG	55	2	0.04	250
Gamma_4_1100C_FG	55	4	0.07	250
Gamma_8_1100C_FG	55	8	0.13	250

Table 5.2: Concentration of Ge  $x$  determined from the chemical formula  $\text{Si}_{1-x}\text{Ge}_x$ .

Selected samples were subjected to GIXRD (grazing incidence X-ray diffraction) characterization. Figure 5.1 shows XRD scans taken at an incident angle of  $1^\circ$  with  $2\theta$  ranging from  $15^\circ$  to  $65^\circ$ . Indexing all peaks between  $50^\circ$  and  $60^\circ$  for all the samples resulted in finding

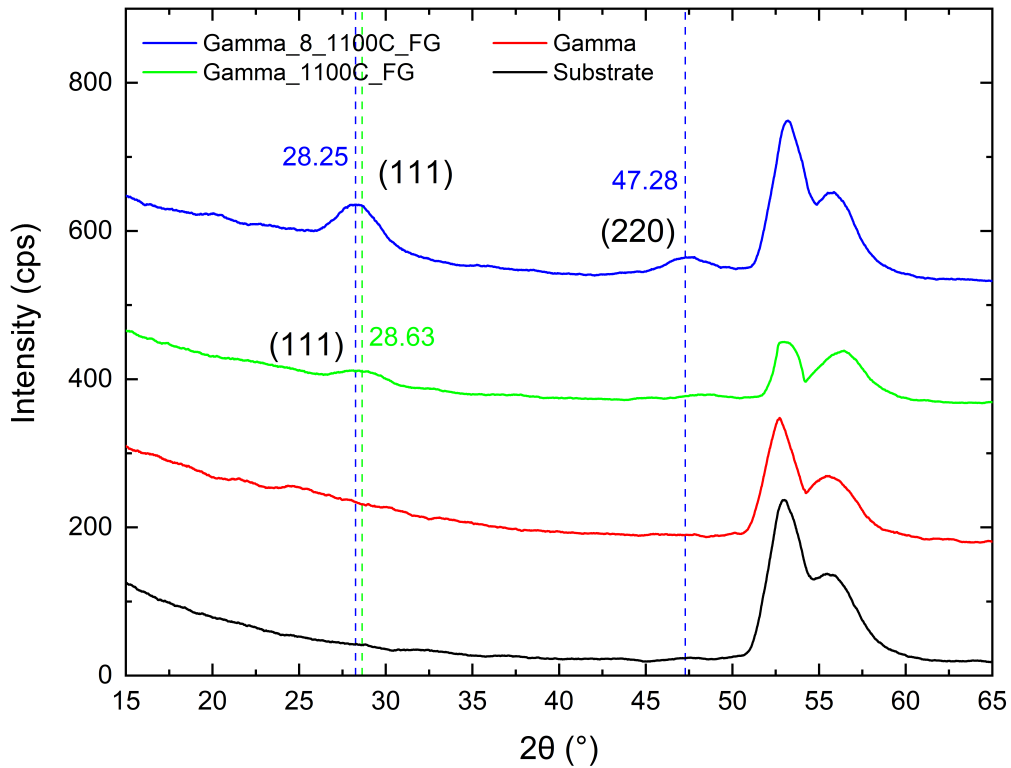


Figure 5.1: GIXRD scans of selected samples from Gamma PECVD deposition regime.

the Si (331) plane from the substrate as a major common peak for all samples [26, 27]. It can be observed that as-deposited (Gamma sample) is amorphous and, after annealing (sample Gamma\_1100C\_FG), it presents a small peak at  $28.63^\circ$  corresponding to the Si (111) plane.



The sample Gamma\_8\_1100C\_FG exhibits an additional peak at  $47.28^\circ$  associated to the plane (220) and a more pronounced diffraction at the (111) plane, indicating a higher degree of crystallization. The peak associated to the (111) plane is shifted to  $28.25^\circ$ , representing a larger lattice parameter. It has been reported that pure unstrained Si QDs were fabricated by chemical synthesis having lattice constant  $a = 5.43 \text{ \AA}$  [28]. Using Bragg's law of diffraction, we calculated the lattice parameter for samples Gamma\_1100C\_FG and Gamma\_8\_1100C\_FG being  $5.57 \text{ \AA}$  and  $5.64 \text{ \AA}$ , respectively. Small tensile strain is possible in our PECVD-grown Si QDs. The sample without Ge has a much higher lattice parameter when compared to the work of Yu et al. [28] using chemical synthesis. This fact can be explained by the nature of each preparation method. Chemical methods that result in dispersed QDs produce more pure structures, and the method used in this thesis makes QDs in a solid matrix which changes the QDs properties [6]. Our result is consistent with Vegard's law [29] when comparing the sample Gamma\_1100C\_FG to Gamma\_8\_1100C\_FG. Vegard's law relates the change in the lattice parameter as a function of each element in an alloy. For  $\text{Si}_{1-x}\text{Ge}_x$ , we have:

$$a(x)_{\text{Si}_{1-x}\text{Ge}_x} = (1 - x) a_{\text{Si}} + x a_{\text{Ge}} . \quad (5.1)$$

Therefore, it is easy to see that the alloy  $\text{Si}_{1-x}\text{Ge}_x$  has a larger lattice parameter since  $a_{\text{Ge}} > a_{\text{Si}}$ .

Raman measurements were carried out on selected samples to compare the effect of Ge implantation on vibrational properties as shown in Figure 5.2. It can be observed that, in samples with and without Ge, Raman spectra reveal three vibrational modes in common. The first mode, occurring at  $305 \text{ cm}^{-1}$ , corresponds to the longitudinal acoustic (LA) mode associated with the Si-Si bond. The longitudinal optical (LO) mode of the Si-Si bond is observed at  $434 \text{ cm}^{-1}$ , while the Si-Si transverse optical (TO) vibrational mode emerges at  $520 \text{ cm}^{-1}$ . These three vibrational modes have been reported in crystalline Si and are commonly associated with the Si substrate [30]. In addition, a careful inspection of the peak at  $520 \text{ cm}^{-1}$  in Figures 5.2(a) and 5.2(b) shows a broadening on its left side, indicating that there are also vibrations associated with phonon confinement in the QS, as reported by Shin et al. [31]. The TO peak in figures 5.2(a) and 5.2(b) does not show any shift. Thus, we do not observe strain in the Raman measurements, likely because this peak is almost entirely from the substrate. In addition to

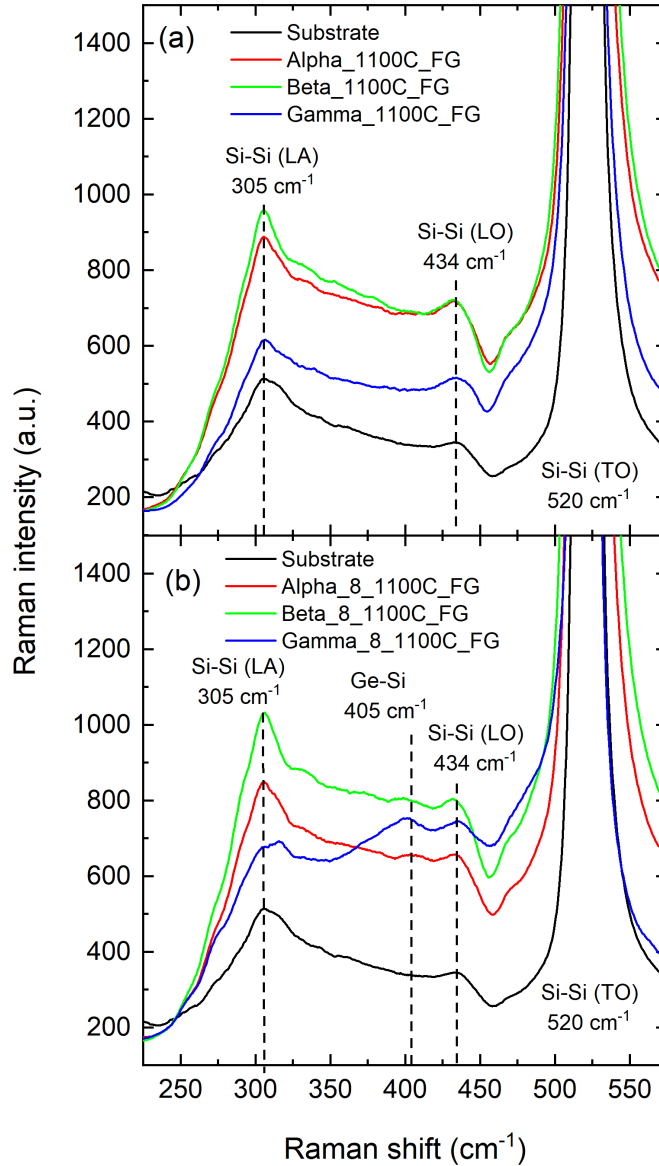


Figure 5.2: Raman spectra of samples (a) without Ge and (b) with Ge implanted at 8 at. %.

the mentioned modes, Figure 5.2(b) uniquely displays an extra peak at  $405\text{ cm}^{-1}$  in samples that went through Ge implants. This peak is associated with Si QDs containing Ge impurities, and its presence has been published theoretically [32] and experimentally [12, 20, 33]. Based on these Raman findings, we have consistent evidence of the formation of SiGe QDs after Ge implantation and annealing in all different regimes of PECVD films.

Figure 5.3 shows steady-state photoluminescence (PL) spectra obtained at room temperature in the UV-Vis and NIR. Only samples without Ge are shown to illustrate the general

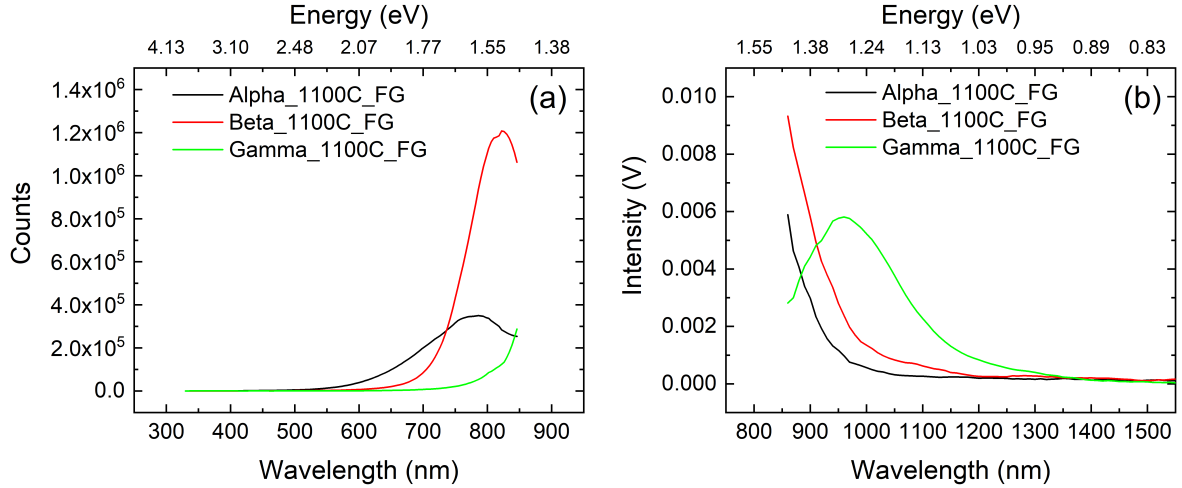


Figure 5.3: Steady-state PL on selected samples in the (a) UV-Vis and (b) NIR.

emission behaviour among the different deposition regimes. Table 5.3 shows the wavelength of maximum emission ( $\lambda_{\max}$ ) for samples without Ge, along with the calculated diameter using the approach of the effective mass approximation that provides  $E_g(D) = E_g(\infty) + A/D^2$ , where  $E_g(\infty) = 1.12$  eV and  $A = 3.57$  eV  $\cdot$  nm<sup>2</sup> [34].

Sample	$\lambda_{\max}$ (nm)	$D$ (nm)
Alpha_1100C_FG	786	2.79
Beta_1100C_FG	822	3.03
Gamma_1100C_FG	960	4.56

Table 5.3: Samples without germanium with their wavelength of maximum emission ( $\lambda_{\max}$ ) and QD diameter  $D$ .

The wavelengths of maximum emission of all samples are summarized in Figure 5.4. As we have some samples with  $\lambda_{\max}$  in the UV-Vis and others in the NIR, and our system employs different detectors for each range, we cannot make comparisons with their intensities. Some samples such as Alpha\_8.1100C\_FG, Beta\_8.1100C\_FG, and Gamma\_8.1100C\_FG did not have their  $\lambda_{\max}$  determined using the NIR solid-state detector because of their weak emission. We can observe in Figure 5.4 that samples without Ge (Alpha\_1100C\_FG, Beta\_1100C\_FG, Gamma\_1100C\_FG, black dots in Figure 5.4) present a red shift (towards higher wavelength numbers) as the concentration of Si in the deposited films increases. According to the RBS results shown in Table 5.2, these samples have 20%, 30%, and 55% Si excess in relation to stoichiometric SiO<sub>2</sub>, respectively. Therefore, the lower N<sub>2</sub>O flow rate (Table 5.1) has led to

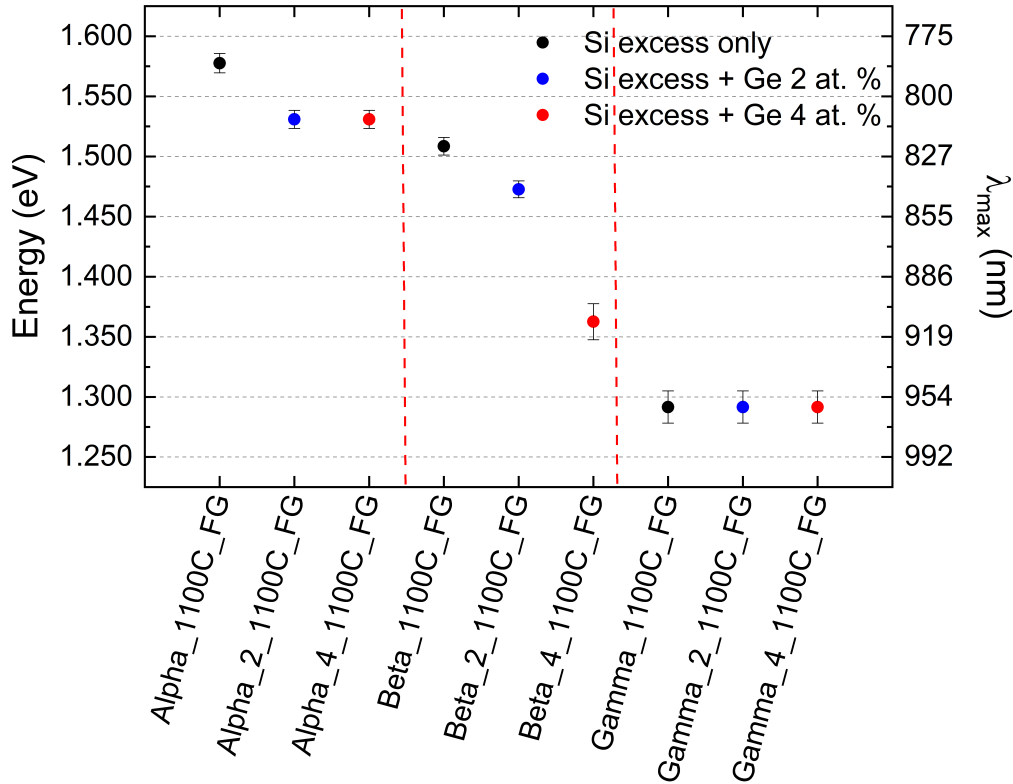


Figure 5.4: Wavelength of maximum emission,  $\lambda_{\max}$ , obtained during steady-state PL characterization. Samples Alpha, Beta, and Gamma with Ge 8 at.% did not have their  $\lambda_{\max}$  determined because of their weak emission.

a higher Si to (O+N) ratio. Consequently, higher Si concentration for Si QD nucleation in the matrix produces larger QDs.

When Ge is added to these samples, we observe a shift towards higher wavelengths (or lower energies) in the majority of samples (Figure 5.4), and this shift is due to the decrease in the bandgap for SiGe compounds with a higher Ge at.%. As a consequence, the QDs formed by this compound will have a lowered emission energy. The only samples that do not show this behaviour are those from the Gamma sample set, which has the highest concentration of Si excess.

After steady-state PL measurements, samples were subjected to TRPL characterization at room temperature. Their lifetimes were measured at 800 nm. A 1 ms pulse width and 1.7 ms observation window were kept constant during all the measurements. As a single exponential did not yield good quality fits ( $R^2 < 0.7$ ), the curves were individually normalized and fitted

with a double exponential decay curve:

$$y = y_0 + A_1 e^{-t/t_1} + A_2 e^{-t/t_2}, \quad (5.2)$$

where  $y_0$  is an offset related to the background noise, and  $A_1$  and  $A_2$  are the weights of each lifetime  $t_1$  and  $t_2$ , respectively. The parameters obtained from the fitting of all measurements are summarized in Table 5.4.

Sample	$y_0$	$A_1$	$t_1$ ( $\mu\text{s}$ )	$A_2$	$t_2$ ( $\mu\text{s}$ )	$\bar{t}_w$ ( $\mu\text{s}$ )
Alpha_1100C_FG	$0.019 \pm 0.001$	$0.78 \pm 0.01$	$31 \pm 1$	$0.22 \pm 0.01$	$211 \pm 9$	$71 \pm 5$
Alpha_2_1100C_FG	$0.024 \pm 0.001$	$0.75 \pm 0.01$	$23 \pm 1$	$0.25 \pm 0.01$	$196 \pm 9$	$65 \pm 5$
Alpha_4_1100C_FG	$0.022 \pm 0.001$	$0.83 \pm 0.01$	$30 \pm 1$	$0.17 \pm 0.01$	$246 \pm 18$	$67 \pm 7$
Alpha_8_1100C_FG	$0.012 \pm 0.001$	$0.76 \pm 0.02$	$20 \pm 1$	$0.24 \pm 0.02$	$98 \pm 5$	$38 \pm 4$
Beta_1100C_FG	$0.007 \pm 0.001$	$0.74 \pm 0.01$	$30 \pm 0$	$0.26 \pm 0.01$	$107 \pm 3$	$49 \pm 3$
Beta_2_1100C_FG	$0.009 \pm 0.001$	$0.85 \pm 0.01$	$29 \pm 1$	$0.15 \pm 0.01$	$137 \pm 8$	$45 \pm 5$
Beta_4_1100C_FG	$0.010 \pm 0.001$	$0.86 \pm 0.01$	$28 \pm 1$	$0.14 \pm 0.01$	$141 \pm 8$	$43 \pm 4$
Beta_8_1100C_FG	$0.017 \pm 0.001$	$0.59 \pm 0.02$	$14 \pm 1$	$0.41 \pm 0.03$	$64 \pm 3$	$34 \pm 4$
Gamma_1100C_FG	$0.009 \pm 0.001$	$0.72 \pm 0.02$	$28 \pm 1$	$0.28 \pm 0.03$	$129 \pm 8$	$57 \pm 7$
Gamma_2_1100C_FG	$0.017 \pm 0.001$	$0.69 \pm 0.03$	$24 \pm 2$	$0.31 \pm 0.03$	$113 \pm 8$	$52 \pm 7$
Gamma_4_1100C_FG	$0.024 \pm 0.001$	$0.70 \pm 0.05$	$24 \pm 2$	$0.30 \pm 0.05$	$103 \pm 12$	$48 \pm 10$
Gamma_8_1100C_FG	$0.026 \pm 0.001$	$0.41 \pm 0.05$	$7 \pm 2$	$0.59 \pm 0.05$	$53 \pm 4$	$34 \pm 10$

Table 5.4: Parameters obtained from double exponential fit ( $y = y_0 + A_1 e^{-t/t_1} + A_2 e^{-t/t_2}$ ) of time-resolved photoluminescence decays along with the average-weighted lifetime.

Table 5.4 also shows the average-weighted lifetime  $\bar{t}_w = (A_1 t_1 + A_2 t_2)/(A_1 + A_2)$ , calculated for each sample, and it is plotted in Figure 5.5. When we analyze the deposition regimes separately, it is noted that the  $\bar{t}_w$  becomes shorter with increasing Ge concentration. There are two possible explanations for this phenomenon. In the first one, germanium atoms break the symmetry of the system and increase the oscillator strength of the excitons, which shortens the lifetime, according to Delerue et al.[35]. Another possibility is the shortening of lifetime caused by a higher number of defects introduced during the implantation process. The last possibility is the most likely, since defects are non-radiative recombination centers in this kind

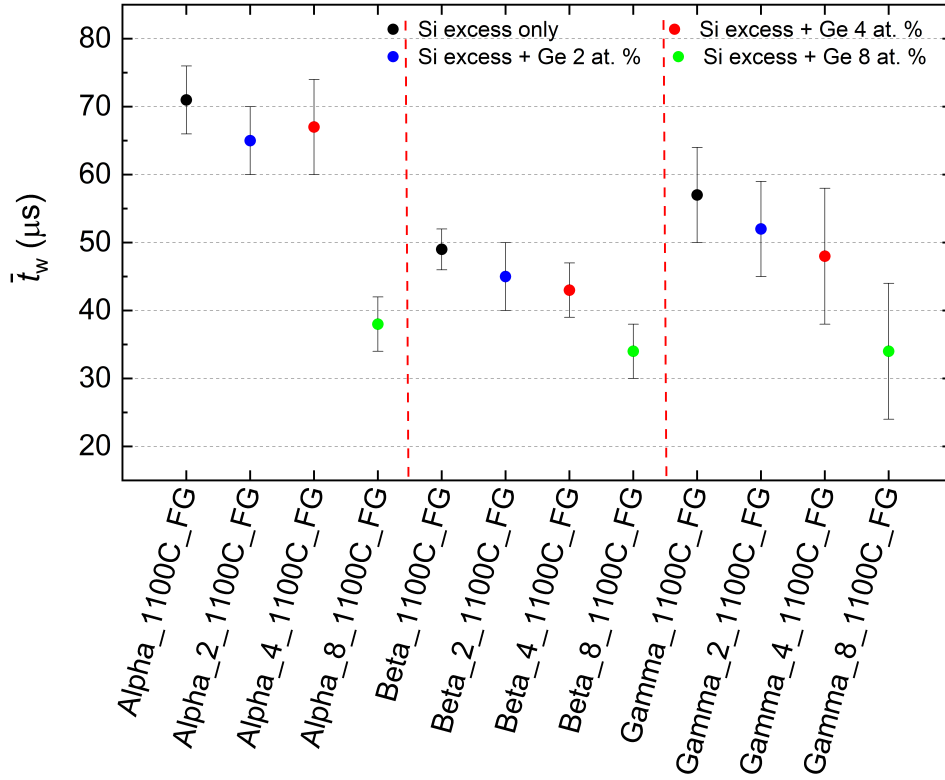


Figure 5.5: Average-weighted lifetime  $\bar{t}_w = (A_1 t_1 + A_2 t_2)/(A_1 + A_2)$  for each sample.

of system [34], and it was also observed that the PL intensity decreased as Ge dose increased.

It is important to note that samples originating from deposition regime Gamma had their emission decay measured at 800 nm, which is not their  $\lambda_{\text{max}}$ . The data and analysis of these samples were plotted just for the record, and their TRPL results cannot be compared to those of the other samples.

When comparing the samples of the deposition regime Alpha to Beta, we must recall that the QD diameters also play an important role in the lifetime of QSS. We estimated the QD sizes of Alpha\_1100C\_FG to 2.79 nm, and Beta\_1100C\_FG to 3.03 nm. According to the literature, the lifetime shortens as the QD diameter increases [35, 36]. Based on that, we would expect the longest lifetime for sample Beta\_1100C\_FG, although the longest one belongs to sample Alpha\_1100C\_FG. This contradictory behaviour can also be explained by the defect concentration that may be higher in sample Beta\_1100C\_FG since it showed PL intensity 10 orders of magnitude lower than Alpha\_1100C\_FG.

At this point, it is interesting to compare the photoluminescence properties of the two dis-

tinct fabrication methods that were used to make SiGe QDs in this thesis. All the samples described in Chapter 4 were made with Si peak excess of 17.5 at. %, very close to some of the samples in this chapter (Alpha set), which has Si excess of 20 at. %. Furthermore, samples produced by the hybrid method (PECVD plus Ge implant) were annealed only after Ge implants, therefore we choose to compare with the sample set “AA”, that underwent annealing only after Si and Ge implants, as described in Chapter 4. Figure 5.6 combines steady-state PL spectra from samples described in chapters 4 and 5, in panels (a) and (b), respectively.

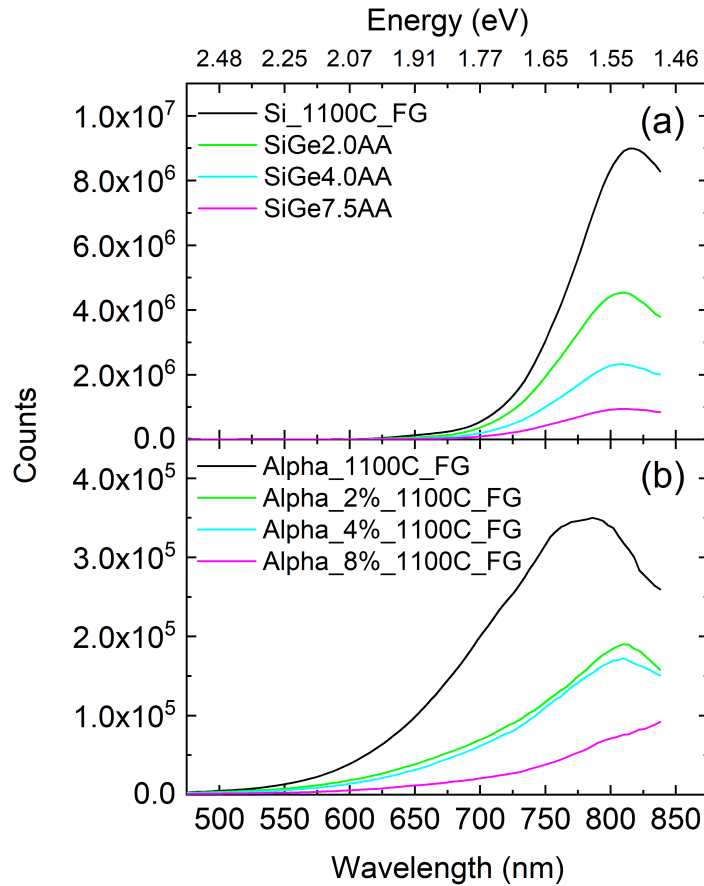


Figure 5.6: Steady-state PL comparison between (a) SiGeXAA and (b) Alpha\_X% sample sets. Samples in (a) were fabricated by co-implant of Si and Ge while samples in (b) were fabricated by a combination of PECVD plus Ge implant.

We observe that samples produced by co-implantation exhibit higher ( $\times 30$ ) photoluminescence emission, and samples produced by both methods lose intensity as the Ge concentration increases. Quantum dots formed by PECVD have more Si-O-N-related defects known for quenching PL yield [6]. Moreover, literature suggests that Si quantum dots in a PECVD SiO<sub>2</sub>

matrix can be either amorphous [37] or crystalline [38]. On the other hand, it is well-established that Si QDs produced by ion implantation are crystalline [39, 40, 41]. As examined in section 5.3, my Alpha-set samples produced by PECVD are likely to be amorphous. Thus, another factor that may explain the lower PL intensity in PECVD samples is the larger disorder at the amorphous QD/matrix interface, leading to the decrease of PL intensity. Comparing samples without Ge, it can be observed in Figure 5.6 that PECVD sample Alpha\_1100C\_FG is shifted to lower wavelengths and has a broad peak compared to the sample Si\_1100C\_FG. Besides effects that are associated with N and F contamination in the film [42], the PL shift and PL peak broadening can be connected to a different average QD size and QDs size distribution between two different fabrication methods, as well as a difference in the strength of the QC, or matrix effects ( $\text{SiO}_2$  versus  $\text{SiO}_x\text{N}_y$ ). This can be investigated further, as will be discussed in the next chapter. Previously, our group demonstrated that N-rich films showed a reduction in PL intensity at high annealing temperatures of PECVD prepared samples [43]. According to Cadogan et al. [43], if Si-QDs in an  $\text{Si}_3\text{N}_x$  matrix are to be integrated in optoelectronic devices, a hydrogenated matrix is needed to achieve a high light output.

## 5.4 Conclusions

In this study, SiGe quantum structures (QSS) were successfully fabricated using a hybrid method involving PECVD deposition of Si-rich  $\text{SiO}_2$  and Ge implantation followed by post-annealing. The investigation focused on understanding the behaviour of the emitted light wavelength and lifetimes of the QSS in relation to the Ge concentration. The structural properties of the samples were analyzed using GIXRD and Raman spectroscopy, while RBS was employed to quantify the Si/Ge ratio. RBS results revealed Si excess ranging from 4 to 29% in relation to stoichiometric silicon dioxide.

The XRD analysis indicated that the as-deposited films were amorphous, but after annealing, it exhibited crystallization, with the degree of crystallization being higher with the addition of Ge. Raman spectra revealed three common vibrational modes in samples with and without Ge, with an additional peak at  $405\text{ cm}^{-1}$  in the samples implanted with Ge, confirming the formation of SiGe QDs after Ge implantation and annealing.



Steady-state photoluminescence measurements at room temperature showed a red shift in samples without Ge as the concentration of Si increased, indicating larger QDs. The mean QD diameters calculated from PL measurements ranged from 2.79 nm to 4.56 nm. Additionally, when Ge was introduced, PL emission exhibited a shift towards higher wavelengths in most samples, which was due to the smaller bandgap of the silicon-germanium compound. Time-resolved photoluminescence measurements indicated average-weighted lifetimes between 34  $\mu$ s and 71  $\mu$ s, with a decrease in lifetime observed as the concentration of Ge increased.

In conclusion, the hybrid fabrication method successfully produced SiGe QDs, and the analysis using various techniques provided valuable insights into their structural and optical properties. Further comparison between the two methods of SiGe QD fabrication (ion co-implantation and PECVD + implantation) will be given briefly in the next chapter. The study highlights the tunability of SiGe QDs through control of Si and Ge concentrations, offering potential applications in optoelectronic devices.

# References

- [1] L. T. Canham, *Applied Physics Letters* 57, 1046 (1990).
- [2] U. Woggon, *Optical Properties of Semiconductor Quantum Dots*, Springer, Berlin, 1997.
- [3] B. Kramer (Editor), *Advances in Solid State Physics*, Springer, Berlin, 2000.
- [4] L. Pavesi, D. J. Lockwood, (Editors), *Silicon Photonics*, Springer, 2004.
- [5] G. T. Reed (Editor), *Silicon Photonics: the state of the art*, Wiley, 2008.
- [6] E. G. Barbagiovanni, D. J. Lockwood, P. J. Simpson, and L. V. Goncharova, *Appl. Phys. Rev.* 1, 011302 (2014).
- [7] J.-M. Baribeau, X. Wu, N. L. Rowell, and D. J. Lockwood, *J. Phys.: Condens. Matter* 18, R139 (2006).
- [8] N. L. Rowell and D. J. Lockwood, *ECS Trans.* 97, 3 (2020).
- [9] F. Erogbogbo, T. Liu, N. Ramadurai, P. Tuccarione, L. Lai, M. T. Swihart, and P. N. Prasad, *ACS Nano* 5, 7950 (2011).
- [10] C. Mehringer, C. Klöner, B. Butz, B. Winter, E. Spiecker, and W. Peukert, *Nanoscale* 7, 5186 (2015).
- [11] S. J. Lee, T. W. Kim, J. H. Song, and M. E. Lee, *Bulletin Korean Chem Soc* 36, 2829 (2015).
- [12] S. Takeoka, K. Toshikiyo, M. Fujii, S. Hayashi, and K. Yamamoto, *Phys. Rev. B* 61, 15988 (2000).
- [13] M. Fujii, D. Kovalev, J. Diener, F. Koch, S. Takeoka, and S. Hayashi, *Journal of Applied Physics* 88, 5772 (2000).

- [14] K. U. Joshi, D. Kabiraj, A. M. Narsale, D. K. Avasthi, T. N. Warang, and D. C. Kothari, *Surface and Coatings Technology* 203, 2482 (2009).
- [15] J. Hanna, T. Ohuchi, and M. Yamamoto, *Journal of Non-Crystalline Solids* 198–200, 879 (1996).
- [16] A. Rodríguez, M. I. Ortiz, J. Sangrador, T. Rodríguez, M. Avella, A. C. Prieto, J. Jiménez, A. Kling, and C. Ballesteros, *Physica Status Solidi (a)* 204, 1639 (2007).
- [17] C.-H. Lee, C.-Y. Yu, C. M. Lin, C. W. Liu, H. Lin, and W.-H. Chang, *Applied Surface Science* 254, 6257 (2008).
- [18] J. G. Zhu, C. W. White, J. D. Budai, S. P. Withrow, and Y. Chen, *Journal of Applied Physics* 78, 4386 (1995).
- [19] W. Xu, H. Tu, D. Liu, R. Teng, Q. Xiao, and Q. Chang, *J Nanopart Res* 13, 7095 (2011).
- [20] K. Zhong, M. Lai, Y. Chen, and B. Gu, *Physica B: Condensed Matter* 407, 3660 (2012).
- [21] Z. Yang, Y. Shi, J. Liu, B. Yan, R. Zhang, Y. Zheng, and K. Wang, *Materials Letters* 58, 3765 (2004).
- [22] E.-K. Lee, D. J. Lockwood, J.-M. Baribeau, A. M. Bratkovsky, T. I. Kamins, and L. Tsybeskov, *Phys. Rev. B* 79, (2009).
- [23] S. A. Mala, L. Tsybeskov, D. J. Lockwood, X. Wu, and J.-M. Baribeau, *Applied Physics Letters* 103, (2013).
- [24] K. Agarwal, H. Rai, and S. Mondal, *Mater. Res. Express* 10, 062001 (2023).
- [25] T. Nishimura, *Nuclear Instruments and Methods B* 371 (2016).
- [26] C. Weiss, M. Rumpel, M. Schnabel, P. Löper, and S. Janz, *28th European Photovoltaic Solar Energy Conference and Exhibition*; 387-391 (2013).
- [27] Y. Tang, B. Wang, R. Xue, and H. Yan, *Powder Diffr.* 35, 178 (2020).
- [28] Y. Yu, G. Fan, A. Fermi, R. Mazzaro, V. Morandi, P. Ceroni, D.-M. Smilgies, and B. A. Korgel, *J. Phys. Chem. C* 121, 23240 (2017).
- [29] M. Willander, O. Nur, and S. C. Jain, *Silicon Germanium Strained Layers and Heterostructures*, *Phys. Scr. T114*, 22 (2004).

- [30] P. H. Tan, K. Brunner, D. Bougeard, and G. Abstreiter, *Phys. Rev. B* 68 (12), (2003).
- [31] H. K. Shin, D. J. Lockwood, and J.-M. Baribeau, *Solid State Communications* 114, 505 (2000).
- [32] A.S. Vasin, O.V. Vikhrova, and M.I. Vasilevskiy, *J. Appl. Phys.* 115 (14), 143505 (2014)
- [33] N. A. P. Mogaddam, A. S. Alagoz, S. Yerci, R. Turan, S. Foss, and T. G. Finstad, *J. Appl. Phys.* 104, 124309 (2008).
- [34] E. G. Barbagiovanni, D. J. Lockwood, P. J. Simpson, and L. V. Goncharova, *J. Appl. Phys.* 111, 034307 (2012).
- [35] C. Delerue, G. Allan, and M. Lannoo, *J. Lumin.* 80, 65 (1999).
- [36] C. Garcia, B. Garrido, P. Pellegrino, R. Ferre, J. A. Moreno, J. R. Morante, L. Pavesi, and M. Cazzanelli, *Appl. Phys. Lett.* 82, 1595 (2003).
- [37] L. A. Nesbit, *Applied Physics Letters* 46, 38 (1985).
- [38] T. Inokuma, Y. Wakayama, T. Muramoto, R. Aoki, Y. Kurata, and S. Hasegawa, *Journal of Applied Physics* 83, 2228 (1998).
- [39] H. Z. Song and X. M. Bao, *Phys. Rev. B* 55, 6988 (1997).
- [40] C. Bonafos, B. Colombeau, A. Altibelli, M. Carrada, G. Ben Assayag, B. Garrido, M. Lopez, A. Perez-Rodriguez, J. R. Morante, and A. Claverie, *Nuclear Instruments and Methods in Physics Research Section B: Beam Interactions with Materials and Atoms* 178, 17 (2001).
- [41] B. Garrido Fernandez, M. Lopez, C. Garcia, A. Perez-Rodriguez, J. R. Morante, C. Bonafos, M. Carrada, and A. Claverie, *Journal of Applied Physics* 91, 798 (2002).
- [42] S. Mirabella, R. Agosta, G. Franzò, I. Crupi, M. Miritello, R. Lo Savio, M. A. Di Stefano, S. Di Marco, F. Simone, and A. Terrasi, *Journal of Applied Physics* 106, (2009).
- [43] C. C. Cadogan, L. V. Goncharova, P. J. Simpson, P. H. Nguyen, Z. Q. Wang, and T.-K. Sham, *Journal of Vacuum Science & Technology B* 34, 61202 (2016).

# Chapter 6

## Conclusions and future work

### 6.1 Conclusions

Silicon has been the dominant semiconductor in the electronic industry due to its interface with silicon oxide that has a low concentration of defects, and its versatility achieved through various dopants and doping levels. Despite poor light emission due to indirect bandgap of bulk Si, silicon quantum structures (Qs) such as Si quantum dots (QDs) show great potential to improve Si light emission. The electrical and optical properties of these quantum structures are intrinsically connected to the collective lattice vibrations (phonons), and are influenced by defects. Consequently, a critical aspect in the advancement and refinement of semiconductor devices involves characterizing and quantifying such defects. In Chapter 3 of this thesis, I described a method to correlate the surface and near-surface concentration of defects to the Debye temperature measured by LEED. In Chapters 4 and 5, I investigated the optical (luminescence and time-resolved PL) and structural characteristics of SiGe quantum structures (Qs) formed either by Si and Ge sequential implantation, or by Ge implantation into an insulating matrix of Si-rich silicon oxide deposited by PECVD.

In Chapter 3, I obtained surface Debye temperatures by LEED pattern intensity analysis as a function of temperature for Si (001) and for two Si epitaxial films of 1.0  $\mu\text{m}$  and 0.6  $\mu\text{m}$ , with uncertainty close to 4%. The value of  $\theta_D$  averaged over the three energies at which LEED patterns were measured at spot (0 1) is equal to  $333 \pm 13$  K for the reference sample Si (001),  $299 \pm 12$  K for SoS 1.0  $\mu\text{m}$ , and  $260 \pm 10$  K for SoS 0.6  $\mu\text{m}$ . Other techniques such as RBS

and PAS were used in order to correlate the surface Debye temperature to the surface and near-surface concentration of defects. RBS and PAS analyses revealed that the concentration of defects was highest in proximity to the film/substrate interface, likely due to the lattice mismatch, and decreased toward the surface. The near-surface concentration of defects calculated from RBS was  $4.62 \times 10^{13} \text{ cm}^{-2}$  for Si (001),  $7.28 \times 10^{13} \text{ cm}^{-2}$  for SoS  $1.0 \mu\text{m}$  and  $1.33 \times 10^{14} \text{ cm}^{-2}$  for SoS  $0.6 \mu\text{m}$ . PAS results also showed that the thinner epitaxial layer has more defects in the near-surface layer compared to the thicker film:  $1.32 \times 10^{12} \text{ cm}^{-2}$  for SoS  $1.0 \mu\text{m}$  and  $2.25 \times 10^{12} \text{ cm}^{-2}$  for SoS  $0.6 \mu\text{m}$ . Therefore, I showed that a larger concentration of defects  $N_d$  in Si epitaxial films correlates with a lower surface Debye temperature following the empirical relation  $\theta_D = (365 \pm 14) - (8.1 \pm 1.5) \times 10^{-13} N_d$  for our set of samples. Overall, LEED measurements of the surface Debye temperature exhibited good sensitivity to near-surface defect concentrations, and may have potential as a quantitative tool for defect characterization and quantification.

In Chapter 4, I used Si and Ge ion co-implantation to produce SiGe quantum structures (Qs) in a silicon dioxide matrix, focusing on the effect of annealing step sequence on the formation and luminescence properties of these Qs. I investigated two sample sets of SiGe Qs fabricated by Si implantation at the same dose, with varying Ge doses ranging from 0.5 at.% to 7.5 at.%. The first set underwent annealing between the Si and Ge implants, while the second set was annealed after both implantations. Photoluminescence measurements showed the presence of both visible and near-infrared bands for the Qs, suggesting a broad range of particle sizes. The sample set without intermediate annealing presented a consistent shift towards higher wavelengths as the concentration of Ge increased, demonstrating that the QD bandgap was reduced. Raman spectroscopy evidenced SiGe crystal formation for high Ge concentrations in samples annealed after both implants. Time-resolved photoluminescence (TRPL) measurements demonstrated two decay components, with shorter lifetimes associated with higher Ge content in both sets of samples. For pure Si QDs, TRPL results showed two distinct time constants of  $70 \pm 1 \mu\text{s}$  and  $220 \pm 2 \mu\text{s}$ , similar to results for similar systems reported in the literature. Thus, I found that the effective formation of SiGe quantum dots required a sequential implantation process of Si and Ge, followed by thermal annealing. Opting for an alternative annealing sequence, involving intermediate anneal between Si and Ge implants,

primarily resulted in the formation of pure Si quantum dots. The Ge implantation plus the final annealing increased the defect concentration, leading to a decrease in photoluminescence intensity since the final annealing step failed to incorporate Ge atoms into the Si QDs lattice.

In Chapter 5, I fabricated SiGe quantum structures (Qs) using a hybrid method involving PECVD deposition of Si-rich  $\text{SiO}_x$  followed by Ge implantation and then post-annealing. Three different Si-rich  $\text{SiO}_x$  regimes were deposited by PECVD, with Si excess concentrations of 20, 30, and 55 at.% as measured by RBS. Germanium implantation doses were 2, 4, and 8 at.%. After the Ge implants, samples underwent thermal annealing for Qs formation. GIXRD and Raman were employed to study the structural properties of the produced samples. The structural analyses were correlated to the steady-state and time-resolved photoluminescence spectra in order to understand the behaviour of the optical emission properties of the Qs in relation to the Ge concentration. After annealing, the as-deposited films underwent crystallization, as evidenced by XRD analysis, with a higher degree of crystallization observed in samples with Ge. Raman spectra confirmed the formation of SiGe quantum dots (QDs) subsequent to Ge implantation and annealing. A red shift in samples without Ge was measured by PL as the concentration of Si increased, indicating larger QDs. The QD diameters calculated from PL measurements ranged from 2.79 nm to 4.56 nm. Additionally, when Ge was introduced, PL exhibited a shift towards higher wavelengths in most of the samples. TRPL measurements indicated average-weighted lifetimes between  $34 \pm 10 \mu\text{s}$  and  $71 \pm 5 \mu\text{s}$ , with a decrease in lifetime observed as the concentration of Ge increased. Overall, the hybrid fabrication method effectively generated SiGe quantum structures (Qs) emitting in the NIR, but with decreasing intensity for Ge concentrations higher than 8 at.%.

In conclusion, this thesis made significant contributions to the field of surface science and silicon photonics. I introduced a novel method for characterizing surface and near-surface defects in crystalline materials, establishing a correlation between defect concentrations and surface Debye temperatures measured via LEED. Additionally, the investigation into the luminescence properties of SiGe quantum structures fabricated through ion co-implantation highlighted the importance of annealing sequences to the optical characteristics of these materials. Furthermore, the study of a hybrid fabrication method involving PECVD and Ge implantation offers an alternative for efficiently producing SiGe quantum structures with tailored properties.

Overall, these contributions advance our understanding of defect characterization techniques and provide valuable insights into optimizing the fabrication processes of semiconductor quantum structures for various applications in photonics and electronics.

## 6.2 Future work

The research conducted in this thesis establishes a foundation for extending the methodology of LEED to quantify surface and near-surface defects in various samples, such as Ge crystals, and especially in compound semiconductors like GaAs, SiC, SiGe, etc. This expansion holds significance for two reasons. First, it will enhance the robustness of the method by enriching its database. Second, the current formulation of the Debye-Waller factor, expressed in Equation 3.3, exclusively accommodates single-atom materials. Consequently, there exists an avenue for theoretical advancements in calculating the Debye temperature through the application of LEED to diatomic materials.

I see the future of the research on SiGe quantum structures by expanding the optical characterization to low-temperature photoluminescence. At lower temperatures, non-radiative processes are minimized, preserving radiative recombination processes and providing a clearer signal of the transitions involved in the luminescence process. Additionally, low-temperature measurements can lead to sharper and better-resolved spectral features. This enhanced resolution can offer more detailed information about the optical properties of the QDs. Transmission electron microscopy should be used in this work in order to measure size distributions and structural parameters of the quantum dots. Moreover, XPS should be employed for its ability to detect chemical states associated with Si-Ge bonds, thereby contributing to a better understanding of the impact of Ge concentration on the properties of the QDs.



# Appendix A

## Copyrights



This is a License Agreement between Matheus Coelho Adam ("User") and Copyright Clearance Center, Inc. ("CCC") on behalf of the Rightsholder identified in the order details below. The license consists of the order details, the Marketplace Permissions General Terms and Conditions below, and any Rightsholder Terms and Conditions which are included below.

All payments must be made in full to CCC in accordance with the Marketplace Permissions General Terms and Conditions below.

<b>Order Date</b>	04-Mar-2024	<b>Type of Use</b>	Republish in a thesis/dissertation
<b>Order License ID</b>	1457289-1	<b>Publisher</b>	ELSEVIER BV
<b>ISSN</b>	0039-6028	<b>Portion</b>	Chapter/article

### LICENSED CONTENT

---

<b>Publication Title</b>	Surface science	<b>Rightsholder</b>	Elsevier Science & Technology Journals
<b>Article Title</b>	Surface Debye temperature determination from LEED: correlation to defects in epitaxial films	<b>Publication Type</b>	Journal
<b>Date</b>	01/01/1964	<b>Start Page</b>	122104
<b>Language</b>	English, French, German	<b>Volume</b>	723
<b>Country</b>	Netherlands		

# Curriculum Vitae: Matheus Coelho Adam

## EDUCATION

**Ph.D. Physics** 2019 - present

The University of Western Ontario, London, ON, Canada

Thesis: Luminescence and Structural Properties of Silicon-Germanium Quantum Structures Fabricated by Ion Implantation

**M.Sc. Physics** 2010 – 2013

Federal University of Rio Grande do Sul, Porto Alegre RS, Brazil

Thesis: Silicon Nitride Deposited by Reactive Sputtering for Non-Volatile Memory Applications

**B.Sc. Physics** 2006 – 2010

Federal University of Rio Grande do Sul, Porto Alegre RS, Brazil

Thesis: Characterization of Deep Levels Close to the Valence Band in Proton Implanted GaAs

## PUBLICATIONS

1. F. L. Buguis, N. S. Y. Hsu, S. A. Sirohey, **M. C. Adam**, L. V. Goncharova, and J. B. Gilroy, Dyads and Triads of Boron Difluoride Formazanate and Boron Difluoride Dipyrromethene Dyes, *Chemistry A* (2023).
2. Y. Liu, L.-Y. Chang, L.-C. Hsu, **M. C. Adam**, Y. Jiang, L. V. Goncharova, and L. Liu, The Role of Li<sup>+</sup> and Yb<sup>3+</sup> in Modulating the Electronic Structure and Luminescence of MgGeO<sub>3</sub>:Mn<sup>2+</sup> Nanoparticles, *Journal of Alloys and Compounds* 957, 170422 (2023).
3. **M. C. Adam**, N. Darukhanawalla, J. M. Gaudet, G. O'Hara, P. Harford, G. Hall, J. Ociepa, M. H. Weber, P. J. Simpson, and L. V. Goncharova, Surface Debye Temperature Determination from LEED: Correlation to Defects in Epitaxial Films, *Surface Science* 723, 122104 (2022).
4. Matheus Adam, Artur Vicente P. Coelho, Marcelo B. Pereira, and Henri I. Boudinov. Sputtered Silicon Nitride Thin Films for Non-Volatile Memory Applications. *ECS Transactions* 39, 371 (2011).

5. Coelho, A V P; **Adam, M C**; Boudinov, H. Distinguishing bulk traps and interface states in deep-level transient spectroscopy. *Journal of Physics D*, 44, 305303 (2011).
6. Coelho, A V P; **Adam, M C**; Boudinov, H. Deep levels fine structure in proton implanted p-type GaAs. *Journal of Physics D*, 43, 205104 (2010).
7. Dalponte, M; **Adam, M C**; Boudinov, H I; Goncharova, L V; Feng, T; Garfunkel, E; Gustafsson, T. Effect of excess vacancy concentration on As and Sb doping in Si. *Journal of Physics D*, 42, 165106 (2009).

## AWARDS

The Lillian Margaret & Walter David Jackson Scholarship in Physics. Academic Year 2022-2023. Western University. London, ON, Canada.

Winner of Student Poster Session. 26th International Conference on the Application of Accelerators in Research & Industry. Denton, TX, USA. November 2022.

UFRGS Young Investigator Award at XX Salão de Iniciação Científica (2008), Federal University of Rio Grande do Sul, RS, Brazil.

National Council for Scientific and Technological Development (CNPq) Fellowship for Undergrad Research. 2006 to 2010.

Coordination of Superior Level Staff Improvement (CAPES) Master's Degree Fellowship. 2010 to 2012.

## PROFESSIONAL EXPERIENCE

### **Xanadu Quantum Technologies Inc., Toronto, ON, Canada**

*Photonics Engineer (current)*

- Test of integrated photonic solutions.
- High volume testing of photonics devices.
- Wafer level equipment and optical tester integration.
- Statistical data analysis, process control for test, process characterization, and yield analysis.

### **OCI Vacuum Microengineering Inc., London, ON, Canada**

*Research Assistant for Application and Development (December 2022 – March 2024)*

- Plan and execute experiments using the MBE system to investigate Li-ion battery electrodes using AES and LEED.
- Study Li diffusion in various materials that have the potential as electrodes in the next generation of Li-ion batteries.
- Development a quality control tool for Li-based battery manufacturing.
- Assist in writing research proposals and grant applications.
- Train co-op Students by providing guidance in laboratory techniques, experiments, and research methodologies.

**CEITEC S.A., Porto Alegre, Brazil**

*Process Engineer – Probe Area (July 2013 – April 2019)*

- PCM tests employing Keithley S530 Parametric Tester.
- Functional tests employing National Instruments PXI and LabView suite software.
- Use of JMP software for data analysis.
- Tester and prober integration.
- Work with Keithley and Keysight (Agilent) general equipment (like oscilloscopes, SMUs and DMMs) for non-automated electrical characterization.
- Development of prober recipes for engineering and production tests.
- Responsible for managing the calibration schedule of equipment.
- Write procedures and work instructions for operational and engineering levels.
- Train operators and technicians.
- Work with ISO 9001 Quality Management System.

**CEITEC S.A., Porto Alegre, Brazil**

*Process Engineer – Lithography Area (April 2012 – June 2013)*

- Work with all manufacturing and metrology equipment of the lithography area, including: tracks, steppers, interferometry for resist thickness measurements, CD-SEM, overlay measurement equipment and wafer particle counter.
- Perform level 1 maintenance tasks and equipment qualification for production.
- Development of engineering and production recipes for Nikon i12 steppers and SVG Tracks.
- Active participation on manufacturing process transference, adjusting and optimizing the lithography processes.
- Process control of coating and exposure process by control charts and FMEA.